Linear and Nonlinear Elastic Wave Propagation in a Fluid-Filled Borehole

by

Sergio Kostek

M.S., Massachusetts Institute of Technology (1991)
B.S., University of São Paulo (1980)

Submitted to the Department of Earth, Atmospheric, and Planetary Sciences
in partial fulfillment of the requirements for the degree of
Doctor of Philosophy
at the
MASSACHUSETTS INSTITUTE OF TECHNOLOGY
April 1993

Signature of the Author ....
Department of Earth, Atmospheric and Planetary Sciences
April 27, 1993

Certified by . ...
M. Nafi Toksöz
Professor of Geophysics
Thesis Advisor

Certified by . ...
R. Burridge
Scientific Advisor
Thesis Co-Advisor

Accepted by ....
Thomas H. Jordan
Chairman
Department of Earth, Atmospheric, and Planetary Sciences

Linear and Nonlinear Elastic Wave Propagation in a Fluid-Filled Borehole

by

Sergio Kostek

Submitted to the Department of Earth, Atmospheric, and Planetary Sciences
on April 27, 1993, in partial fulfillment of the
requirements for the degree of
Doctor of Philosophy

Abstract

This thesis is concerned with the propagation of waves in a fluid-filled borehole and their interactions with a surrounding elastic formation. In particular, we focus on the lowest order borehole mode, the Stoneley wave. The three problems of interest here are: radiation from the borehole into an anisotropic formation; the interaction of Stoneley waves with fluid-filled fractures; and the effects of formation nonlinearities on the propagation of Stoneley waves.

In the first part of the thesis we develop a formalism which represents the borehole in terms of effective sources for low-frequency radiation into an anisotropic, slowly varying medium. The method consists of introducing the ratio of borehole radius to wavelength ϵ as a small parameter and then obtaining an asymptotic solution in ascending powers of ϵ. In this way we obtain a sequence of problems which are solvable in a closed form. The first problem is a two-dimensional static elastic problem for the inflation of a borehole in an arbitrary anisotropic solid. The next problem involves a one-dimensional hyperbolic system of equations for pressure and longitudinal particle velocity in the fluid. The coefficients in this system involve the solution to the first problem. The final step is to find a source of seismic waves in the solid, which is equivalent to the traveling tube wave (low-frequency limit of the Stoneley wave). That is, we replace the solid and borehole by an intact solid and construct a moving system of body-force dipoles concentrated along the location of the centerline of the borehole, which generates the same seismic radiation as the propagating tube wave in the actual borehole. By combining the body force distribution with appropriate Green's functions we obtain the far-field radiation pattern from a source in a borehole. Results are obtained for situations where the tube wave is either faster or slower than the quasi-shear waves in the solid. In the former case we identify the existence of (possibly two) Mach waves and provide explicit solutions for the far-field radiation. The cross-well geometry, where a source is placed in one borehole and receivers in another, is also analysed and a solution is obtained in a form which clearly exhibits reciprocity.

In the second part we develop analytical and finite-difference models for studying wave propagation in boreholes surrounded by inhomogeneous elastic media. The presence of a fluid-filled fracture intersecting the borehole is modelled explicitly and its effects on Stoneley waves are studied. For instance, we find that elasticity of the formation tends to increase the reflection coefficient of Stoneley waves. On the other hand, multiple fractures lead to an interference phenomenon which results in a decrease of the reflection coefficient when compared to a single fracture with the same total aperture. The effects of a washout in the presence of a fracture are shown to be negligible at low frequencies but it strongly dominates the reflectivity at higher frequencies. The analytical models we have developed can be used to interpret Stoneley wave reflection data, where the effective fracture aperture can be quantified. The first model considers the effects of borehole enlargements (*e.g.,* washouts) on the reflection coefficient of Stoneley waves. By using low-frequency arguments we obtain an expression which involves the washout volume, which can be obtained from a caliper log. Comparisons of this model and the finite-difference solutions previously obtained are in good agreement. Next we develop an elastic model which generalizes the rigid formation model and correctly predicts the effective fracture aperture. We also establish the equivalence between multiple fractures and a permeable medium.

In the third part we study the effects of formation nonlinearities on the propagation of Stoneley waves. We motivate the study by recognizing that rocks are much more nonlinear than homogeneous materials. We then introduce a formalism for studying small amplitude wave propagation in prestressed media, and develop a perturbation model that allows the computation of changes in Stoneley wave phase velocity as a function of borehole pressure. The results obtained indicate that the effects are measurable and that pressurizing the borehole is an effective method of measuring the in-situ nonlinear properties of rocks.

Thesis Advisor: M. Nafi Toksöz
Title: Professor of Geophysics

Thesis Co-Advisor: R. Burridge
Title: Scientific Advisor

Acknowledgements

It has been almost six years now since I first contacted my advisor Nafi Toksöz about the possibilities of coming to M.I.T. to pursue a Ph.D. I had been working in the oil related industry for almost eight years then, and it was not easy to make the decision to come back to academic life. Nafi, however, played a major role in getting me back to graduate school, and I will always be grateful to him for that. He has guided me since the beginning, when I finally decided to take some time off from work and engage in serious studies. He has provided guidance and constructive criticism throughout my thesis work, giving me enough freedom to pursue the problems that I thought were of scientific interest. He has also been a good friend and I have enjoyed discussing politics, economics, and other matters with him.

I would also like to thank my co-advisor and friend, Bob Burridge. Since I was transferred to Schlumberger-Doll Research (SDR) I had always wanted to work with Bob. It gave me great joy when he accepted to be my co-advisor. Since then, we have worked on many exciting problems. Anyone familiar with his work will recognize his influence on this thesis.

I thank the management of Schlumberger for letting me take a one-year leave and for providing all the financial support for this to be possible. I would like to be more specific and thank Tom Tombrello from Caltech, who at the time was the director of research at SDR, and who is also responsible for my transfer to Ridgefield. He and Phil Christie were the people at Schlumberger first involved in getting me back to school. The support of Mike Ekstrom, Bill Preeg, and Steve Chang are also acknowledged. They have provided the fertile atmosphere at work, such that I could sail through my reseach without interruptions. I owe a lot to them.

My education at M.I.T. was a very pleasing experience. I thank Tom Jordan, Ted Madden, and Dan Rothman for the excellent courses they taught and for influencing my scientific views. At ERL I have interacted with many people, but I would like to single out Arthur Cheng and thank him for the many stimulating discussions we have had on borehole acoustics. Interactions with Roger Turpening, Batakrishna Mandal, Arcangelo Sena, Rick Gibson, Xiao-ming Tang were very stimulating and enriched my geophysical knowledge. I should also thank my Brazilian friends at M.I.T., Fernando Frimm, Hermano Igo Krebs, and Paul Milewski, for their tremendous support on all aspects of my student life. Their friendship is very dear to me.

At Schlumberger, I have had the fortune to collaborate and learn much of what I know about wave propagation and rock physics from David Linton Johnson, Curt Randall, Bikash Sinha, Tom Plona, Larry Schwartz, Tarek Habashy, Jian Hsu, and Ken Winkler. David has been a great mentor throughout my work and I am very grateful for that. Bikash and Curt have been a great source of help in some of the topics of this thesis.

My collaboration with Ari Ben-Menahem was very rewarding and actually planted the seed for some of the work that I subsequently pursued. Another person that I have collaborated extensively and that I would like to thank is Andy Norris. I have learned a great deal from him. I enjoy very much his friendship and enthusiasm for science.

My deepest gratitudes go to my wife, Eliane, and children, Natasha and Vladimir, for their love and support during this busy time of our lives. I could not have done this work without Eliane's constant encouragement and unselfish love.

Dedicated to my parents, Anna and Michajlo,
my lovely wife, Eliane, and my children, Natasha and Vladimir,
for their sacrifice, love, and support.

Contents

Chapter 1

Introduction

1.1 Background

In the last 10-15 years the acoustic properties of a fluid-filled cylindrical cavity in an elastic solid have received a great deal of attention, not least because of its technical importance in the search for oil reserves. The classic papers by Tsang and Rader (1979), Cheng and Toksöz (1981), and Kurkjian and Chang (1986) have established that, depending on the spatial dependence of the sourcing transducer, the acoustic signal is composed of many different components. Some of these are normal modes of the system, corresponding to poles in the appropriate Green's function, and others, "head waves", corresponding to branch points. If the source has an axially symmetric component, it is known that at low frequencies the dominant contribution to the acoustic signal is due to the lowest order mode in the problem, the "tube wave". It consists primarily of a longitudinal vibration of the fluid, and it propagates with a speed depending upon the properties of the fluid and, because of some compliance of the borehole wall, the geometry of the borehole and the properties of the solid. If the solid were perfectly rigid, the tube wave speed would be the characteristic acoustic speed in the fluid.

Because of the compliance of the borehole wall, a tube wave may act as a source of seismic waves in the surrounding solid. In a fast formation, where the tube wave is slower than the shear wave in the solid, a steadily moving tube wave produces a disturbance which is confined to the neighborhood of the borehole, but seismic waves are excited where the tube wave behaves discontinuously, such as near the source and as the wave passes through significant interfaces. In a slow formation, where the tube wave is faster than the shear wave in the solid, in addition, a propagating tube wave will continuously shed a conical shear wave as it travels.

White and Sengbush (1963) computed the low-frequency far-field radiation from a point source in a fluid-filled borehole by integrating the contribution from the pressure wave propagating along the borehole at the tube wave speed. In doing so they used a result obtained by Heelan (1953) who computed the far-field low-frequency displacements due to a transient pressure applied to a short length of an empty cylindrical borehole. The far-field low-frequency displacements thus obtained are a generalization of the results obtained by Lee and Balch (1982) who derived these displacements by a stationary phase approximation to the exact solution of a point source in a fluid-filled borehole. White and Sengbush (1963) addressed the cases of both fast and slow formations.

Based on the results of Lee and Balch (1982), Ben-Menahem and Kostek (1991) recognized that, under certain circumstances, the far-field low-frequency radiation from a point source in a fluid-filled borehole was equivalent to that generated by a suitable combination of a monopole source and a vertical dipole source localized in the formation in the absence of the borehole. Kurkjian *et al.* (1992) showed that the exact radiation pattern was obtained if the mechanism above was allowed to move up and down the borehole at the tube wave speed.

Recently there has been much interest in cross-well tomography in which sources are placed in one borehole and receivers in another. The radiation related to the source well has also been studied by de Bruin and Huizer (1989), Albright and Johnson (1990), and Meredith (1991), whereas coupling of formation body waves into tube waves was first treated by White (1953), and later analyzed by Schoenberg (1986). Complicated couplings from tube waves into channel waves in the source well, and from channel waves into tube waves at the receiver well has been described by Lines *et al.* (1992), Albright and Johnson (1990), and Krohn (1990). Further complications arise if the formation is anisotropic. Thus, it becomes important to develop a general method for obtaining equivalent sources in these circumstances.

Tube waves are also important in fracture detection. Reflected tube waves (low-frequency Stoneley waves) have been used by Hornby *et al.* (1989) to locate fractures and estimate their effective aperture by using a simple analytical model. The approach considers both horizontal as well as inclined parallel-plate models of fractures. Comparisons with laboratory data show that the simple analytical model tends to underestimate the reflection coefficient of Stoneley waves. To account for the effects of the wall elasticity, Tang (1990) used a modal solution valid at low frequencies to derive expressions for the reflection and transmission coefficients of Stoneley waves from a horizontal parallel-plate model of a fluid-filled fracture. The reflection coefficients resulting from this model are higher in amplitude than the ones predicted with the rigid formation assumption. Multiple fractures and borehole environmental conditions also affect tube waves in various ways (Kostek and Randall, 1991). Further modeling is required in order to extract quantitative information from reflection data.

Finally, nonlinear effects in rocks such as manifested in their pressure dependence of wave speeds, have been recognized in the past (King, 1966; Toksöz *et al.*, 1976) but have gained interest only recently (Johnson *et al.*, 1987; Johnson and Shankland, 1989; Johnson *et al.*, 1991; Meegan *et al.*, 1992; Johnson *et al.*, 1992). The microstructure of the rocks (microcracks, grain-to-grain contacts, etc.) clearly give rise to this highly nonlinear behaviour. These structural inhomogeneities act as nucleation sites for failure, whose initial stages are accompanied by the movement of dislocations, the development of a system of microcracks, the opening of microcracks and pores, the formation of macrocracks, and finally, failure. Laboratory studies (Shkolnik *et al.*, 1990) showed that higher-order elastic constants are much more sensitive than the linear constants to detect such inhomogeneities. In-situ formation nonlinearities have never been measured before with wave propagation techniques. It becomes of interest to understand the nonlinear effects on tube waves, since they are potentially related to rock strength.

1.2 Outline

This thesis is concerned with the propagation of waves in a fluid-filled borehole and their interactions with a surrounding elastic medium. We develop a formalism which represents the borehole in terms of effective sources for low-frequency radiation into an anisotropic, slowly varying medium. The fundamental borehole mode which gives rise to this radiation is the tube wave (low-frequency Stoneley wave). Its interaction with fluid-filled fractures intersecting the borehole are studied through numerical and analytical models. The effects of formation nonlinearity on this borehole mode are also studied.

In Chapter 2 we present the low-frequency asymptotic theory for representing sources in a fluid-filled borehole. The method consists of introducing the ratio of borehole radius to wavelength ϵ as a small parameter and then obtaining an asymptotic solution in ascending powers of ϵ. In this way we obtain a sequence of problems which are solvable. The first problem is a two-dimensional static elastic problem for the inflation of a borehole in an arbitrary anisotropic solid. The next problem arising in the asymptotic approach involves a one-dimensional hyperbolic system of equations for pressure and longitudinal particle velocity in the fluid. The coefficients in this system involve the solution to the static elastic problem just mentioned. The next and final step is to find a source of seismic waves in the solid, which is equivalent to the traveling tube wave. That is, we replace the solid and borehole by an intact solid and construct a moving system of body-force dipoles concentrated along the location of the centerline of the borehole, which generates the same seismic radiation as the propagating tube wave in the actual borehole. Explicit results are obtained for a medium with orthorhombic symmetry.

In Chapter 3 we quote a form for the far-field Green's function in an anisotropic medium and then combine it with the body force distribution to calculate the far field. Results are obtained for situations where the tube wave is either faster or slower than the quasi-shear waves. In the former case we identify the existence of (possibly two) Mach waves and provide explicit results for the far-field radiation. The important cross-well geometry, where a source is placed in one borehole and receivers in another, is analysed. The solution is obtained in a form which clearly exhibits reciprocity. The far field is first specialized to a circular borehole in an isotropic medium, and shown to be identical to those of Lee and Balch (1982) and Ben-Menahem and Kostek (1991). Then, the nontrivial case of a borehole in a transversely isotropic medium is considered, where we show the radiation patterns and wavefront surfaces for various situations involving media with symmetry axis parallel or perpendicular to the borehole axis, and also with triplication of the quasi-shear wavefront.

Chapter 4 presents a mathematical model and its numerical implementation, for studying wave propagation in boreholes surrounded by inhomogeneous elastic media. The presence of a fluid-filled fracture intersecting the borehole is modelled explicitly and its effects on Stoneley waves are studied. Various situations involving rigid/elastic formations, single/multiple fractures, and borehole washouts are studied and their effects on the reflectivity of Stoneley waves are discussed. For instance, we find that elasticity of the formation tends to increase the reflection coefficient of Stoneley waves. On the other hand, multiple fractures lead to an interference phenomena which results in a decrease of the reflection coefficient when compared to a single fracture with the same total aperture. The effects of a washout in the presence of a fracture are shown to be negligible at low frequencies but strongly dominates the reflectivity at higher frequencies. These examples illustrate that better models are needed in order to obtain quantitative information from reflected Stoneley waves.

In Chapter 5 we develop a series of simple analytical models which can be used to interpret Stoneley wave reflection data. For instance, the effective fracture aperture can be quantified. The first model considers the effects of borehole enlargements (*e.g.*, washouts) on the reflection coefficient of Stoneley waves. By using low-frequency arguments we obtain an expression which involves the washout volume, which can be obtained from a caliper log. Comparisons of this model and the finite-difference solutions previously obtained are in good agreement. Next we develop an elastic model which generalizes the rigid formation model of Hornby *et al.* (1989). It also agrees with the finite-difference calculations obtained in the previous chapter. We finally establish the equivalence between multiple fractures and a permeable medium.

In Chapter 6 we study the effects of formation nonlinearities on the propagation of Stoneley waves. We motivate the study by recognizing that rocks are much more nonlinear than homogeneous materials. We then develop the formalism for studying small amplitude wave propagation in prestressed media, and a perturbation model that allows the computation of changes in Stoneley wave phase velocity as a function of borehole pressure. The results obtained indicate that the effects are measurable and that pressurizing the borehole is an effective method of measuring the in-situ nonlinear properties of rocks.

Chapter 2

Tube Waves and Effective Sources

2.1 Introduction

An important wave mode which propagates along a fluid-filled borehole is the Stoneley wave. At low frequencies this mode is usually called a “tube wave”, which is primarily a longitudinal vibration of the fluid. It propagates with a speed depending upon the properties of the fluid and, because of some compliance of the borehole wall, the geometry of the hole and the properties of the solid. If the solid were perfectly rigid, the tube wave speed would be the characteristic acoustic speed in the fluid.

Because of the compliance of the borehole wall, a tube wave may act as a source of seismic waves in the surrounding solid. In a fast formation, where the tube wave is slower than the shear wave (S-wave) in the solid, a steadily moving tube wave produces a disturbance which is confined to the neighborhood of the hole, but seismic waves are excited where the tube wave behaves discontinuously, such as near the source and as the wave passes through significant interfaces. In a slow formation, where the tube wave is faster than the S-wave in the solid, in addition, a propagating tube wave will continuously shed a conical shear wave as it travels.

Most previous related work has been confined to circular holes in isotropic solids because wave problems in such a structure can be solved exactly in terms (of infinite sums and integrals) of Bessel functions and exponentials. See, for instance, Lee and Balch (1982), where the authors obtain an exact solution and then consider the low-frequency régime, where the borehole radius is much less than a wavelength.

In view of the difficulty (perhaps impossibility) of solving analytically any but the most symmetrical dynamical problems, and the difficulty at this time of obtaining three-dimensional numerical solutions, we have developed a method of obtaining the low-frequency (or narrow-borehole) approximation directly without first obtaining an exact solution. The method consists of introducing the ratio of borehole radius to wavelength ϵ as a small parameter and then obtaining an asymptotic solution in ascending powers of ϵ. In this way we obtain a sequence of problems which are solvable.

The first problem is a two-dimensional static elastic problem for the inflation of a hole in an arbitrary anisotropic solid. The relevant theory was developed to study stress concentrations around holes in plates under tension. See Lekhnitskii (1963) and Savin (1961). In those works the solution is obtained in terms of stress functions. For variety, in this thesis, we present the theory in terms of displacement, since this relates more closely to the physics under consideration. The next problem arising in the asymptotic approach involves a one-dimensional hyperbolic system of equations for pressure and longitudinal particle velocity in the fluid. The coefficients in this system involve the solution to the static elastic problem just mentioned.

The next and final step is to find a source of seismic waves in the solid, which is equivalent to the traveling tube wave. That is, we replace the solid with a hole by an intact solid and construct a moving system of body-force dipoles concentrated along the location of the centerline of the hole, which generates the same seismic radiation as the propagating tube wave in the actual hole. As final generalizations we allow the cross-section of the borehole to be elliptical and allow the borehole centerline to be curved, provided that the radius of curvature is long compared with a wavelength. We assume the ratio is $O(1/\epsilon)$.

2.2 Equations of Motion in Borehole-Centered Coordinates

In this section we define borehole-centered coordinates, which are a curvilinear orthogonal system in which one coordinate is arc-length s along the centerline of the hole and the other two are cartesian coordinates in the plane perpendicular to the borehole at the point specified by s. As s varies this system does not rotate around the centerline. The system is singular at the center of curvature of the centerline. The acoustic equations in the fluid, the elastodynamic equations in the solid, the appropriate interface conditions on the surface of the borehole, and the conditions at infinity are stated first in cartesian coordinates and then in the borehole centered coordinates.

2.2.1 Borehole-Centered Coordinates

Let $\mathbf{x} = (x_1, x_2, x_3)$ be cartesian coordinates and let

$$\mathbf{x} = \mathbf{X}(s) \tag{2.1}$$

be the equation of the borehole axis parametrized by arclength s. Then

$$\mathbf{e}_3(s) = \mathbf{X}'(s) \tag{2.2}$$

is a unit tangent vector to this curve. We complete $\mathbf{e}_3$ into an orthonormal triple $\{\mathbf{e}_1, \mathbf{e}_2, \mathbf{e}_3\}$ by requiring that as s varies, this frame does not rotate about $\mathbf{e}_3(s)$; that is, the component of its angular velocity about $\mathbf{e}_3(s)$ is zero. To do this we regard $\mathbf{e}_3(s)$ and $\mathbf{e}_3'(s)$ as given and choose $\mathbf{e}_1(s)$, $\mathbf{e}_2(s)$ so that

$$\begin{aligned} \mathbf{e}_1'(s) &= -[\mathbf{e}_3'(s)\cdot\mathbf{e}_1(s)]\mathbf{e}_3(s), \\ \mathbf{e}_2'(s) &= -[\mathbf{e}_3'(s)\cdot\mathbf{e}_2(s)]\mathbf{e}_3(s). \end{aligned} \tag{2.3}$$

Then

$$\begin{aligned} \mathbf{e}_1'(s) &= -\alpha_1\mathbf{e}_3(s), \\ \mathbf{e}_2'(s) &= -\alpha_2\mathbf{e}_3(s), \\ \mathbf{e}_3'(s) &= \alpha_1\mathbf{e}_1(s) + \alpha_2\mathbf{e}_2(s), \end{aligned} \tag{2.4}$$

where

$$\alpha_1 = \mathbf{e}_3'(s)\cdot\mathbf{e}_1(s), \quad \alpha_2 = \mathbf{e}_3'(s)\cdot\mathbf{e}_2(s). \tag{2.5}$$

We set

$$\mathbf{x} = \mathbf{X}(s) + q_1\mathbf{e}_1(s) + q_2\mathbf{e}_2(s). \tag{2.6}$$

Then q_1, q_2, $s = q_3$ are borehole-centered coordinates.

$$\begin{aligned} \mathrm{d}\mathbf{x} &= [\mathbf{X}'(s) + q_1\mathbf{e}_1'(s) + q_2\mathbf{e}_2'(s)]\,\mathrm{d}s + \mathrm{d}q_1\mathbf{e}_1(s) + \mathrm{d}q_2\mathbf{e}_2(s) \\ &= \mathrm{d}q_1\mathbf{e}_1 + \mathrm{d}q_2\mathbf{e}_2 + (1 - \alpha_1 q_1 - \alpha_2 q_2)\,\mathrm{d}q_3\mathbf{e}_3, \end{aligned} \tag{2.7}$$

and so

$$|\,\mathrm{d}\mathbf{x}|^2 = \mathrm{d}q_1^2 + \mathrm{d}q_2^2 + h^2\,\mathrm{d}q_3^2, \tag{2.8}$$

where

$$h(q_1, q_2, q_3) = 1 - \alpha_1(q_3)q_1 - \alpha_2(q_3)q_2. \tag{2.9}$$

Thus (q_1, q_2, q_3) form an orthogonal curvilinear coordinate system. We shall next state the equations of motion in cartesian coordinates and then rewrite them in borehole-centered coordinates.

2.2.2 The Equations of Motion in Cartesian Coordinates

The momentum and constitutive equations in the borehole fluid are

$$\rho_f \mathbf{v}_{,t} + \nabla p = \mathbf{0}, \tag{2.10}$$

$$\sigma p_{,t} + \nabla\cdot\mathbf{v} = G_{,t}. \tag{2.11}$$

Here ρ_f and σ are the density and bulk compliance of the fluid, p and $\mathbf{v}$ are the pressure and velocity, respectively, and G is a source term representing the production of volume. Let ρ be the density, $\mathbf{u}$ the particle displacement, $\mathbf{w} = \mathbf{u}_{,t}$ the particle velocity, and $\boldsymbol{\tau}$ the stress in the solid. Then the momentum and constitutive equations in the solid are

$$\rho\mathbf{w}_{,t} - \nabla\cdot\boldsymbol{\tau} = \mathbf{0}, \tag{2.12}$$

$$\boldsymbol{\tau} = \mathbf{c} : \nabla\mathbf{u}, \tag{2.13}$$

where $\mathbf{c}$ is the fourth rank tensor of elastic constants (stiffnesses). If the medium is isotropic (2.13) specializes to

$$\boldsymbol{\tau} = \lambda(\nabla\cdot\mathbf{u})\mathbf{I} + \mu(\nabla\mathbf{u} + \mathbf{u}\nabla), \tag{2.14}$$

where λ and μ are the Lamé constants. Equations (2.13) and (2.14) may be differentiated with respect to t to obtain

$$\boldsymbol{\tau}_{,t} = \mathbf{c} : \nabla\mathbf{w}, \tag{2.15}$$

$$\boldsymbol{\tau}_{,t} = \lambda(\nabla\cdot\mathbf{w})\mathbf{I} + \mu(\nabla\mathbf{w} + \mathbf{w}\nabla). \tag{2.16}$$

Together with (2.12) they form the elastodynamic equations as a first-order hyperbolic system.

On the interface between the fluid and the solid (the borehole wall) the normal particle velocity and traction are continuous:

$$\mathbf{n}\cdot(\mathbf{w} + \mathbf{w}^I) = \mathbf{n}\cdot\mathbf{v}, \tag{2.17}$$

$$(\boldsymbol{\tau} + \boldsymbol{\tau}^I)\cdot\mathbf{n} = -p\mathbf{n}. \tag{2.18}$$

Here $\mathbf{n}$ is the unit normal to the interface pointing into the solid; $\mathbf{w}^I$ and $\boldsymbol{\tau}^I$ are the particle velocity and stress fields due to an incident wave. They satisfy the homogeneous elastodynamic equations outside the borehole and enter our equations only through the interface conditions (2.17) and (2.18). To complete the specification of the problem we require the boundary condition at infinity that $\mathbf{u}$, $\mathbf{w}$,and $\boldsymbol{\tau}$ tend to zero as the field point recedes from the borehole.

2.2.3 The Equations of Motion in Borehole Centered Coordinates

Using the formulae of Subsection 2.2.1 we rewrite the equations of motion as follows. Equation (2.10) becomes

$$\begin{aligned} \rho_f v_{1,t} + p_{,1} &= 0, \\ \rho_f v_{2,t} + p_{,2} &= 0, \\ \rho_f v_{3,t} + h^{-1} p_{,3} &= 0. \end{aligned} \tag{2.19}$$

Equation (2.11) becomes

$$\sigma p_{,t} + v_{1,1} + v_{2,2} + h^{-1}(v_{3,3} - \alpha_1 v_1 - \alpha_2 v_2) = G_{,t}. \tag{2.20}$$

The interface conditions expressed by Equations (2.17) and (2.18) become

$$n_k(w_k + w_k^I) = n_k v_k, \tag{2.21}$$

and

$$(\tau_{ij} + \tau_{ij}^I)n_j = -pn_i. \tag{2.22}$$

The boundary condition at infinity becomes

$$\mathbf{u},\ \mathbf{w},\ \boldsymbol{\tau} \to 0 \quad \text{as} \quad \sqrt{q_1^2 + q_2^2} \to \infty. \tag{2.23}$$

The momentum equation in the solid becomes

$$\begin{aligned} \rho w_{1,t} &= \tau_{11,1} + \tau_{21,2} + h^{-1}\tau_{31,3} + h^{-1}(-\alpha_1\tau_{11} - \alpha_2\tau_{21} + \alpha_1\tau_{33}), \\ \rho w_{2,t} &= \tau_{12,1} + \tau_{22,2} + h^{-1}\tau_{32,3} + h^{-1}(-\alpha_1\tau_{12} - \alpha_2\tau_{22} + \alpha_2\tau_{33}), \\ \rho w_{3,t} &= \tau_{13,1} + \tau_{23,2} + h^{-1}\tau_{33,3} + 2h^{-1}(-\alpha_1\tau_{13} - \alpha_2\tau_{23}). \end{aligned} \tag{2.24}$$

The differentiated constitutive law becomes

$$\boldsymbol{\tau}_{,t} = \mathbf{c} : \nabla\mathbf{w}, \tag{2.25}$$

where

$$\nabla\mathbf{w} = \begin{pmatrix} w_{1,1} & w_{1,2} & h^{-1}(w_{1,3} + \alpha_1 w_3) \\ w_{2,1} & w_{2,2} & h^{-1}(w_{2,3} + \alpha_2 w_3) \\ w_{3,1} & w_{3,2} & h^{-1}(w_{3,3} - \alpha_1 w_1 - \alpha_2 w_2) \end{pmatrix}. \tag{2.26}$$

Substituting (2.26) into (2.25) and writing the result in full, one obtains

$$\begin{aligned} \tau_{ij,t} &= c_{ijk\delta} w_{k,\delta} + h^{-1} c_{ij\gamma 3}(w_{\gamma,3} + \alpha_\gamma w_3) \\ &\qquad + h^{-1} c_{ij33}(w_{3,3} - \alpha_1 w_1 - \alpha_2 w_2), \end{aligned} \tag{2.27}$$

where the repeated Greek subscripts are summed over the values 1,2. When the medium is isotropic (2.27) specializes to

$$\begin{aligned} \tau_{11,t} &= (\lambda + 2\mu)w_{1,1} + \lambda w_{2,2} + h^{-1}\lambda(w_{3,3} - \alpha_1 w_1 - \alpha_2 w_2), \\ \tau_{22,t} &= \lambda w_{1,1} + (\lambda + 2\mu)w_{2,2} + h^{-1}\lambda(w_{3,3} - \alpha_1 w_1 - \alpha_2 w_2), \\ \tau_{33,t} &= \lambda w_{1,1} + \lambda w_{2,2} + h^{-1}(\lambda + 2\mu)(w_{3,3} - \alpha_1 w_1 - \alpha_2 w_2), \\ \tau_{23,t} &= \mu[w_{3,2} + h^{-1}(w_{2,3} + \alpha_2 w_3)], \\ \tau_{31,t} &= \mu[w_{3,1} + h^{-1}(w_{1,3} + \alpha_1 w_3)], \\ \tau_{12,t} &= \mu(w_{2,1} + w_{1,2}). \end{aligned} \tag{2.28}$$

2.3 Asymptotic Analysis

In this section we introduce the small parameter ϵ, assuming the radius of the hole is $O(1)$, the wavelength is $O(1/\epsilon)$, and the radius of curvature of the borehole centerline is $O(1/\epsilon^2)$. We then specify that the solution should depend on time t and s only through $T = \epsilon t$ and $S = \epsilon s$ and assume an asymptotic power series in ϵ for each dependent variable. The leading-order equations tell us that to this order the fluid motion is longitudinal (along the well) and that the displacement in the solid is related to the pressure in the fluid by a two-dimensional elastostatic problem. The equations involving terms of the next order yield the one-dimensional acoustic system for pressure and longitudinal particle velocity in the fluid, showing how the coefficients depend upon the solution of the elastostatic problem which arose at the leading order. This one-dimensional system is then solved for a volume-injection source concentrated at a point in the borehole.

2.3.1 The Small Parameter ϵ

In this section we shall make some assumptions about the relative sizes of the borehole radius, the wavelength, the radius of curvature of the centerline of the borehole, and the length scale on which the material properties vary, in terms of a small parameter ϵ. We shall assume that, in the units of the coordinates q_i, the borehole radius is $O(1)$ as $\epsilon \to 0$. We shall assume that the wavelength is $O(1/\epsilon)$. The scale on which the medium properties vary and the radius of curvature are both $O(1/\epsilon^2)$. Under these assumptions α_1 and α_2 are $O(\epsilon^2)$. So, let us write

$$\alpha_i = \epsilon^2\beta_i, \quad \beta_i = O(1), \tag{2.29}$$

and

$$h^{-1} = (1 - \epsilon^2\beta_1 q_1 - \epsilon^2\beta_2 q_2)^{-1} = 1 + O(\epsilon^2). \tag{2.30}$$

Let us introduce new "slow" variables T and S defined by

$$T = \epsilon t, \quad S = \epsilon s. \tag{2.31}$$

Then

$$\partial_t = \epsilon\partial_T, \quad \partial_s = \epsilon\partial_S. \tag{2.32}$$

We shall suppose that all quantities depend upon t and s only though T and S. Thus we may rewrite (2.19) to (2.22) as

$$\begin{array}{rcl} \epsilon\rho_f v_{1,T} + p_{,1} & = & 0, \\ \epsilon\rho_f v_{2,T} + p_{,2} & = & 0, \\ \rho_f v_{3,T} + p_{,S} & = & O(\epsilon^2). \end{array} \tag{2.33}$$

$$\epsilon\sigma p_{,T} + \epsilon v_{3,S} + v_{1,1} + v_{2,2} - \epsilon G_{,T} = O(\epsilon^2), \tag{2.34}$$

$$n_\alpha(w_\alpha + w^I_\alpha) + \epsilon m_3(w_3 + w^I_3) = n_\alpha v_\alpha + \epsilon m_3 v_3, \tag{2.35}$$

$$\begin{array}{rcl} (\tau_{\alpha\beta} + \tau^I_{\alpha\beta})n_\beta + \epsilon m_3(\tau_{\alpha3} + \tau^I_{\alpha3}) & = & -pn_\alpha, \\ (\tau_{3\beta} + \tau^I_{3\beta})n_\beta + \epsilon m_3\tau_{33} & = & -\epsilon p m_3, \end{array} \tag{2.36}$$

where the Greek subscripts range over 1,2 only. Because the equation of the borehole wall depends upon q_3 only through S, we have written

$$n_3 = \epsilon^2 m_3. \tag{2.37}$$

Next (2.24) becomes

$$\begin{array}{rcl} \epsilon\rho w_{1,T} & = & \tau_{11,1} + \tau_{21,2} + \epsilon\tau_{31,S} - \epsilon^2\beta_\alpha\tau_{\alpha1} + O(\epsilon^3), \\ \epsilon\rho w_{2,T} & = & \tau_{12,1} + \tau_{22,2} + \epsilon\tau_{32,S} - \epsilon^2\beta_\alpha\tau_{\alpha2} + O(\epsilon^3), \\ \epsilon\rho w_{3,T} & = & \tau_{13,1} + \tau_{23,2} + \epsilon\tau_{33,S} - 2\epsilon^2\beta_\alpha\tau_{\alpha3} + O(\epsilon^3), \end{array} \tag{2.38}$$

and (2.25) and (2.26) become

$$\boldsymbol{\tau}_{,t} = \mathbf{c} : \nabla\mathbf{w}, \tag{2.39}$$

and

$$\nabla\mathbf{w} = \begin{pmatrix} w_{1,1} & w_{1,2} & w_{1,S} + \epsilon^2\beta_1 w_3 \\ w_{2,1} & w_{2,2} & w_{2,S} + \epsilon^2\beta_2 w_3 \\ w_{3,1} & w_{3,2} & w_{3,S} - \epsilon^2\beta_1 w_1 - \epsilon^2\beta_2 w_2 \end{pmatrix} + O(\epsilon^3). \tag{2.40}$$

Then (2.27) yields

$$\begin{array}{rcl} \epsilon\tau_{ij,T} & = & c_{ijk\delta}w_{k,\delta} + \epsilon c_{ijk3}w_{k,S} \\ & & + \epsilon^2 c_{ij\gamma3}\beta_\gamma w_3 - \epsilon^2 c_{ij33}\beta_\alpha w_\alpha + O(\epsilon^3), \end{array} \tag{2.41}$$

which, for an isotropic material, specializes to

$$\begin{aligned}
\epsilon\tau_{11,T} &= (\lambda+2\mu)w_{1,1} + \lambda w_{2,2} + \epsilon\lambda w_{3,S} + O(\epsilon^2),\\
\epsilon\tau_{22,T} &= \lambda w_{1,1} + (\lambda+2\mu)w_{2,2} + \epsilon\lambda w_{3,S} + O(\epsilon^2),\\
\epsilon\tau_{33,T} &= \lambda w_{1,1} + \lambda w_{2,2} + \epsilon(\lambda+2\mu)w_{3,S} + O(\epsilon^2),\\
\epsilon\tau_{23,T} &= \mu(w_{3,2} + \epsilon w_{2,S}) + O(\epsilon^2),\\
\epsilon\tau_{31,T} &= \mu(w_{3,1} + \epsilon w_{1,S}) + O(\epsilon^2),\\
\epsilon\tau_{12,T} &= \mu(w_{2,1} + w_{1,2}).
\end{aligned} \tag{2.42}$$

We shall assume that the field quantities can be expanded in powers of ϵ. However, they do not all start at the same power. Thus let

$$\begin{aligned}
\mathbf{v} &= \mathbf{v}^{(0)} + \epsilon\mathbf{v}^{(1)} + O(\epsilon^2),\\
p &= p^{(0)} + \epsilon p^{(1)} + O(\epsilon^2),\\
\mathbf{u} &= \mathbf{u}^{(0)} + \epsilon\mathbf{u}^{(1)} + O(\epsilon^2),\\
\mathbf{w} &= \epsilon\mathbf{w}^{(0)} + \epsilon^2\mathbf{w}^{(1)} + O(\epsilon^3),\\
\boldsymbol{\tau} &= \boldsymbol{\tau}^{(0)} + \epsilon\boldsymbol{\tau}^{(1)} + O(\epsilon^2),\\
\mathbf{u}^I &= \mathbf{u}^{I(0)} + \epsilon\mathbf{u}^{I(1)} + O(\epsilon^2),\\
\mathbf{w}^I &= \epsilon\mathbf{w}^{I(0)} + \epsilon^2\mathbf{w}^{I(1)} + O(\epsilon^3),\\
\boldsymbol{\tau}^I &= \boldsymbol{\tau}^{I(0)} + \epsilon\boldsymbol{\tau}^{I(1)} + O(\epsilon^2).
\end{aligned} \tag{2.43}$$

Also

$$\mathbf{u}, \mathbf{w}, \boldsymbol{\tau} \to 0 \quad \text{as} \quad \sqrt{q_1^2 + q_2^2} \to \infty. \tag{2.44}$$

2.3.2 The Leading Terms in ϵ and the Elastostatic Problem

We next write (2.33) to (2.41) to leading order in ϵ, using (2.43):

$$\begin{aligned}
p^{(0)}_{,1} &= 0,\\
p^{(0)}_{,2} &= 0,\\
\rho_f v^{(0)}_{3,T} + p^{(0)}_{,S} &= 0.
\end{aligned} \tag{2.45}$$

$$v^{(0)}_{1,1} + v^{(0)}_{2,2} = 0. \tag{2.46}$$

$$0 = n_\alpha v^{(0)}_\alpha. \tag{2.47}$$

$$\begin{aligned}
(\tau^{(0)}_{\alpha\beta} + \tau^{I(0)}_{\alpha\beta})n_\beta &= -p^{(0)}n_\alpha,\\
(\tau^{(0)}_{3\beta} + \tau^{I(0)}_{3\beta})n_\beta &= 0.
\end{aligned} \tag{2.48}$$

$$\begin{aligned}
0 &= \tau^{(0)}_{11,1} + \tau^{(0)}_{21,2},\\
0 &= \tau^{(0)}_{12,1} + \tau^{(0)}_{22,2},\\
0 &= \tau^{(0)}_{13,1} + \tau^{(0)}_{23,2}.
\end{aligned} \tag{2.49}$$

$$\tau^{(0)}_{ij,T} = c_{ijk\gamma} w^{(0)}_{k,\gamma}, \tag{2.50}$$

which may be integrated in T to get

$$\tau_{ij}^{(0)} = c_{ijk\gamma} u_{k,\gamma}^{(0)}. \tag{2.51}$$

The boundary condition gives

$$\mathbf{u}^{(0)} \to \mathbf{0} \text{ as } \sqrt{q_1^2 + q_2^2} \to \infty. \tag{2.52}$$

Equation (2.45) implies that $p^{(0)}$ is independent of q_1 and q_2. Thus

$$p^{(0)} = p^{(0)}(S, T). \tag{2.53}$$

Assuming irrotational fluid motion,

$$\nabla \times \mathbf{v} = \mathbf{0}, \tag{2.54}$$

Equations (2.46) and (2.47) imply that

$$v_1^{(0)} = 0, \quad v_2^{(0)} = 0. \tag{2.55}$$

Equations (2.54) and (2.55) imply that

$$v_{3,\alpha}^{(0)} = 0, \tag{2.56}$$

so that

$$v_3^{(0)} = v_3^{(0)}(S, T). \tag{2.57}$$

Equations (2.48), (2.49), (2.51), and (2.52) form a two-dimensional elastostatic problem for $\mathbf{u}^{(0)}$ and $\boldsymbol{\tau}^{(0)}$ with forcing terms $\boldsymbol{\tau}^{I(0)}$ and $p^{(0)}$ in (2.48). Thus

$$\mathbf{u}^{(0)} \quad \text{and} \quad \mathbf{w}^{(0)} \quad \text{depend linearly upon} \quad \boldsymbol{\tau}_T^{I(0)} + p_T^{(0)}\mathbf{I}. \tag{2.58}$$

2.3.3 Terms of the Next Order in ϵ

We proceed to the next order in ϵ in (2.34) and (2.35), making use of (2.43),

$$\sigma p_{,T}^{(0)} + v_{3,S}^{(0)} + v_{1,1}^{(1)} + v_{2,2}^{(1)} - G_{,T} = 0. \tag{2.59}$$

$$n_\alpha(w_\alpha^{(0)} + w_\alpha^{I(0)}) = n_\alpha v_\alpha^{(1)}. \tag{2.60}$$

Integrating (2.59) across the borehole, and using the two-dimensional divergence theorem with (2.60), we get

$$\begin{aligned} \sigma A p^{(0)}_{,T} + A v^{(0)}_{3,S} - \int_\Sigma G_{,T}\,\mathrm{d}A &= -\int_{\partial\Sigma} n_\alpha v_\alpha^{(1)}\,\mathrm{d}s \\ &= -\int_{\partial\Sigma} n_\alpha(w_\alpha^{(0)} + w_\alpha^{I(0)})\,\mathrm{d}s. \end{aligned} \tag{2.61}$$

It follows from (2.58) that $\int_{\partial\Sigma} n_\alpha w_i^{(0)}\,\mathrm{d}s$ depends linearly upon $\boldsymbol{\tau}^{I(0)}_{,T} + p^{(0)}_{,T}\mathbf{I}$. Thus

$$\int_{\partial\Sigma} n_\alpha u_i^{(0)}\,\mathrm{d}s = AN_{i\alpha pq}(\tau^{I(0)}_{pq} + p^{(0)}\delta_{pq}), \tag{2.62}$$

say. Then

$$\int_{\partial\Sigma} n_\alpha u_\alpha^{(0)}\,\mathrm{d}s = AN(\boldsymbol{\tau}^{I(0)} + p^{(0)}\mathbf{I}), \tag{2.63}$$

where $N(\boldsymbol{\tau}) = N_{\alpha\alpha pq}\tau_{pq}$. Also differentiating (2.63) with respect to T gives

$$\int_{\partial\Sigma} n_\alpha w_\alpha^{(0)}\,\mathrm{d}s = AN(\boldsymbol{\tau}^{I(0)}_{,T} + p^{(0)}_{,T}\mathbf{I}). \tag{2.64}$$

In (2.61) to (2.64) Σ is the right cross-section of the borehole at $\mathbf{X}(S)$, A is its area, and $\partial\Sigma$ its boundary. Hence we have

$$(\sigma + N(\mathbf{I}))p^{(0)}_{,T} + v^{(0)}_{3,S} = \frac{1}{A}\int_\Sigma G_{,T}\,\mathrm{d}A - \frac{1}{A}\int_\Sigma w^{I(0)}_{\alpha,\alpha}\,\mathrm{d}A - N(\boldsymbol{\tau}^{I(0)}_{,T}). \tag{2.65}$$

Because $\tau^{I(0)}_{pq} = c_{pqij}u^{I(0)}_{i,j}$ we may write (2.65) as

$$(\sigma + N(\mathbf{I}))p^{(0)}_{,T} + v^{(0)}_{3,S} = \frac{1}{A}\int_\Sigma G_{,T}\,\mathrm{d}A - [\delta_{ij} - t_i t_j + (\delta_{mn} - t_m t_n)N_{mnpq}c_{pqij}]u^{I(0)}_{i,jT}. \tag{2.66}$$

2.3.4 The One-Dimensional Acoustic System in the Fluid

Equation (2.65) together with the third equation of (2.45):

$$\rho_f v^{(0)}_{3,T} + p^{(0)}_{,S} = 0, \tag{2.67}$$

form a one-dimensional hyperbolic system for $v_3^{(0)}$ and $p^{(0)}$. We should remember that $\mathbf{v}^{(0)}$, $p^{(0)}$, $\mathbf{w}^{(0)}$, $\boldsymbol{\tau}^{(0)}$ are related to $\mathbf{v}$, p, $\mathbf{w}$, $\boldsymbol{\tau}$ by (2.43), and that these are evaluated in the coordinates q_1, q_2, q_3, which have the same physical units as x_1, x_2, x_3. Transforming (2.65) and (2.67) back to the variables s, t using (2.31) and (2.32) we get

$$(\sigma + N(\mathbf{I}))p^{(0)}_{,t} + v^{(0)}_{3,s} = \frac{1}{A}\int_{\Sigma} G_{,t}\,\mathrm{d}A - \frac{1}{A}\int_{\Sigma} u^{I(0)}_{\alpha,\alpha t}\,\mathrm{d}A - N(\boldsymbol{\tau}^{I(0)}_{,t}), \tag{2.68}$$

$$\rho_f v^{(0)}_{3,t} + p^{(0)}_{,s} = 0. \tag{2.69}$$

2.3.5 The One-Dimensional Acoustic Solution

We restate the system (2.68), (2.69):

$$\rho_f v^{(0)}_{3,t} + p^{(0)}_{,s} = 0, \tag{2.70}$$

$$(\sigma + N(\mathbf{I}))p^{(0)}_{,t} + v^{(0)}_{3,s} = \frac{1}{A}\int G_{,t}\,\mathrm{d}A = \frac{V_0}{A} g'(t)\delta(s), \tag{2.71}$$

specializing to a source concentrated at the origin and supplying accumulated volume $V_0 g(t)$ up to time t, and assuming that there is no incident stress field: $\boldsymbol{\tau}^I(0) = \mathbf{0}$. If the coefficients vary slowly, as we assume, we may solve (2.70), (2.71) by the method of generalized progressing waves and so we assume a solution in the form

$$\begin{pmatrix} v_3^{(0)} \\ p^{(0)} \end{pmatrix} = \sum_{n=0}^{\infty} \begin{pmatrix} \bar{v}_n(s) \\ \bar{p}_n(s) \end{pmatrix} f_n(t - \tau(s)) \tag{2.72}$$

away from the source. Here each f_n is one integration step smoother than the previous one:

$$f_n = f'_{n+1}, \tag{2.73}$$

and travel time $\tau(s)$, and coefficients $\bar{v}_n$, and $\bar{p}_n$ are to be determined.

On substituting (2.72) into (2.70), (2.71), and then equating the coefficients of the successive f_n to zero, we get for $n = -1$

$$\begin{pmatrix} \rho_f & -\tau' \\ -\tau' & \sigma + N(\mathbf{I}) \end{pmatrix} \begin{pmatrix} \bar{v}_0 \\ \bar{p}_0 \end{pmatrix} = \begin{pmatrix} 0 \\ 0 \end{pmatrix}, \tag{2.74}$$

and for $n = 0$

$$\begin{pmatrix} \rho_f & -\tau' \\ -\tau' & \sigma + N(\mathbf{I}) \end{pmatrix} \begin{pmatrix} \bar{v}_1 \\ \bar{p}_1 \end{pmatrix} + \begin{pmatrix} \bar{p}'_0 \\ \bar{v}'_0 \end{pmatrix} = \begin{pmatrix} 0 \\ 0 \end{pmatrix}. \tag{2.75}$$

Equation (2.74) implies

$$\tau' = \pm\gamma_T, \tag{2.76}$$

where γ_T is the tube wave slowness given by

$$\gamma_T = \sqrt{\rho_f(\sigma + N(\mathbf{I}))}. \tag{2.77}$$

Then

$$\frac{\bar{p}_0}{\bar{v}_0} = \pm\zeta, \tag{2.78}$$

where ζ is the characteristic impedance given by

$$\zeta = \sqrt{\frac{\rho_f}{\sigma + N(\mathbf{I})}}. \tag{2.79}$$

So we may write

$$\begin{pmatrix} \bar{v}_0 \\ \\ \bar{p}_0 \end{pmatrix} = a_0(s) \begin{pmatrix} \pm\zeta^{-\frac{1}{2}} \\ \\ \zeta^{\frac{1}{2}} \end{pmatrix}, \tag{2.80}$$

where a_0 is a coefficient to be determined. Using (2.80) in (2.75) and multiplying on the left by $(\pm\zeta^{-\frac{1}{2}} \quad \zeta^{\frac{1}{2}})$ we find that

$$a_0'(s) = 0. \tag{2.81}$$

Thus, to a first approximation,

$$\begin{pmatrix} v_3^{(0)} \\ \\ p^{(0)} \end{pmatrix} = a_0^{\pm} \begin{pmatrix} \pm\zeta^{-\frac{1}{2}} \\ \\ \zeta^{\frac{1}{2}} \end{pmatrix} f_0^{\pm}[t - \tau_{\pm}(s)], \tag{2.82}$$

where $a_0^{\pm}$ are constants and

$$\tau_{\pm}' = \pm\gamma_T. \tag{2.83}$$

We may now determine $a_0^{\pm} f_0^{\pm}$ by expressing (2.70) and (2.71) near the source as jump conditions:

$$\begin{aligned} p^{(0)}(+0,t) - p^{(0)}(-0,t) &= 0, \\ v_3^{(0)}(+0,t) - v_3^{(0)}(-0,t) &= \frac{V_0}{A} g'(t). \end{aligned} \tag{2.84}$$

Since causality requires the waves to propagate away from the source, we shall assume that the + or − sign in (2.82) is the same as the sign of s. Using (2.82) in (2.84) we see that

$$\begin{aligned} a_0^+ f_0^+(t) - a_0^- f_0^-(t) &= 0, \\ a_0^+ f_0^+(t) - a_0^+ f_0^-(t) &= \frac{V_0 \zeta^{\frac{1}{2}}(0) g'(t)}{A(0)}, \end{aligned} \tag{2.85}$$

so that

$$a_0^+ f^+(t) = a_0^- f^-(t) = \frac{V_0 \zeta^{\frac{1}{2}}(0) g'(t)}{2A(0)}. \tag{2.86}$$

Finally we get

$$\begin{pmatrix} v_3^{(0)} \\ p^{(0)} \end{pmatrix} = \frac{V_0}{2A_0(0)} \begin{pmatrix} \pm\zeta^{\frac{1}{2}}(0)\zeta^{-\frac{1}{2}}(s) \\ \zeta^{\frac{1}{2}}(0)\zeta^{\frac{1}{2}}(s) \end{pmatrix} g'[t - \operatorname{sgn}(s)\int_0^s \gamma_T(s')\,\mathrm{d}s']. \tag{2.87}$$

Isolating $p^{(0)}$ we have

$$p^{(0)}(s,t) = \frac{V_0 \zeta^{\frac{1}{2}}(0)\zeta^{\frac{1}{2}}(s)}{2A(0)} g'[t - \operatorname{sgn}(s)\int_0^s \gamma_T(s')\,\mathrm{d}s']. \tag{2.88}$$

This pressure distribution, which is a generalization of a standard result (White, 1983; p. 147), radiates seismic waves into the formation and will be used later to calculate an equivalent source body-force distribution in the formation.

2.4 The Line Density of Dipoles

In this section we derive the distribution of body force which, when acting in the intact solid, would produce the same radiation as the tube wave in the borehole. This turns out to be a line distribution of dipoles, concentrated along the borehole centerline, which depends upon linear operators defined by the elastostatic problem.

Let us extend the definition of $\mathbf{u}$ and $\mathbf{w}$ to the interior of the borehole, defining them to be zero there. Consider f_i defined by

$$\rho u_{i,tt} - (c_{ijk\ell} u_{k,\ell})_{,j} = f_i. \tag{2.89}$$

Then f_i will be an effective source field. To evaluate f_i, let us introduce a vector test function ϕ_i and integrate using the distributional definition of the derivatives:

$$I = \int_{-\infty}^{+\infty} \mathrm{d}t \int_V \phi_i f_i \, \mathrm{d}\mathbf{x} \;=\; \int_{-\infty}^{+\infty} \mathrm{d}t \int_V [\rho\phi_{k,tt} - (\phi_{i,j}c_{ijk\ell})_{,\ell}] u_k \, \mathrm{d}\mathbf{x}. \qquad (2.90)$$

This is an ordinary integral since the integrand is finite everywhere. Also the integrand vanishes inside the borehole. Thus

$$I = \int_{-\infty}^{+\infty} \mathrm{d}t \int_{V_\epsilon} \phi_i f_i \, \mathrm{d}\mathbf{x} \;=\; \int_{-\infty}^{+\infty} \mathrm{d}t \int_{V_\epsilon} [\rho\phi_{k,tt} - (\phi_{i,j}c_{ijk\ell})_{,\ell}] u_k \, \mathrm{d}\mathbf{x}, \qquad (2.91)$$

where V_ϵ is the region exterior to the borehole.

Now let us use the divergence theorem in V_ϵ to get

$$\begin{aligned} I \;=\; & \int_{-\infty}^{+\infty} \mathrm{d}t \int_{V_\epsilon} [-\rho\phi_{i,t}u_{i,t} + \phi_{i,j}c_{ijk\ell}u_{k,\ell}] \, \mathrm{d}\mathbf{x} \\ & + \int_{-\infty}^{+\infty} \mathrm{d}t \int_{\partial V_\epsilon} \phi_{i,j}c_{ijk\ell}u_k n_\ell \, \mathrm{d}A, \end{aligned} \qquad (2.92)$$

where ∂V_ϵ is the boundary of V_ϵ, unit normal $\mathbf{n}$ points towards the exterior of the borehole, and $\mathrm{d}A$ indicates an element of area. Integrating once more by parts we get

$$\begin{aligned} I \;=\; & \int_{-\infty}^{+\infty} \mathrm{d}t \int_{V_\epsilon} \phi_i [\rho u_{i,tt} - (c_{ijk\ell}u_{k,\ell})_{,j}] \, \mathrm{d}\mathbf{x} \\ & + \int_{-\infty}^{+\infty} \mathrm{d}t \int_{\partial V_\epsilon} (\phi_{i,j}c_{ijk\ell}u_k n_\ell - \phi_i c_{ijk\ell}u_{k,\ell}n_j) \, \mathrm{d}A \qquad (2.93) \\ =\; & \int_{-\infty}^{+\infty} \mathrm{d}t \int_{\partial V_\epsilon} (\phi_{i,j}c_{ijk\ell}u_k n_\ell - \phi_i c_{ijk\ell}u_{k,\ell}n_j) \, \mathrm{d}A, \end{aligned}$$

because u_i satisfies the homogeneous Equation (2.89) in V_ϵ. Since the borehole is narrow

$$\mathrm{d}A = \mathrm{d}s \, \mathrm{d}s', \qquad (2.94)$$

to leading order in ϵ, where s is arclength along the borehole and s' is arclength around the circumference $\partial\Sigma_s$ of the right cross-section at s. Let us also write for $\mathbf{x}$ on the borehole wall

$$\begin{aligned} \phi_i(\mathbf{x}) &= \phi_i(\mathbf{X}(s)) + [x_m - X_m(s)]\phi_{i,m}(\mathbf{X}(s)) + O(\epsilon^2), \\ c_{ijk\ell}(\mathbf{x}) &= c_{ijk\ell}(\mathbf{X}(s)) + O(\epsilon^2), \end{aligned} \qquad (2.95)$$

where $c_{ijk\ell}(\mathbf{X}(s))$ is defined by the elastic constants of the material drilled out to form the borehole. Then to leading order

$$\begin{aligned} I &= \int_{-\infty}^{+\infty} \mathrm{d}t \int \mathrm{d}s \int_{\partial\Sigma_s} \Big\{ \phi_{i,m}(\mathbf{X}(s),t) \Big[c_{imk\ell} u_k n_\ell \\ &\qquad - c_{ijk\ell} u_{k,\ell} n_j (x_m - X_m(s)) \Big] - \phi_i(\mathbf{X}(s),t) c_{ijk\ell} u_{k,\ell} n_j \Big\} \, \mathrm{d}s'. \end{aligned} \tag{2.96}$$

But

$$c_{ijk\ell} u_{k,\ell} n_j = -p n_i, \tag{2.97}$$

where p is the pressure in the borehole fluid at $\mathbf{X}(s)$, which is independent of s', $p = p^{(0)}(s,t)$, to leading order in ϵ. Thus the last term in (2.96) vanishes and (2.96) becomes

$$I = \int_{-\infty}^{+\infty} \mathrm{d}t \int \mathrm{d}s \int_{\partial\Sigma_s} \phi_{i,m}(\mathbf{X}(s),t) [c_{imk\ell} u_k n_\ell + p^{(0)} (x_m - X_m(s)) n_i] \, \mathrm{d}s', \tag{2.98}$$

where in the integrand $c_{imk\ell}$ is taken to be $c_{imk\ell}(\mathbf{X}(s))$.

Let

$$\begin{aligned} g_{im}(s,t) &= \int_{\partial\Sigma_s} [c_{imk\ell}(\mathbf{X}(s)) u_k(\mathbf{X}(s),t) n_\ell(s,s') \\ &\quad + p^{(0)}(\mathbf{X}(s),t)(x_m - X_m(s)) n_i(s,s')] \, \mathrm{d}s'. \end{aligned} \tag{2.99}$$

We now apply Stokes's theorem to (2.99). But first we write

$$\mathbf{n} = \mathbf{t}' \times \mathbf{t}, \quad n_p = \epsilon_{pqr} t'_q t_r, \tag{2.100}$$

where $\mathbf{t} = \mathbf{e}_3$ is the unit tangent to the borehole axis, and $\mathbf{t}'$ is the unit tangent to $\partial\Sigma_s$. Then

$$\begin{aligned} p^{(0)} \int_{\partial\Sigma_s} (x_m - X_m(s)) n_i \, \mathrm{d}s' &= p^{(0)} t_r \int_{\partial\Sigma_s} (x_m - X_m(s)) \epsilon_{iqr} t'_q \, \mathrm{d}s' \\ &= p^{(0)} t_r \int_{\Sigma_s} \epsilon_{qnp} (x_m - X_m(s))_{,n} \epsilon_{ipr} t_q \, \mathrm{d}A \\ &= p^{(0)} A (\delta_{qr}\delta_{ni} - \delta_{qi}\delta_{nr}) t_r t_q \delta_{mn} \\ &= p^{(0)} A (\delta_{im} - t_i t_m). \end{aligned} \tag{2.101}$$

The other term in (2.99) must be treated separately since u_k is not continuous up to the boundary in Σ_s. Let us extend $c_{ijk\ell}$ smoothly and define the fictitious displacement field u_k^* *inside* the borehole so that

$$c_{ijk\ell}u^*_{k,\ell j} = 0 \text{ in } \Sigma_s, \quad u^*_k = u_k \text{ in } \partial\Sigma_s. \tag{2.102}$$

Thus $\mathbf{u}^*$ satisfies the elastic equilibrium equations inside the borehole and has the same displacement on the boundary as the external field. Hence using Stoke's theorem we have

$$\begin{aligned}
\int_{\partial\Sigma_s} c_{imk\ell}u_k n_\ell \,\mathrm{d}s' &= \int_{\partial\Sigma_s} c_{imk\ell}u^*_k \epsilon_{\ell qr}t'_q t_r \,\mathrm{d}s' \\
&= \int_{\Sigma_s} \epsilon_{qpn}c_{imk\ell}u^*_{k,p}\epsilon_{\ell nr}t_q t_r \,\mathrm{d}A \\
&= \int_{\Sigma_s} (\delta_{qr}\delta_{p\ell} - \delta_{q\ell}\delta_{pr})c_{imk\ell}u^*_{k,p}t_q t_r \,\mathrm{d}A \\
&= \int_{\Sigma_s} (t_r t_r c_{imk\ell}u^*_{k,\ell} - t_\ell t_p c_{imk\ell}u^*_{k,p}) \,\mathrm{d}A \\
&= \int_{\Sigma_s} c_{imk\ell}u^*_{k,p}(\delta_{\ell p} - t_\ell t_p) \,\mathrm{d}A \\
&= \int_{\Sigma_s} \tau^*_{im} \,\mathrm{d}A,
\end{aligned} \tag{2.103}$$

where $\boldsymbol{\tau}^*$ is the stress field belonging to the displacement $\mathbf{u}^*$ inside Σ_s. We have used the fact that the tangential s-derivative $t_p u^*_{k,p}$ is $O(\epsilon^2)$ at most, and so the term $t_\ell t_p c_{imk\ell}u^*_{k,p}$ does not contribute. When the borehole is elliptical in cross-section $\boldsymbol{\tau}^*$ is constant and we may write

$$\int_{\partial\Sigma_s} c_{imk\ell}u^*_k n_\ell \,\mathrm{d}s' = A\tau^*_{im}. \tag{2.104}$$

Thus, using (2.101) and (2.104) in (2.99) we obtain

$$\begin{aligned}
g_{im} &= A[\tau^*_{im} + p^{(0)}(\delta_{im} - t_i t_m)] \\
&= Ap^{(0)}[c_{impq}N_{pqrs}(\delta_{rs} - t_r t_s) + \delta_{im} - t_i t_m] \\
&= Ap^{(0)}N^*_{im},
\end{aligned} \tag{2.105}$$

say. Notice the similarities between the terms in square brackets in (2.66) and (2.105). In Appendix A it is shown that $N_{pqrs} = N_{rspq}$, and so the square bracketed expressions are indeed identical. Comparing (2.90) and (2.98) using (2.99) and (2.105) we find that

$$\begin{aligned}\int \phi_i f_i \,\mathrm{d}\mathbf{x} &= \int \phi_{i,m}(\mathbf{X}(s) g_{im} \,\mathrm{d}s \\ &= \int \mathrm{d}\mathbf{x} \int \phi_{i,m}(\mathbf{x},t)\delta(\mathbf{x}-\mathbf{X}(s)) g_{im}(s,t)\,\mathrm{d}s \\ &= \int \mathrm{d}\mathbf{x} \int -\phi_i(\mathbf{x},t)\delta_{,m}(\mathbf{x}-\mathbf{X}(s)) g_{im}(s,t)\,\mathrm{d}s, \qquad (2.106)\end{aligned}$$

and since ϕ_i is an arbitrary test function we have

$$\begin{aligned}f_i(\mathbf{x},t) &= -\int g_{im}(s,t)\delta_{,m}(\mathbf{x}-\mathbf{X}(s))\,\mathrm{d}s \\ &= -\int A(s) N^*_{im}(s) p^{(0)}(s,t)\delta_{,m}(\mathbf{x}-\mathbf{X}(s))\,\mathrm{d}s. \qquad (2.107)\end{aligned}$$

The integrand above is a superposition of nine body force dipoles of differing strengths $g_{im}(s,t)$ depending on position and time. In symmetrical configurations the off diagonal terms are zero, thus reducing the force system to three mutually orthogonal dipoles moving along the borehole (see Figure 2.1). As will be shown later, these dipoles move away from the source at the tube wave speed.

2.5 The Borehole Compliance: The Elastostatic Problem

In this section we use a complex variable technique to solve that elastostatic problem and so obtain the linear operators which occur in the expression for the body force distribution. It is interesting that the linear operator involves the product of three matrices, one depends upon the elastic constants of the solid, one on the fluid pressure and any incident stress field, and the third on the profile of the borehole cross-section. The calculations are analytical except that a sextic equation has to be solved for an eigensystem.

2.5.1 The Complex Variable Method

In this section we set up the machinery for calculating the operator N and N^*_{im} of (2.63) and (2.107). Thus we must solve the elastostatic problem (2.48), (2.49) and

(2.50), which we restate using the displacement $\mathbf{u}^{(0)}$ instead of the particle velocity $\mathbf{w}^{(0)}$. The constitutive equation is

$$\tau_{ij}^{(0)} = c_{ijk\gamma} u_{k,\gamma}^{(0)}. \tag{2.108}$$

The equilibrium equation is

$$\tau_{i\alpha,\alpha}^{(0)} = 0, \tag{2.109}$$

where to this order of approximation the solution is (locally) independent of x_3, the coordinate parallel to the borehole axis. The boundary condition on the borehole wall is

$$\tau_{i\alpha}^{(0)} n_\alpha = -(\tau_{i\alpha}^{I(0)} n_\alpha + p^{(0)} n_i), \tag{2.110}$$

where $\mathbf{n}$ is normal to the borehole wall and $n_3 = 0$. In Equations (2.108), (2.109), (2.110) Roman subscripts range over 1,2,3, whereas Greek subscripts range over 1,2 only, and the summation convention applies. In solving this system of equations we use the complex variable method of Lekhnitskii (1963), Savin (1961), and Muskhelishvili (1953). These authors set up their equations in terms of stress functions, which leads naturally to the use of elastic compliances, and this is most direct when one is concerned primarily with stress concentration. But we are concerned primarily with displacements, and in the following development we take the elastic stiffnesses and displacement components as basic. However, a form of stress function will play a minor role in imposing the boundary conditions. This complex-variable method is also known as the *Stroh formalism* and was used by Stroh (1958) and (1962). See also Ting (1990) for a modern review.

The method requires that we seek the displacement as an analytic function of the combination

$$x_1 + \eta x_2. \tag{2.111}$$

Substituting (2.108) into (2.109) we get

$$c_{i\alpha k\beta} u_{k,\alpha\beta} = 0, \tag{2.112}$$

where we have dropped the superscript ${}^{(0)}$ on $\mathbf{u}$; we shall continue to drop it on $\mathbf{u}$, $\boldsymbol{\tau}$ and p in this section. Then, setting

$$u_k = u_k(z) = u_k(x_1 + \eta x_2), \tag{2.113}$$

Equation (2.112) leads to

$$\mathbf{P}(\eta)\mathbf{u}'' = 0, \tag{2.114}$$

where

$$P_{ik}(\eta) = c_{i1k1} + (c_{i1k2} + c_{i2k1})\eta + c_{i2k2}\eta^2. \tag{2.115}$$

Thus

$$\det(\mathbf{P}(\eta)) = 0. \tag{2.116}$$

But this is a sextic in η with real coefficients. So the roots are real or occur as complex conjugate pairs. Actually it follows from energy considerations that there are no real roots. Let the six roots be

$$\eta_n, \quad \bar{\eta}_n, \quad \Im\{\eta_n\} > 0, \quad n = 1,2,3. \tag{2.117}$$

From (2.114) it follows that $\mathbf{u}''$ is a null vector of $\mathbf{P}(\eta_n)$, and therefore a multiple of a standard null vector $\mathbf{U}_n$.

$$u_k'' = A_n(z_n)U_{kn}, \tag{2.118}$$

where $\mathbf{U}_n$ is a function only of the $c_{ijk\ell}$ and not of the coordinates, and $A_n(z_n)$ is a scalar coefficient depending on x_1, x_2 through

$$z_n = x_1 + \eta_n x_2, \quad n = 1,2,3, \tag{2.119}$$

on which it depends analytically. Because u_k is real, we seek u_k as the real part of a superposition of such solutions

$$u_k = \Re\{\sum_{n=1}^{3} U_{kn}A_n(z_n)\}, \quad \mathbf{u} = \Re\{\mathbf{U}\mathbf{A}\}. \tag{2.120}$$

Here $\mathbf{A}$ is the column vector with components $A_n(z_n)$, $n = 1,2,3$ and $\mathbf{U}$ is the matrix whose columns are the null vectors $\mathbf{U}_n$, $n = 1,2,3$. $A_n(z_n)$ is an analytic function of its argument. Since η_n and $\mathbf{U}_n$ are independent of x_1 and x_2, depending only on the elastic constants $c_{i\alpha k\beta}$, (2.108) and (2.120) give

$$\tau_{ij} = \Re\{\sum_{n=1}^{3}(c_{ijk1} + c_{ijk2}\eta_n)U_{kn}A_n'(z_n)\}. \tag{2.121}$$

Before imposing the boundary conditions (2.110) we shall introduce the stress functions T_i such that

$$\tau_{i1} = -T_{i,2}, \quad \tau_{i2} = T_{i,1}, \tag{2.122}$$

which exist by virtue of (2.109). Let us now consider the x_1x_2-plane. The cylindrical borehole wall cuts this plane in a curve, which we shall call the borehole profile, with tangent $\mathbf{t}$ related to x_α and n_α by

$$x_{1,s} = t_1 = -n_2, \quad x_{2,s} = t_2 = n_1, \tag{2.123}$$

where $x_{1,s}$ and $x_{2,s}$ are the derivatives of x_1 and x_2 with respect to arclength s along the borehole profile. Then using (2.122), (2.123) in the left member of (2.110) we get

$$\tau_{i\alpha}n_\alpha = \tau_{i1}t_2 - \tau_{i2}t_1 = -T_{i,2}x_{2,s} - T_{i,1}x_{1,s} = -T_{i,s}, \tag{2.124}$$

and in the right member

$$\begin{aligned} -(\tau^I_{1\alpha}n_\alpha + pn_1) &= -\tau^I_{11}x_{2,s} + \tau^I_{12}x_{1,s} - px_{2,s}, \\ -(\tau^I_{2\alpha}n_\alpha + pn_2) &= -\tau^I_{21}x_{2,s} + \tau^I_{22}x_{1,s} + px_{1,s}, \\ -\tau^I_{3\alpha}n_\alpha &= -\tau^I_{31}x_{2,s} + \tau^I_{32}x_{1,s}. \end{aligned} \tag{2.125}$$

Using (2.124), (2.125) in (2.110), with the fact that the τ^I_{ij} are constant, we obtain

$$\begin{aligned} T_1 &= -\tau^I_{12}x_1 + (\tau^I_{11} + p)x_2, \\ T_2 &= -(\tau^I_{22} + p)x_1 + \tau^I_{21}x_2, \\ T_3 &= -\tau^I_{32}x_1 + \tau^I_{31}x_2. \end{aligned} \tag{2.126}$$

Let us summarize (2.126) as

$$T_i = (\tau^I_{ik} + p\delta_{ik})\epsilon_{k\alpha}x_\alpha, \tag{2.127}$$

where

$$\epsilon = \begin{pmatrix} 0 & 1 & 0 \\ -1 & 0 & 0 \\ 0 & 0 & 0 \end{pmatrix}. \tag{2.128}$$

From (2.121) and (2.122) we have

$$\tau_{i2} = T_{i,1} = \Re\{\sum_{n=1}^{3}(c_{i2k1} + c_{i2k2}\eta_n)U_{kn}A_n'(z_n)\}, \tag{2.129}$$

and so integrating and using (2.127) we get

$$\Re\{\sum_{n=1}^{3}(c_{i2k1} + c_{i2k2}\eta_n)U_{kn}A_n(z_n)\} = (\tau_{ik}^I + p\delta_{ik})\epsilon_{k\alpha}x_\alpha \tag{2.130}$$

on the borehole profile. Let us define the matrices $\mathbf{K}_{21}$, $\mathbf{K}_{22}$, and $\boldsymbol{\Lambda}$ as follows:

$$(\mathbf{K}_{21})_{ik} = c_{i2k1}, \quad (\mathbf{K}_{22})_{ik} = c_{i2k2}, \quad \boldsymbol{\Lambda} = \mathrm{diag}\{\eta_1, \eta_2, \eta_3\}. \tag{2.131}$$

Then (2.130) may be rewritten

$$\Re\{(\mathbf{K}_{21}\mathbf{U} + \mathbf{K}_{22}\mathbf{U}\boldsymbol{\Lambda})\mathbf{A}\} = (\boldsymbol{\tau}^I + p\mathbf{I})\boldsymbol{\epsilon}\mathbf{x} \tag{2.132}$$

on the borehole profile.

2.5.2 The Elliptical Borehole

Before proceeding further we shall specialize to a borehole having elliptical profile, with major semi-axis r_1, minor semi-axis r_2, and whose major axis makes an angle α with the 1-axis. Then the elliptical profile may be parameterized by r_1, r_2, and angle θ where

$$\begin{aligned} z = x_1 + \mathrm{i}x_2 &= \mathrm{e}^{\mathrm{i}\alpha}(r_1\cos\theta + \mathrm{i}r_2\sin\theta) \\ &= \tfrac{1}{2}\mathrm{e}^{\mathrm{i}\alpha}[(r_1+r_2)\mathrm{e}^{\mathrm{i}\theta} + (r_1-r_2)\mathrm{e}^{-\mathrm{i}\theta}]. \end{aligned} \tag{2.133}$$

Setting $\zeta = \mathrm{e}^{\mathrm{i}\theta}$, (2.133) becomes

$$z = x_1 + \mathrm{i}x_2 = \tfrac{1}{2}\mathrm{e}^{\mathrm{i}\alpha}[(r_1+r_2)\zeta + (r_1-r_2)\tfrac{1}{\zeta}] \quad \text{on} \quad |\zeta| = 1. \tag{2.134}$$

But if we allow $|\zeta| > 1$, (2.134) is a conformal mapping of the exterior of the unit circle in the ζ plane onto the exterior of the ellipse in the z plane, and, because $\Im\{\eta_n\} > 0$, the exterior of the unit circle in ζ plane is mapped onto the exteriors of ellipses in the

z_n-planes. Thus the $A_n(z_n(\zeta))$ may be regarded as functions of ζ analytic outside the unit circle, constrained by (2.130) on the unit circle. So, rewriting (2.130)

$$\Re\{\sum_{n=1}^{3}(c_{i2k1}+c_{i2k2}\eta_n)U_{kn}A_n(z_n(\zeta))\} = (\tau^I_{ik}+p\delta_{ik})\epsilon_{k1}x_1(\zeta)+(\tau^I_{ik}+p\delta_{ik})\epsilon_{k2}x_2(\zeta), \tag{2.135}$$

where from (2.133)

$$\begin{aligned} x_1(\zeta) &= \tfrac{1}{2}[(r_1\cos\alpha + \mathrm{i}r_2\sin\alpha)\zeta + (r_1\cos\alpha - \mathrm{i}r_2\sin\alpha)\tfrac{1}{\zeta}], \\ x_2(\zeta) &= \tfrac{1}{2}[(r_1\sin\alpha - \mathrm{i}r_2\cos\alpha)\zeta + (r_1\sin\alpha + \mathrm{i}r_2\cos\alpha)\tfrac{1}{\zeta}]. \end{aligned} \tag{2.136}$$

and $|\zeta| = 1$.

We may now use the Schwartz formula for a function $F(\zeta)$, analytic outside the unit circle, whose real part is given on the unit circle:

$$F(\zeta) = -\frac{1}{2\pi\mathrm{i}}\oint \Re\{F(\sigma)\}\frac{\sigma+\zeta}{\sigma-\zeta}\frac{\mathrm{d}\sigma}{\sigma}, \tag{2.137}$$

where the integral is once around the unit circle $|\sigma| = 1$, $|\zeta| > 1$, and $F(\zeta)$ is analytic in $|\zeta| > 1$. Applying this to the function in braces on the left of (2.135) we obtain

$$\begin{aligned} \sum_{n=1}^{3}(c_{i2k1} + c_{i2k2}\eta_n)U_{kn}A_n(z_n(\zeta)) &= -\frac{1}{2\pi\mathrm{i}}\oint(D_i\sigma + E_i\frac{1}{\sigma})\frac{\sigma+\zeta}{\sigma-\zeta}\frac{\mathrm{d}\sigma}{\sigma} \\ &= \frac{2E_i}{\zeta}, \end{aligned} \tag{2.138}$$

where D_i and E_i are the coefficients of ζ and $\frac{1}{\zeta}$ on the right of (2.135) after (2.136) is used for $x_1(\zeta)$ and $x_2(\zeta)$. From (2.138) we see that $A_n(z_n(\zeta))$ is proportional to $\frac{1}{\zeta}$, and referring back to (2.132), we have

$$\mathbf{A} = (\mathbf{K}_{21}\mathbf{U} + \mathbf{K}_{22}\mathbf{U}\mathit{\Lambda})^{-1}\mathbf{E}\frac{2}{\zeta}. \tag{2.139}$$

Explicitly

$$\begin{aligned} 2\mathbf{E} &= (\boldsymbol{\tau}^I + p\mathbf{I})\boldsymbol{\epsilon}\begin{pmatrix} r_1\cos\alpha - \mathrm{i}r_2\sin\alpha \\ r_1\sin\alpha + \mathrm{i}r_2\cos\alpha \\ 0 \end{pmatrix} \\ &= (\boldsymbol{\tau}^I + p\mathbf{I})\begin{pmatrix} r_1\sin\alpha + \mathrm{i}r_2\cos\alpha \\ r_1\cos\alpha - \mathrm{i}r_2\sin\alpha \\ 0 \end{pmatrix}. \end{aligned} \tag{2.140}$$

Then from (2.120)

$$\mathbf{u} = \Re\{\mathbf{UA}\} = \Re\{(\mathbf{K}_{21} + \mathbf{K}_{22}\mathbf{U}\Lambda\mathbf{U}^{-1})^{-1}\mathbf{E}\frac{2}{\zeta}\}, \tag{2.141}$$

or

$$\mathbf{u} = \Re\{2(\mathbf{K}_{21} + \mathbf{K}_{22}\mathbf{U}\Lambda\mathbf{U}^{-1})^{-1}\mathbf{E}(\cos\theta - \mathrm{i}\sin\theta)\} \tag{2.142}$$

at the point with parameter θ according to (2.133), i.e.,

$$\begin{aligned} \mathbf{u} \;=\; & \Re\Big\{2(\mathbf{K}_{21} + \mathbf{K}_{22}\mathbf{U}\Lambda\mathbf{U}^{-1})^{-1}\mathbf{E} \\ & \times\Big[x_1\Big(\frac{\cos\alpha}{r_1} + \frac{\mathrm{i}\sin\alpha}{r_2}\Big) + x_2\Big(\frac{\sin\alpha}{r_1} - \frac{\mathrm{i}\cos\alpha}{r_2}\Big)\Big]\Big\}. \end{aligned} \tag{2.143}$$

Thus, using (2.140), we may write the displacement gradient as

$$\nabla\mathbf{u}^* = \Re\{\mathbf{L}(\boldsymbol{\tau}^I + p\mathbf{I})\mathbf{M}\}, \tag{2.144}$$

with corresponding strain

$$\boldsymbol{\varepsilon}^* = \frac{1}{2}(\nabla\mathbf{u}^* + \mathbf{u}^*\nabla) = \Re\{\mathbf{L}(\boldsymbol{\tau}^I + p\mathbf{I})\mathbf{M} + \mathbf{M}^T(\boldsymbol{\tau}^I + p\mathbf{I})^T\mathbf{L}^T\}, \tag{2.145}$$

where

$$\mathbf{L} = (\mathbf{K}_{21} + \mathbf{K}_{22}\mathbf{U}\Lambda\mathbf{U}^{-1})^{-1}, \tag{2.146}$$

and, from (2.140) and (2.143), we see that

$$\mathbf{M} = \frac{1}{r_1 r_2}\begin{pmatrix} \mathrm{i}(r_1^2\sin^2\alpha + r_2^2\cos^2\alpha) & r_1 r_2 - \mathrm{i}(r_1^2 - r_2^2)\sin\alpha\cos\alpha & 0 \\ -r_1 r_2 - \mathrm{i}(r_1^2 - r_2^2)\sin\alpha\cos\alpha & \mathrm{i}(r_1^2\cos^2\alpha + r_2^2\sin^2\alpha) & 0 \\ 0 & 0 & 0 \end{pmatrix}. \tag{2.147}$$

Equation (2.145) may also be written as

$$\varepsilon^*_{ij} = N_{ijk\ell}(\tau^I_{k\ell} + p\delta_{k\ell}), \tag{2.148}$$

where

$$N_{ijk\ell} = \frac{1}{2}\Re\{L_{ik}M_{\ell j} + L_{jk}M_{\ell i}\}. \tag{2.149}$$

The three matrix factors in (2.144) depend respectively on, the elastic constants of the material, the incident stress field (including the pressure p), and the geometry of the borehole profile. The constant tensor $\nabla\mathbf{u}^*$ is the uniform displacement gradient belonging to the interior problem mentioned after (2.103). The corresponding stress τ^*_{ij} is given by

$$\tau^*_{ij} = c_{ijk\gamma} u^*_{k,\gamma}. \tag{2.150}$$

Thus the operator N of (2.63) is given by

$$N(\boldsymbol{\tau}) = \Re\{(\mathbf{L}\boldsymbol{\tau}\mathbf{M})_{\alpha\alpha}\}, \tag{2.151}$$

and

$$N(\mathbf{I}) = \Re\{L_{\alpha\gamma}M_{\gamma\alpha}\} = \Re\{\mathrm{tr}(\mathbf{LM})\}. \tag{2.152}$$

Taking the borehole axis parallel to the 3-direction, we may now also write down the operator N^*_{im} of (2.105) and (2.107). Thus

$$\begin{aligned} \tau^*_{im} + p^{(0)}(\delta_{im} - \delta_{3i}\delta_{3m}) &= c_{imk\gamma}u^*_{k\gamma} + p^{(0)}(\delta_{im} - \delta_{3i}\delta_{3m}) \\ &= p^{(0)}[c_{imk\gamma}L_{k\alpha}M_{\alpha\gamma} + \delta_{im} - \delta_{3i}\delta_{3m}], \end{aligned} \tag{2.153}$$

and so

$$N^*_{im} = \Re\{c_{imk\gamma}L_{k\alpha}M_{\alpha\gamma} + \delta_{im} - \delta_{3i}\delta_{3m}\}. \tag{2.154}$$

2.6 Special Explicitly Solvable Cases

In this section the configuration is specialized so that a plane perpendicular to the borehole axis is a plane of symmetry for the anisotropic medium. When this is so the 3 × 3 elastostatic problem of Section 4 decouples into a 2 × 2 and a 1 × 1 system which may be solved analytically. Further specialization to transverse isotropy with axis parallel or perpendicular to the borehole, and finally to isotropy, enables one to calculate analytically the operators giving the coefficients in the one-dimensional acoustic system and the body-force distribution.

2.6.1 Orthorhombic Symmetry with the Borehole Parallel to an Axis

The matrix $(\mathbf{K}_{21} + \mathbf{K}_{22}\mathbf{U}\mathit{\Lambda}\mathbf{U}^{-1})^{-1}$ is generally too complicated to evaluate in a perspicuous form as a function of the elastic constants. However, when the coordinate planes are planes of material symmetry, the 3×3 matrices split into a 2×2 and a 1×1 diagonal block so that u_3 decouples from u_1 and u_2. The calculation is then manageable analytically. The c_{ijkl} are zero if any index appears an odd number of times. Thus $\mathbf{P}$ of (2.115) reduces to

$$\mathbf{P}(\eta) = \begin{pmatrix} a + c\eta^2 & (c+d)\eta & 0 \\ (c+d)\eta & c + b\eta^2 & 0 \\ 0 & 0 & e + f\eta^2 \end{pmatrix}, \tag{2.155}$$

where

$$\begin{aligned} a = c_{1111}, \quad b = c_{2222}, \quad c = c_{1212}, \\ d = c_{1122}, \quad e = c_{1313}, \quad f = c_{2323}. \end{aligned} \tag{2.156}$$

We see that $\det(\mathbf{P}(\eta))$ factors as

$$\det(\mathbf{P}(\eta)) = Q(\eta)R(\eta), \tag{2.157}$$

where

$$\begin{aligned} Q(\eta) &= (a + c\eta^2)(c + b\eta^2) - (c+d)^2\eta^2, \\ R(\eta) &= e + f\eta^2. \end{aligned} \tag{2.158}$$

We may set

$$\mathbf{U} = \begin{pmatrix} -(c+d)\eta_1 & -(c+d)\eta_2 & 0 \\ a + c\eta_1^2 & a + c\eta_2^2 & 0 \\ 0 & 0 & 1 \end{pmatrix}, \tag{2.159}$$

where η_1 and η_2 are the zeros of Q, and η_3 the zero of R, having positive imaginary parts. Thus

$$\eta_3 = \mathrm{i}\sqrt{\frac{e}{f}}. \tag{2.160}$$

We shall not need the explicit forms of η_1 and η_2. Inverting (2.159) we get

$$\mathbf{U}^{-1} = \frac{1}{\det \mathbf{U}} \begin{pmatrix} a + c\eta_2^2 & (c+d)\eta_2 & 0 \\ -(a + c\eta_1^2) & -(c+d)\eta_1 & 0 \\ 0 & 0 & \det \mathbf{U} \end{pmatrix}, \tag{2.161}$$

where

$$\det \mathbf{U} = -(c+d)(\eta_1 - \eta_2)(a - c\eta_1\eta_2). \tag{2.162}$$

Thus

$$\mathbf{U}\Lambda\mathbf{U}^{-1} = \begin{pmatrix} \dfrac{a(\eta_1 + \eta_2)}{a - c\eta_1\eta_2} & \dfrac{(c+d)\eta_1\eta_2}{a - c\eta_1\eta_2} & 0 \\ -\dfrac{(a + c\eta_1^2)(a + c\eta_2^2)}{(c+d)(a - c\eta_1\eta_2)} & \dfrac{-c\eta_1\eta_2(\eta_1 + \eta_2)}{a - c\eta_1\eta_2} & 0 \\ 0 & 0 & \eta_3 \end{pmatrix}. \tag{2.163}$$

Since the matrix splits it is advantageous to deal separately with the 2 × 2 and the 1 × 1 blocks.

2.6.2 The 2 × 2 Block

We rewrite the 2 × 2 of (2.163) as

$$\mathbf{U}\Lambda\mathbf{U}^{-1} = \frac{1}{a - c\eta_1\eta_2} \begin{pmatrix} a(\eta_1 + \eta_2) & (c+d)\eta_1\eta_2 \\ -\dfrac{(a + c\eta_1^2)(a + c\eta_2^2)}{c+d} & -c\eta_1\eta_2(\eta_1 + \eta_2) \end{pmatrix}. \tag{2.164}$$

Let us reduce the 21 entry by setting

$$a + c\eta^2 = \xi. \tag{2.165}$$

Then $Q(\eta) = 0$ implies

$$\xi[c + \frac{b(\xi - a)}{c}] - \frac{(c+d)^2(\xi - a)}{c} = 0. \tag{2.166}$$

The product of the roots of this quadratic equation in ξ is

$$\xi_1\xi_2 = (a + c\eta_1^2)(a + c\eta_2^2) = \frac{a(c+d)^2}{b}. \tag{2.167}$$

Thus (2.164) may be rewritten

$$\mathbf{U}\Lambda\mathbf{U}^{-1} = \frac{1}{a - c\eta_1\eta_2}\begin{pmatrix} a(\eta_1+\eta_2) & (c+d)\eta_1\eta_2 \\ -\dfrac{a(c+d)}{b} & -c\eta_1\eta_2(\eta_1+\eta_2) \end{pmatrix}. \tag{2.168}$$

From (2.131)

$$\mathbf{K}_{21} = \begin{pmatrix} 0 & c & 0 \\ d & 0 & 0 \\ 0 & 0 & 0 \end{pmatrix}, \ \mathbf{K}_{22} = \begin{pmatrix} c & 0 & 0 \\ 0 & b & 0 \\ 0 & 0 & f \end{pmatrix}. \tag{2.169}$$

Then, retaining only the 2×2 block,

$$\mathbf{K}_{21} + \mathbf{K}_{22}\mathbf{U}\Lambda\mathbf{U}^{-1} = \frac{c}{a - c\eta_1\eta_2}\begin{pmatrix} a(\eta_1+\eta_2) & a + d\eta_1\eta_2 \\ -(a + d\eta_1\eta_2) & -b\eta_1\eta_2(\eta_1+\eta_2) \end{pmatrix}. \tag{2.170}$$

To eliminate η_1, and η_2 we need the symmetric functions $\eta_1 + \eta_2$ and $\eta_1\eta_2$. But these are easily obtained from the equation

$$Q(\eta) = 0 \tag{2.171}$$

satisfied by η_1, and η_2. Thus

$$\eta_1^2\eta_2^2 = \frac{a}{b}, \tag{2.172}$$

and so, because η_1 and η_2 have positive imaginary parts,

$$\eta_1\eta_2 = -\sqrt{\frac{a}{b}}. \tag{2.173}$$

Also

$$\eta_1^2 + \eta_2^2 = -\frac{ab - d^2}{bc} + \frac{2d}{b}. \tag{2.174}$$

Hence

$$\begin{aligned} (\eta_1+\eta_2)^2 &= \eta_1^2 + \eta_2^2 + 2\eta_1\eta_2 \\ &= -\frac{ab-d^2}{bc} + \frac{2d}{b} - 2\sqrt{\frac{a}{b}}. \end{aligned} \tag{2.175}$$

Again, because of the disposition of η_1 and η_2 in the complex plane,

$$\eta_1 + \eta_2 = \frac{\mathrm{i}}{\sqrt{b}}\sqrt{\frac{ab-d^2}{c} + 2(\sqrt{ab}-d)}. \tag{2.176}$$

Thus, after some reduction,

$$\mathbf{K}_{21} + \mathbf{K}_{22}\mathbf{U}\mathit{\Lambda}\mathbf{U}^{-1} = \frac{1}{\sqrt{ab}+c} \times \begin{pmatrix} \mathrm{i}\sqrt{ac}\sqrt{\sqrt{ab}-d}\sqrt{\sqrt{ab}+2c+d} & c(\sqrt{ab}-d) \\ -c(\sqrt{ab}-d) & \mathrm{i}\sqrt{bc}\sqrt{\sqrt{ab}-d}\sqrt{\sqrt{ab}+2c+d} \end{pmatrix}, \tag{2.177}$$

and

$$\mathbf{L} = (\mathbf{K}_{21} + \mathbf{K}_{22}\mathbf{U}\mathit{\Lambda}\mathbf{U}^{-1})^{-1} = \frac{1}{\sqrt{ab}+d} \times \begin{pmatrix} -\mathrm{i}\sqrt{\frac{b}{c}}\sqrt{\frac{\sqrt{ab}+2c+d}{\sqrt{ab}-d}} & 1 \\ -1 & -\mathrm{i}\sqrt{\frac{a}{c}}\sqrt{\frac{\sqrt{ab}+2c+d}{\sqrt{ab}-d}} \end{pmatrix}. \tag{2.178}$$

2.6.3 The 1 × 1 Block

The calculation for the 1 × 1 block is trivial:

$$\mathbf{U}\mathit{\Lambda}\mathbf{U}^{-1} = \eta_3 = \mathrm{i}\sqrt{\frac{e}{f}}, \tag{2.179}$$

$$\mathbf{K}_{21} + \mathbf{K}_{22}\mathbf{U}\mathit{\Lambda}\mathbf{U}^{-1} = f\eta_3 = \mathrm{i}\sqrt{ef}, \tag{2.180}$$

and

$$(\mathbf{K}_{21} + \mathbf{K}_{22}\mathbf{U}\mathit{\Lambda}\mathbf{U}^{-1})^{-1} = -\frac{\mathrm{i}}{\sqrt{ef}}. \tag{2.181}$$

Thus finally

$$\mathbf{L} = \begin{pmatrix} \dfrac{-\mathrm{i}}{\sqrt{ab}+d}\sqrt{\dfrac{b(\sqrt{ab}+2c+d)}{c(\sqrt{ab}-d)}} & \dfrac{1}{\sqrt{ab}+d} & 0 \\ \dfrac{-1}{\sqrt{ab}+d} & \dfrac{-\mathrm{i}}{\sqrt{ab}+d}\sqrt{\dfrac{a(\sqrt{ab}+2c+d)}{c(\sqrt{ab}-d)}} & 0 \\ 0 & 0 & \dfrac{-\mathrm{i}}{\sqrt{ef}} \end{pmatrix}. \qquad (2.182)$$

2.6.4 The Body-Force Dipoles

Since we now have both $\mathbf{M}$ and $\mathbf{L}$ explicitly from (2.147) and (2.182) we may calculate $\mathcal{N}(\mathbf{I})$ and $\mathcal{N}^*_{im}$. From (2.152) and (2.154) we see that these depend on $\mathbf{L}$ and $\mathbf{M}$ only through the matrix product $\Re\{\mathbf{LM}\}$, which we easily find to be

$$\Re\{\mathbf{LM}\} = \frac{1}{\sqrt{ab}+d}\left[-\begin{pmatrix} 1 & 0 \\ 0 & 1 \end{pmatrix}\right.$$
$$\left. +\sqrt{\frac{\sqrt{ab}+2c+d}{\sqrt{ab}-d}}\begin{pmatrix} \sqrt{\dfrac{b}{c}}\,\dfrac{r_1^2\sin^2\alpha + r_2^2\cos^2\alpha}{r_1r_2} & -\sqrt{\dfrac{b}{c}}\,\dfrac{(r_1^2-r_2^2)\sin\alpha\cos\alpha}{r_1r_2} \\ -\sqrt{\dfrac{a}{c}}\,\dfrac{(r_1^2-r_2^2)\sin\alpha\cos\alpha}{r_1r_2} & \sqrt{\dfrac{a}{c}}\,\dfrac{r_1^2\cos^2\alpha + r_2^2\sin^2\alpha}{r_1r_2} \end{pmatrix}\right], \qquad (2.183)$$

where we have have presented the leading 2×2 block only. Equation (2.152) gives $\mathcal{N}(\mathbf{I})$ as the trace of this:

$$\mathcal{N}(\mathbf{I}) = \frac{1}{\sqrt{ab}+d}\left[-2\right.$$
$$\left. +\sqrt{\frac{\sqrt{ab}+2c+d}{\sqrt{ab}-d}}\,\frac{(\sqrt{a}r_1^2+\sqrt{b}r_2^2)\cos^2\alpha + (\sqrt{a}r_2^2+\sqrt{b}r_1^2)\sin^2\alpha}{\sqrt{c}\,r_1r_2}\right]. \qquad (2.184)$$

The expression for $\mathcal{N}^*_{im}$ in (2.154) involves contractions of tensors rather than multiplication of matrices and so, as a preliminary, we shall write the components of $\Re\{\mathbf{LM}\}$ as a 4-vector in the order 11, 12, 21, 22 and the components of $c_{imk\gamma}$ as a 6×4 matrix, and then form the matrix product of these. The order of the components in the matrix will be

$$\begin{pmatrix} c_{1111} & c_{1112} & c_{1121} & c_{1122} \\ c_{2211} & c_{2212} & c_{2221} & c_{2222} \\ c_{3311} & c_{3312} & c_{3321} & c_{3322} \\ c_{2311} & c_{2312} & c_{2321} & c_{2322} \\ c_{3111} & c_{3112} & c_{3121} & c_{3122} \\ c_{1211} & c_{1212} & c_{1221} & c_{1222} \end{pmatrix}. \tag{2.185}$$

Now we use (2.156) and the fact that the $c_{imk\gamma}$ vanish if any subscript appears an odd number of times to reduce the matrix to

$$\begin{pmatrix} a & 0 & 0 & d \\ d & 0 & 0 & b \\ c_{1133} & 0 & 0 & c_{2233} \\ 0 & 0 & 0 & 0 \\ 0 & 0 & 0 & 0 \\ 0 & c & c & 0 \end{pmatrix}. \tag{2.186}$$

Using (2.182) and (2.186) in (2.154) we find the only non-zero components of N^*_{im} are

$$\begin{aligned} N^*_{11} = & \frac{1}{\sqrt{ab}+d}\left[\sqrt{ab} - a + \sqrt{\frac{\sqrt{ab}+2c+d}{\sqrt{ab}-d}}\right. \\ & \left. \times \frac{(d\sqrt{a}r_1^2 + a\sqrt{b}r_2^2)\cos^2\alpha + (a\sqrt{b}r_1^2 + d\sqrt{a}r_2^2)\sin^2\alpha}{\sqrt{c}\,r_1 r_2}\right], \end{aligned} \tag{2.187}$$

$$\begin{aligned} N^*_{22} = & \frac{1}{\sqrt{ab}+d}\left[\sqrt{ab} - b + \sqrt{\frac{\sqrt{ab}+2c+d}{\sqrt{ab}-d}}\right. \\ & \left. \times \frac{(b\sqrt{a}r_1^2 + d\sqrt{b}r_2^2)\cos^2\alpha + (d\sqrt{b}r_1^2 + b\sqrt{a}r_2^2)\sin^2\alpha}{\sqrt{c}\,r_1 r_2}\right], \end{aligned} \tag{2.188}$$

$$\begin{aligned} N^*_{33} = & \frac{1}{\sqrt{ab}+d}\left[-(c_{1133}+c_{2233}) + \sqrt{\frac{\sqrt{ab}+2c+d}{\sqrt{ab}-d}}\right. \\ & \left. \times \frac{(c_{2233}\sqrt{a}r_1^2 + c_{1133}\sqrt{b}r_2^2)\cos^2\alpha + (c_{1133}\sqrt{b}r_1^2 + c_{2233}\sqrt{a}r_2^2)\sin^2\alpha}{\sqrt{c}\,r_1 r_2}\right], \end{aligned} \tag{2.189}$$

and

$$N^*_{12} = N^*_{21} = -\frac{\sqrt{c}(\sqrt{a}+\sqrt{b})}{\sqrt{ab}+d}\sqrt{\frac{\sqrt{ab}+2c+d}{\sqrt{ab}-d}}\frac{(r_1^2 - r_2^2)\sin\alpha\cos\alpha}{r_1 r_2}. \tag{2.190}$$

2.6.5 Transverse Isotropy: Axis in the 1-Direction

The only simplification is that

$$e = c, \quad c_{1133} = d, \quad \text{and} \quad c_{2233} = b - 2f. \tag{2.191}$$

2.6.6 Transverse Isotropy: Axis in the 3-Direction

Here the only relationships between the constants are

$$a = b, \quad e = f, \quad d = a - 2c, \quad \text{and} \quad c_{2233} = c_{1133} = g. \tag{2.192}$$

2.6.7 Isotropy

When the medium is isotropic with Lamé constants λ and μ

$$a = b = \lambda + 2\mu, \quad c = e = f = \mu, \quad c_{2233} = c_{1133} = d = \lambda. \tag{2.193}$$

Then

$$\begin{aligned} \sqrt{ab} &= \lambda + 2\mu, & \sqrt{ab} - d &= 2\mu, \\ \sqrt{ab} + 2c + d &= 2(\lambda + 2\mu) & \sqrt{ab} + d &= 2(\lambda + \mu), \end{aligned} \tag{2.194}$$

leading to

$$N(\mathbf{I}) = \frac{1}{\lambda + \mu}\left[-1 + \frac{\lambda + 2\mu}{2\mu} \cdot \frac{r_1^2 + r_2^2}{r_1 r_2}\right], \tag{2.195}$$

and

$$N_{11}^* = \frac{\lambda + 2\mu}{2\mu(\lambda + \mu)} \cdot \frac{[\lambda r_1^2 + (\lambda + 2\mu) r_2^2]\cos^2\alpha + [(\lambda + 2\mu) r_1^2 + \lambda r_2^2]\sin^2\alpha}{r_1 r_2}, \tag{2.196}$$

$$N_{22}^* = \frac{\lambda + 2\mu}{2\mu(\lambda + \mu)} \cdot \frac{[(\lambda + 2\mu) r_1^2 + \lambda r_2^2]\cos^2\alpha + [\lambda r_1^2 + (\lambda + 2\mu) r_2^2]\sin^2\alpha}{r_1 r_2}, \tag{2.197}$$

$$N_{33}^* = \frac{\lambda}{\lambda + \mu}\left[-1 + \frac{\lambda + 2\mu}{2\mu}\frac{r_1^2 + r_2^2}{r_1 r_2}\right], \tag{2.198}$$

and

$$N_{12}^* = N_{21}^* = -\frac{\lambda + 2\mu}{\lambda + \mu} \cdot \frac{r_1^2 - r_2^2}{r_1 r_2} \sin\alpha\cos\alpha. \tag{2.199}$$

2.6.8 Circular Borehole

When $r_1 = r_2$, (2.184) and (2.187) to (2.190) reduce to

$$N(\mathbf{I}) = \frac{1}{\sqrt{ab}+d}\left[-2+\sqrt{\frac{\sqrt{ab}+2c+d}{\sqrt{ab}-d}}\cdot\frac{\sqrt{a}+\sqrt{b}}{\sqrt{c}}\right], \tag{2.200}$$

and

$$N^*_{11} = \frac{1}{\sqrt{ab}+d}\left[\sqrt{ab}-a+\sqrt{\frac{\sqrt{ab}+2c+d}{\sqrt{ab}-d}}\cdot\frac{d\sqrt{a}+a\sqrt{b}}{\sqrt{c}}\right], \tag{2.201}$$

$$N^*_{22} = \frac{1}{\sqrt{ab}+d}\left[\sqrt{ab}-a+\sqrt{\frac{\sqrt{ab}+2c+d}{\sqrt{ab}-d}}\cdot\frac{b\sqrt{a}+d\sqrt{b}}{\sqrt{c}}\right], \tag{2.202}$$

$$N^*_{33} = \frac{1}{\sqrt{ab}+d}\left[-(c_{1133}+c_{2233})+\sqrt{\frac{\sqrt{ab}+2c+d}{\sqrt{ab}-d}}\cdot\frac{c_{2233}\sqrt{a}+c_{1133}\sqrt{b}}{\sqrt{c}}\right], \tag{2.203}$$

and N^*_{12} and N^*_{21} vanish.

2.6.9 The $N(\mathbf{I})$ and $\mathbf{N}^*$ for the Isotropic, Circular Case

Specializing (2.195) to (2.199) by setting $r_1 = r_2$ we get

$$N(\mathbf{I}) = \frac{1}{\mu}, \tag{2.204}$$

$$\mathbf{N}^* = \begin{pmatrix} \frac{\lambda+2\mu}{\mu} & 0 & 0 \\ 0 & \frac{\lambda+2\mu}{\mu} & 0 \\ 0 & 0 & \frac{\lambda}{\mu} \end{pmatrix}, \tag{2.205}$$

which may be written as

$$\mathbf{N}^* = \begin{pmatrix} \frac{v_c^2}{v_s^2} & 0 & 0 \\ 0 & \frac{v_c^2}{v_s^2} & 0 \\ 0 & 0 & \frac{v_c^2}{v_s^2}-2 \end{pmatrix}, \tag{2.206}$$

where v_c and v_s are the compressional and shear wave speeds in the isotropic medium. They are given by

$$v_c^2 = \frac{\lambda + 2\mu}{\rho}, \quad v_s^2 = \frac{\mu}{\rho}. \tag{2.207}$$

Equations (2.204)-(2.206) agree with the results of previous authors (White, 1983; Lee and Balch, 1982).

2.7 Discussion and Conclusions

We have set up a formalism for calculating the seismic radiation from a borehole asymptotically in the limit as the ratio of the borehole diameter to wavelength goes to zero. In this limit an acoustic source in the borehole acts indirectly as a seismic source. The source first generates a tube wave, which is an acoustic wave in the fluid filling the borehole, and the pressure field of the tube wave, by distorting the borehole wall, in turn generates the seismic wave. The action of the tube wave is equivalent in the narrow borehole approximation, to a line distribution of body force along the borehole centerline and acting in the intact elastic solid, *i.e.,* the solid with no borehole in it. We have found expressions for this source distribution, which turn out to be a distribution of dipoles.

In previous work the asymptotic limit of a narrow hole was calculated by taking the low frequency approximation to an exact solution for a circular cylindrical hole in an isotropic medium. By directly calculating the asymptotic limit, one is able to find these body-force equivalents and other aspects of the solution in quite general circumstances, without the need for exact solutions. In fact, we have found the asymptotic solution for a curved hole with elliptic cross-section in an arbitrary anisotropic medium. When these results are specialized to right circularly cylindrical holes in an isotropic medium, they agree with previous work in the literature.

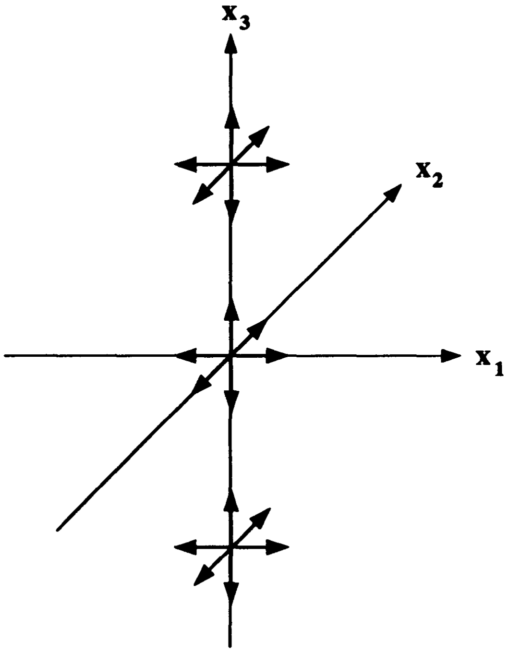

Figure 2.1: Symmetrical distribution of dipoles for a straight borehole, corresponding to the integrand in equation (2.107).

Chapter 3

Radiation from a Source in a Borehole

3.1 Introduction

Recently there has been much interest in cross-well tomography in which sources are placed in one borehole and receivers in another. One may think of the sources acting on the solid only through a tube wave as an intermediary, and reciprocally, the receivers reponding to the seismic wave only through intermediate tube waves excited in the second well. Thus it is important to understand the interaction between the tube wave and the seismic wave. Moreover, the recent emphasis on anisotropy requires that the solid not be restricted to isotropy. Also, the existence of horizontal and deviated wells means that we cannot assume that the borehole has any particularly symmetrical orientation with respect to the symmetry planes of the anisotropic medium or that the borehole has a circular cross-section, especially along highly curved sections.

In this chapter we quote a form for the far-field Green's function in an anisotropic medium, and then combine it with the body force distribution derived in the previous chapter to calculate the far field. Results are obtained for situations where the tube wave is either faster or slower than the quasi-shear waves. The case of two boreholes with a source in one well and a receiver in the other well is also analysed. The solution is obtained in a form which clearly exhibits reciprocity.

Next, the far field is first specialized to a circular borehole in an isotropic medium, and shown to be identical to those of Lee and Balch (1982) and Ben-Menahem and Kostek (1991). Then, the nontrivial case of a borehole in a transversely isotropic medium is considered, where we show the radiation patterns and wavefront surfaces for various situations involving media with symmetry axis parallel or perpendicular to the borehole axis, and also with triplication of the quasi-shear wavefront.

3.2 The Far-Field Radiation Pattern

In this section we shall calculate the seismic far field generated by the pressure field calculated in Section 2.3.5 for an acoustic volume source in the borehole. We shall need N^*_{im} from (2.154) and the equivalent source distribution of body-force dipoles given in (2.107), we shall also need the far field Green's function in the anisotropic medium, and finally we shall integrate the Green's function against the source distribution to obtain the far field.

3.2.1 The Green's Function

We shall now calculate the seismic field radiated by the source distribution of Equation (2.107). The far-field Green's function for a uniform anisotropic medium is given in Burridge (1967). In order to understand that result we shall need some background. We shall consider plane waves of the form

$$\mathbf{u} = \mathbf{P}(\boldsymbol{\xi}) f(t - \boldsymbol{\xi} \cdot \mathbf{x}), \tag{3.1}$$

where the constant vectors $\boldsymbol{\xi}$ and $\mathbf{P}(\boldsymbol{\xi})$ are the wave slowness and the polarization, respectively. For (3.1) to satisfy the elastic wave equation, $\boldsymbol{\xi}$ must be restricted to lie on a 3-sheeted surface S called the slowness surface. Each of the three sheets of S surrounds the origin. The vector $\mathbf{P}$ must be an eigenvector of a certain symmetric matrix whose entries are quadratic polynomials in $\boldsymbol{\xi}$ with elastic constants as coefficients. We shall normalize $\mathbf{P}$ to be a unit vector. Then in the far field (Burridge, 1976; Section

6), the Green's function $\mathbf{G}(\mathbf{x},t;\mathbf{x}',t')$ is given by

$$G_{ij}(\mathbf{x},t;\mathbf{x}',t') = \sum_{\boldsymbol{\xi}} \frac{P_i(\boldsymbol{\xi})P_j(\boldsymbol{\xi})\boldsymbol{\xi}\cdot(\mathbf{x}-\mathbf{x}')}{4\pi|C(\boldsymbol{\xi})|^{\frac{1}{2}}|\mathbf{x}-\mathbf{x}'|^2}\delta^*[t-t'-\boldsymbol{\xi}\cdot(\mathbf{x}-\mathbf{x}')]. \tag{3.2}$$

For fixed $\mathbf{x}$, t', $\boldsymbol{\xi}$ and with t increasing from t', each of the planes

$$\boldsymbol{\xi}\cdot(\mathbf{x}-\mathbf{x}') = t - t' \tag{3.3}$$

in $\boldsymbol{\xi}$-space is orthogonal to $\mathbf{x}-\mathbf{x}'$ and its distance from the origin is

$$\frac{t-t'}{|\mathbf{x}-\mathbf{x}'|}. \tag{3.4}$$

When $t = t'$ the plane (3.3) passes through the origin and intersects all the sheets of S. For large $t - t'$ the plane is outside S and does not intersect it. For certain values of t the plane is tangent to S at certain points $\boldsymbol{\xi}$ (see Figure 3.1). These are the points $\boldsymbol{\xi}$ over which the sum is taken in (3.2). If these points $\boldsymbol{\xi}$ are points where S is smooth then they may be characterized as the points where the outward normal to S is parallel to $\mathbf{x}-\mathbf{x}'$. For each such point $\boldsymbol{\xi}$, (3.2) yields a singular wavefield arrival with time dependence

$$\delta^*[t-t'-\boldsymbol{\xi}\cdot(\mathbf{x}-\mathbf{x}')], \tag{3.5}$$

where

$$\delta^* = \begin{cases} \delta, & \text{if } S \text{ is convex outward at } \boldsymbol{\xi}; \\ -\mathcal{H}\delta, & \text{if } S \text{ is saddle shaped at } \boldsymbol{\xi}; \\ -\delta, & \text{if } S \text{ is concave outward at } \boldsymbol{\xi}. \end{cases} \tag{3.6}$$

Here $\mathcal{H}$ is the Hilbert transform. The quantity $C(\boldsymbol{\xi})$ in (3.2) is the Gaussian curvature of S at $\boldsymbol{\xi}$. It is respectively positive, negative, and positive in the three cases of (3.6). Formula (3.2) does not apply when $C(\boldsymbol{\xi}) = 0$ at any of the $\boldsymbol{\xi}$. Then a further more complicated expression for that particular term is required, which we shall not describe. It corresponds to a cuspidal edge on the wavefront and is akin to the expression for the wavefield near a caustic. Such points arise when the sheets of S fail to be convex.

Notice that each term of (3.2) has the form

$$G_{ij}(\mathbf{x},t;\mathbf{x}',t') = F_{ij}(\mathbf{x},\mathbf{x}')\delta[t-t'-\boldsymbol{\xi}\cdot(\mathbf{x}-\mathbf{x}')], \tag{3.7}$$

where F_{ij} is a smooth function of $\mathbf{x}, \mathbf{x}'$ away from $\mathbf{x} = \mathbf{x}'$, which never holds in the far field. If the medium is not homogeneous then G_{ij} has a similar structure in the ray theoretical approximation when no ray focussing occurs:

$$G_{ij}(\mathbf{x}, t; \mathbf{x}', t') = F_{ij}(\mathbf{x}, \mathbf{x}')\delta[t - t' - T(\mathbf{x}, \mathbf{x}')], \tag{3.8}$$

where F_{ij} and T are smooth functions, T being the characteristic travel time along the ray joining $\mathbf{x}$ and $\mathbf{x}'$. Since (2.107) is a distribution of dipoles we shall need the gradient of G with respect to $\mathbf{x}'$:

$$G_{ij,x'_k}(\mathbf{x}, t; \mathbf{x}', t') = \partial_{x'_k} G_{ij}(\mathbf{x}, t; \mathbf{x}', t') = -F_{ij}(\mathbf{x}, \mathbf{x}')T_{,x'_k}\delta'[t - t' - T(\mathbf{x}, \mathbf{x}')]. \tag{3.9}$$

But $-T_{,x'_k}$ is just the wave slowness for the ray at $\mathbf{x}'$. Let us write

$$\xi'_k = -T_{,x'_k}. \tag{3.10}$$

Then

$$G_{ij,x'_k} = F_{ij}\xi'_k\delta'[t - t' - T(\mathbf{x}, \mathbf{x}')]. \tag{3.11}$$

3.2.2 The Far Field

The far field radiated by the source of (2.107) may be written as a sum of terms like

$$\begin{aligned} u_i^{\boldsymbol{\xi}}(\mathbf{x}, t) &= \int\int f_j(\mathbf{x}', t')G_{ij,x'_k}(\mathbf{x}, t; \mathbf{x}', t')\,\mathrm{d}\mathbf{x}'\,\mathrm{d}t' \\ &= \int\int\int A(s)N^*_{jm}(s)p^{(0)}(s, t')\delta_{,m}[\mathbf{x}' - \mathbf{X}(s)]\,\mathrm{d}s\, G_{ij,x'_k}(\mathbf{x}, t; \mathbf{x}', t')\,\mathrm{d}\mathbf{x}'\,\mathrm{d}t' \\ &= \int\int A(s)N^*_{jm}(s)p^{(0)}(s, t')F_{ij}[\mathbf{x}, \mathbf{X}(s)]\xi'_m\delta'[t - t' - T(\mathbf{x}, \mathbf{X}(s))]\,\mathrm{d}s\,\mathrm{d}t', \end{aligned} \tag{3.12}$$

where we have performed the $\mathbf{x}'$ integration and used (3.11). Now the superscript $\boldsymbol{\xi}$ labels the different ray contributions. Performing the t' integral we obtain

$$u_i^{\boldsymbol{\xi}}(\mathbf{x}, t) = \int A(s)N^*_{jm}(s)p^{(0)}[s, t - T(\mathbf{x}, \mathbf{X}(s))]F_{ij}[\mathbf{x}, \mathbf{X}(s)]\xi'_m\,\mathrm{d}s, \tag{3.13}$$

and then using (2.88) we get

$$\begin{aligned} u_i^{\boldsymbol{\xi}}(\mathbf{x},t) &= \int \frac{V_0 A(s)}{2A(0)} N^*_{jm}(s)\zeta^{\frac{1}{2}}(0)\zeta^{\frac{1}{2}}(s) \\ &\quad \times g''[t - \mathrm{sgn}(s)\int_0^s \gamma_T(s')\,\mathrm{d}s' - T(\mathbf{x},\mathbf{X}(s))]F_{ij}[\mathbf{x},\mathbf{X}(s)]\xi'_m\,\mathrm{d}s. \qquad (3.14) \end{aligned}$$

It is convenient to write this integral in the form

$$\begin{aligned} \int_{-\infty}^{+\infty} G(s)g''[t-\phi(s)]\,\mathrm{d}s &= \int_{-\infty}^{+\infty} G(s)\delta[t-\phi(s)]\,\mathrm{d}s *_t g''(t) \\ &= I(t) *_t g''(t), \qquad (3.15) \end{aligned}$$

say. We shall now investigate $I(t)$, which appears to represent the response to $g''(t) = \delta(t)$, i.e. $g(t) = tH(t)$, where H is the Heaviside step function. However, because of the restriction to slow time variation, (3.15) is only relevant when g varies slowly and smoothly in time. Because of the occurrence of δ in I we may evaluate the integral

$$\begin{aligned} I(t) &= \int G(s)\delta[t-\phi(s)]\,\mathrm{d}s \\ &= \sum_{\{s|\phi(s)=t\}} \frac{G(s)}{|\phi'(s)|}, \qquad (3.16) \end{aligned}$$

where the sum extends over all values of s for which $\phi(s) = t$. We shall assume for simplicity that $\phi(s)$ has only one local minimum s_0. We shall distinguish two cases: $s_0 = 0$, and $s_0 \neq 0$, in which case we shall assume for definiteness that $s_0 > 0$. In fast formations, for which $\gamma_T > \boldsymbol{\xi}' \cdot \mathbf{t}$, $s_0 = 0$. In slow formations this inequality may fail for some positions of the receiver, and at $s = 0$ we may have $\gamma_T < \boldsymbol{\xi}' \cdot \mathbf{t}$. We shall consider these two cases separately. We shall see that when $s_0 = 0$ the only geometrical wave arrival emanates from the source point $s = 0$. When $s_0 > 0$ there are two arrivals, one of which emanates from the source, but there is an earlier "conical" wave arrival corresponding to the point s_0.

Let us now examine the function ϕ

$$\begin{aligned} \phi(s) &= \mathrm{sgn}(s)\int_0^s \gamma_T(s')\,\mathrm{d}s' + T(\mathbf{x},\mathbf{X}(s)) \\ &= \phi_1(s) + \phi_2(s), \end{aligned} \qquad (3.17)$$

say. Thus

$$\phi_1'(s) = \operatorname{sgn}(s)\gamma_T(s), \quad \phi_2'(s) = -\boldsymbol{\xi}' \cdot \mathbf{t}. \tag{3.18}$$

For a fast formation $\gamma_T > \boldsymbol{\xi}' \cdot \mathbf{t}$ at $s = 0$, so that $\phi = \phi_1 + \phi_2$ has the form shown in Figure 3.2. In this case $\phi(s)$ has a unique minimum at $s = 0$ with

$$\begin{aligned} \phi'(-0) &= -[\gamma_T + \boldsymbol{\xi}' \cdot \mathbf{t}]_{s=0} < 0, \\ \phi'(+0) &= [\gamma_T - \boldsymbol{\xi}' \cdot \mathbf{t}]_{s=0} > 0. \end{aligned} \tag{3.19}$$

Thus for $t < \phi(0)$ there are no terms in the sum (3.16) and $I(t) = 0$. When $t > \phi(0)$ there are two values, $s_1 < 0$ and $s_2 > 0$, of s for which $\phi(s) = t$, and from (3.16) we may write

$$I(t) = \frac{G(s_1)}{\gamma_T(s_1) + \boldsymbol{\xi}(s_1)' \cdot \mathbf{t}(s_1)} + \frac{G(s_2)}{\gamma_T(s_2) - \boldsymbol{\xi}(s_2)' \cdot \mathbf{t}(s_2)}. \tag{3.20}$$

At $t = \phi(0) + 0$

$$\begin{aligned} I(t) &= G(0)\left(\frac{1}{\gamma_T(0) + \boldsymbol{\xi}(0)' \cdot \mathbf{t}(0)} + \frac{1}{\gamma_T(0) - \boldsymbol{\xi}(0)' \cdot \mathbf{t}(0)}\right), \\ &= \frac{2G(0)\gamma_T(0)}{\gamma_T(0)^2 - (\boldsymbol{\xi}(0)' \cdot \mathbf{t}(0))^2}, \end{aligned} \tag{3.21}$$

and so $I(t)$ jumps by this amount at $t = \phi(0)$ and is smooth elsewhere. $I(t)$ therefore has a graph as shown in Figure 3.3. In a slow formation, let us suppose that for the field point under consideration $s_0 > 0$. The graph of ϕ is as in Figure 3.4. Then $\phi(s_0) < \phi(0)$ and for $t < \phi(s_0)$ there are no s for which $\phi(s) = t$, and so the sum (3.16) is vacuous. For $t > \phi(s_0)$ there are two such s, $s_1 < s_0$ and $s_2 > s_0$. When $t - \phi(s_0) > 0$ is small then $|s_i - s_0|$, $i = 1, 2$, are both small and we have approximately

$$\begin{aligned} \phi(s_i) - \phi(s_0) &= \tfrac{1}{2}\phi''(s_0)(s_i - s_0)^2, \\ \phi'(s_i) &= \phi''(s_0)(s_i - s_0). \end{aligned} \tag{3.22}$$

Then approximately for $i = 1, 2$

$$\phi'(s_i) = \operatorname{sgn}(s_i - s_0)\sqrt{2\phi''(s_0)[\phi(s_i) - \phi(s_0)]}. \tag{3.23}$$

Thus for $t > \phi(s_0)$, $I(t)$ has a reciprocal square-root singularity

$$I(t) = \sqrt{\frac{2}{\phi''(s_0)[t - \phi(s_0)]}}\,G(s_0) + O([t - \phi(s_0)]^{\frac{1}{2}}). \tag{3.24}$$

At $t = \phi(0) - 0$, $s = +0$ and

$$|\phi'(+0)| = \boldsymbol{\xi}(0)' \cdot \mathbf{t}(0) - \gamma_T(0). \tag{3.25}$$

At $t = \phi(0) + 0$, $s = -0$ and

$$|\phi'(-0)| = \boldsymbol{\xi}(0)' \cdot \mathbf{t}(0) + \gamma_T(0). \tag{3.26}$$

Thus at $t = \phi(0)$, $I(t)$ jumps by

$$\begin{aligned} I(\phi(0)+0) - I(\phi(0)-0) &= G(0)\left(\frac{1}{\gamma_T + \boldsymbol{\xi}(0)' \cdot \mathbf{t}(0)} + \frac{1}{\gamma_T - \boldsymbol{\xi}(0)' \cdot \mathbf{t}(0)}\right) \\ &= \frac{2G(0)\gamma_T}{\gamma_T^2 - (\boldsymbol{\xi}(0)' \cdot \mathbf{t}(0))^2} < 0. \end{aligned} \tag{3.27}$$

The graph of $I(t)$ is now as shown in Figure 3.5.

We notice that formulae (3.21) and (3.27) are identical. Thus in all cases there is an arrival corresponding to the jump discontinuity, which seems to emanate from the source point. On referring back to (3.14) we identify $G(0)$ and then, interpreting convolution with a step function as integration, we obtain

$$u_i(\mathbf{x},t) = \sum_{\boldsymbol{\xi}} u_i^{\boldsymbol{\xi}}(\mathbf{x},t) = \sum_{\boldsymbol{\xi}} \frac{\rho_f V_0 N_{jm}^*(0) F_{ij}(\mathbf{x},\mathbf{0})\xi_m'}{\gamma_T^2 - (\boldsymbol{\xi}' \cdot \mathbf{t})^2} g'[t - T(\mathbf{x},\mathbf{0})]. \tag{3.28}$$

For a uniform medium we may identify $F_{ij}\xi_m'$ by comparing (3.7) and (3.2). Thus

$$F_{ij}(\mathbf{x},0) = \frac{P_i(\boldsymbol{\xi})P_j(\boldsymbol{\xi})\boldsymbol{\xi} \cdot \mathbf{x}}{4\pi\rho|C(\boldsymbol{\xi})|^{\frac{1}{2}}|\mathbf{x}|^2}, \quad \xi_m' = \xi_m, \tag{3.29}$$

and so the wave arrival which emanates from the source is

$$u_i(\mathbf{x},t) = \sum_{\boldsymbol{\xi}} \frac{\rho_f V_0 N_{jm}^*(0) P_i(\boldsymbol{\xi})P_j(\boldsymbol{\xi})\boldsymbol{\xi} \cdot \mathbf{x}\xi_m}{4\pi\rho|C(\boldsymbol{\xi})|^{\frac{1}{2}}|\mathbf{x}|^2[\gamma_T^2 - (\boldsymbol{\xi} \cdot \mathbf{t})^2]} g'[t - T(\mathbf{x},\mathbf{0})]. \tag{3.30}$$

In addition, in slow formations and at certain positions of the source, there will be an arrival corresponding to the stationary point s_0 with a pulse shape which is the fractional derivative of order $\frac{1}{2}$ of the g' appearing in (3.30). This pulse shape arises by convolution of g'' with the reciprocal square root. In the isotropic case this arrival has a circular conical wave front. Explicitly we may write this contribution in the form

$$\begin{aligned} u_i(\mathbf{x},t) &= \sum_{\boldsymbol{\xi}} \frac{V_0 A(s_0) N^*_{jm}(s_0) \zeta^{\frac{1}{2}}(0) \zeta^{\frac{1}{2}}(s_0) P_i(\boldsymbol{\xi}) P_j(\boldsymbol{\xi}) \boldsymbol{\xi} \cdot \mathbf{x} \xi_m}{8\pi\rho A(0) |C(\boldsymbol{\xi})|^{\frac{1}{2}} |\mathbf{x}|^2} \sqrt{\frac{2}{\phi''(s_0)}} \\ &\qquad \times \int \frac{1}{[t - t' - \phi(s_0)]^{\frac{1}{2}}} g''(t')\, \mathrm{d}t'. \end{aligned} \tag{3.31}$$

The slowness $\boldsymbol{\xi}$ must be evaluated at the point $s = s_0$ and the quantity $\phi''(s_0)$ may be evaluated explicitly for isotropic media and will then be proportional to $|\mathbf{x}|^{-1}$. The sum in (3.31) is over only those $\boldsymbol{\xi}$ for which $\boldsymbol{\xi}(0)' \cdot \mathbf{t}(0) - \gamma_T(0) > 0$. Typically this will only happen for the (quasi-)S waves.

3.2.3 The Two-Borehole Problem

We consider now the problem of a source in one well and a receiver in another well. The source is of a volume injection type, supplying accumulated volume $V_0 g(t)$ up to time t, and the receiver is sensitive to pressure. For simplicity, we will assume that the medium surrounding the boreholes is homogeneous but anisotropic. The boreholes need not be straight, and the distance between them is $O(1/\epsilon^2)$. The one-dimensional acoustic system in the receiver borehole follows from (2.66), (2.68), and (2.69), with the source term G set to zero. This leads to

$$(\sigma^R + N^R(\mathbf{I}))p^{(0)}_{,t} + v^{(0)}_{3,s} = -[\delta_{ij} - t_i t_j + (\delta_{mn} - t_m t_n) N^R_{mnpq} c_{pqij}] u^{I(0)}_{i,jT}, \tag{3.32}$$

$$\rho^R_f v^{(0)}_{3,t} + p^{(0)}_{,s} = 0, \tag{3.33}$$

where s is the arclength along the receiver borehole, and the superscript R indicates quantities related to the receiver as opposed to the source. We will use the superscript S in relation to the source. The incident field $u^{I(0)}_i(\mathbf{x}(s),t)$ in the case of a fast formation (with respect to the source borehole) is as given by (3.30), which we repeat here

$$u^{I(0)}_i(\mathbf{x}(s),t) = \sum_{\boldsymbol{\xi}(s)} \frac{\rho^S_f V_0 N^{*S}_{jm}(0) P_i(\boldsymbol{\xi}(s)) P_j(\boldsymbol{\xi}(s)) \boldsymbol{\xi}(s) \cdot \mathbf{x}(s) \xi_m(s)}{4\pi\rho |C(\boldsymbol{\xi}(s))|^{\frac{1}{2}} |\mathbf{x}(\mathbf{s})|^2 [(\gamma^S_T)^2 - (\boldsymbol{\xi}(s) \cdot \mathbf{t}^S)^2]} g'[t - T_1(\mathbf{x}(s), \mathbf{0})], \tag{3.34}$$

where $\boldsymbol{\xi}(s)$ is such that $\boldsymbol{\xi}(s)\cdot\mathbf{x}(s) = t$, and $T_1(\mathbf{x}(s), \mathbf{0})$ is the travel time from the source to the point $\mathbf{x}(s)$ which is along the receiver borehole.

Following (2.105) and the reciprocity relation (A.10) from the Appendix A, Equation (3.32) can be rewritten as

$$(\sigma^R + N^R(\mathbf{I}))p^{(0)}_{,t} + v^{(0)}_{3,s} = -N^{*R}_{ij}(s)u^{I(0)}_{i,jT}(\mathbf{x}(s), t). \tag{3.35}$$

The solution of (3.33) and (3.35) follows from the results of Section 2.3. The pressure is thus given by

$$p^{(0)}(s,t) =$$

$$-\int_{-\infty}^{+\infty} \sum_{\boldsymbol{\xi}} \frac{\rho_f^S V_0 N^{*S}_{km}(0) N^{*R}_{ij}(s') P_i(\boldsymbol{\xi}(s')) P_k(\boldsymbol{\xi}(s')) \xi_m(s') \xi_j(s') \boldsymbol{\xi}(s) \cdot \mathbf{x}(s) [\zeta^R(s')\zeta^R(s)]^{\frac{1}{2}}}{8\pi\rho |C(\boldsymbol{\xi}(s'))|^{\frac{1}{2}} |\mathbf{x}(s')|^2 [(\gamma_T^S)^2 - (\boldsymbol{\xi}(s)\cdot\mathbf{t}^S)^2]}$$

$$\times\, \delta(t - T_1(\mathbf{x}(s'), \mathbf{0}) - T_2(s, s')) *_t g'''(t)\, \mathrm{d}s', \tag{3.36}$$

where $T_2(s, s')$ is the tube wave travel time from s' to s in the receiver borehole. Using the result obtained in (3.15) and (3.16) for the integral over s', we finally obtain

$$p^{(0)}(s,t) = \sum_{\boldsymbol{\xi}} \frac{\rho_f^S \rho_f^R V_0 N^{*S}_{km}(0) N^{*R}_{ij}(s) P_i(\boldsymbol{\xi}(s)) P_k(\boldsymbol{\xi}(s)) \xi_m(s) \xi_j(s) \boldsymbol{\xi}(s) \cdot \mathbf{x}(s)}{4\pi\rho |C(\boldsymbol{\xi}(s))|^{\frac{1}{2}} |\mathbf{x}(s)|^2 [(\gamma_T^S)^2 - (\boldsymbol{\xi}(s)\cdot\mathbf{t}^S)^2][(\gamma_T^R)^2 - (\boldsymbol{\xi}(s)\cdot\mathbf{t}^R)^2]}$$

$$\times g''(t - T_1(\mathbf{x}(s), \mathbf{0})). \tag{3.37}$$

If the tube wave in either borehole is faster than the body wave under consideration, then there will be additional "conical" wave arrivals which we shall not treat here. If the slowness surface is not convex at $\boldsymbol{\xi}$, however, we may replace g'' by $g^{*\prime\prime}$ where, in keeping with (3.6),

$$g^* = \begin{cases} g, & \text{if } S \text{ is convex outward at } \boldsymbol{\xi}; \\ -\mathcal{H}g, & \text{if } S \text{ is saddle shaped at } \boldsymbol{\xi}; \\ -g, & \text{if } S \text{ is concave outward at } \boldsymbol{\xi}. \end{cases} \tag{3.38}$$

3.3 Some Examples

In this section we shall illustrate the results obtained in the previous sections with examples of boreholes in isotropic and transversely isotropic homogeneous formations.

3.3.1 Circular Borehole in a Homogeneous Isotropic Medium

We consider a straight borehole of circular cross section of radius r_0 penetrating a homogeneous isotropic formation characterized by a volume density of mass ρ and Lamé parameters λ and μ. The compressional and shear wave speeds in the solid are v_c and v_s, as given in (2.207). The density of the fluid in the borehole is ρ_f and its wave speed v_f is given by

$$\frac{1}{v_f^2} = \rho_f \sigma, \tag{3.39}$$

[see (2.10) and (2.11)]. Under these conditions, the expression for the equivalent body force system [Equation (2.107)] reduces to

$$f_i(\mathbf{x}, t) = -AN^*_{im} \int p^{(0)}(x_3', t)\delta_{,m}(\mathbf{x} - \mathbf{X}(x_3'))\mathrm{d}x_3', \tag{3.40}$$

where $A = \pi r_0^2$, the borehole axis is taken as $\mathbf{X}(x_3) = (0, 0, x_3)$, and the tensor $\mathbf{N}^*$ is given in (2.206), which we repeat here:

$$\mathbf{N}^* = \begin{pmatrix} v_c^2/v_s^2 & 0 & 0 \\ 0 & v_c^2/v_s^2 & 0 \\ 0 & 0 & v_c^2/v_s^2 - 2 \end{pmatrix}. \tag{3.41}$$

The far-field displacements can be computed from (3.30). We first notice that due to the homogeneity of the medium we have $\boldsymbol{\xi} = \boldsymbol{\xi}'$. Furthermore, due to isotropy there are only two $\boldsymbol{\xi}$ vectors, namely $\boldsymbol{\xi}_c = \mathbf{x}/v_c|\mathbf{x}|$ and $\boldsymbol{\xi}_s = \mathbf{x}/v_s|\mathbf{x}|$. The Gaussian curvatures associated with these vectors are $C(\boldsymbol{\xi}_c) = 1/v_c^2$ and $C(\boldsymbol{\xi}_s) = 1/v_s^2$, and the polarization vectors are $\mathbf{P}(\boldsymbol{\xi}_c) = \mathbf{x}/|\mathbf{x}|$ and $\mathbf{P}(\boldsymbol{\xi}_s) = \mathbf{y}/|\mathbf{y}|$ where $\mathbf{y} = \mathbf{x} \times (\mathbf{e}_3 \times \mathbf{x})$. The third polarization corresponding to SH-waves is not excited due to the circular symmetry of the borehole. Finally from (2.77), (2.204), and (3.39) we have $\gamma_T = 1/v_T = \sqrt{1/v_f^2 + \rho_f/\rho v_s^2}$. The far-field displacements are then given by

$$\begin{aligned} u_i(\mathbf{x}, t) \;\; = \;\; & -\frac{\rho_f V_0 \gamma_i}{4\pi\rho} \left[\frac{1}{v_c^3} \frac{(v_c^2/v_s^2 - 2\cos^2\varphi)}{(\cos^2\varphi/v_c^2 - 1/v_T^2)} \frac{g'(t - |\mathbf{x}|/v_c)}{|\mathbf{x}|} \right. \\ & \left. + \frac{1}{v_s^3} \frac{(N^*_{\underline{ii}} - v_c^2/v_s^2 + 2\cos^2\varphi)}{(\cos^2\varphi/v_s^2 - 1/v_T^2)} \frac{g'(t - |\mathbf{x}|/v_s)}{|\mathbf{x}|} \right], \end{aligned} \tag{3.42}$$

where the summation convention is suppressed for underlined indices, and $\gamma_i = \mathbf{x} \cdot \mathbf{e}_i$ $(i = 1, 2, 3)$ with $\gamma_3 = \cos\varphi$. The far-field displacements in terms of spherical coordinates (R, φ, θ) can be computed from

$$\begin{aligned} u_R &= \gamma_i u_i, && (3.43) \\ u_\varphi &= \sqrt{u_1^2 + u_2^2}\,\gamma_3 - u_3\sqrt{1-\gamma_3^2}, && (3.44) \end{aligned}$$

resulting in the following expressions

$$\begin{aligned} u_R(R,\varphi,\theta,t) &= \frac{\rho_f v_T^2 V_0}{4\pi\rho v_c v_s^2}\,\frac{(1-2v_s^2\cos^2\varphi/v_c^2)}{(1-v_T^2\cos^2\varphi/v_c^2)}\,\frac{g'(t-R/v_c)}{R}, && (3.45) \\ u_\varphi(R,\varphi,\theta,t) &= \frac{\rho_f v_T^2 V_0}{2\pi\rho v_s^3}\,\frac{\sin\varphi\cos\varphi}{(1-v_T^2\cos^2\varphi/v_s^2)}\,\frac{g'(t-R/v_s)}{R}, && (3.46) \end{aligned}$$

where $R = (\mathbf{x} \cdot \mathbf{x})^{1/2}$. These expressions agree with the ones given by Lee and Balch (1982), who derived them by using a stationary phase approximation to the exact integral expression for the displacements induced by a point source inside a fluid-filled borehole.

3.3.2 Distributed Versus Localized Sources Along the Borehole

The equivalent force system given by (3.40) consists of three mutually orthogonal dipoles moving along the borehole axis at the tube wave speed. Carrying out the integration indicated in (3.40) we obtain

$$\mathbf{f}(\mathbf{x},t) = -\pi r_0^2 \begin{pmatrix} N_{11}^*\, p^{(0)}(x_3,t)\delta'(x_1)\delta(x_2) \\ N_{22}^*\, p^{(0)}(x_3,t)\delta(x_1)\delta'(x_2) \\ N_{33}^*\, p_{,3}^{(0)}(x_3,t)\delta(x_1)\delta(x_2) \end{pmatrix}. \qquad (3.47)$$

The pressure field $p^{(0)}(x_3,t)$ can be further expanded in terms of multipoles by testing it with a scalar function $\phi(x_3)$ and using the distributional definition of the derivatives

$$\begin{aligned} I &= \int_{-\infty}^{+\infty} p^{(0)}(x_3,t)\phi(x_3)\,\mathrm{d}x_3 \\ &= \int_{-\infty}^{+\infty} p^{(0)}(x_3,t)\left(\sum_{n=0}^{\infty}\phi^{(n)}(0)\frac{x_3^n}{n!}\right)\mathrm{d}x_3. && (3.48) \end{aligned}$$

From (2.88) we obtain

$$p^0(x_3,t) = \frac{\rho_f v_T V_0}{2A} g'(t - \frac{|x_3|}{v_T}), \tag{3.49}$$

which substituted into (3.48) gives

$$\begin{aligned} I &= \frac{\rho_f v_T V_0}{2A} \sum_{n=0}^{\infty} \phi^{(n)}(0) \int_{-\infty}^{+\infty} \frac{x_3^n}{n!}\, g'(t - \frac{|x_3|}{v_T})\, \mathrm{d}x_3 \\ &= \frac{\rho_f v_T V_0}{A} \sum_{m=0}^{\infty} \phi^{(2m)}(0) \int_0^{\infty} \frac{x_3^{2m}}{(2m)!}\, g'(t - \frac{x_3}{v_T})\, \mathrm{d}x_3 \\ &= \frac{\rho_f v_T V_0}{A} \sum_{m=0}^{\infty} v_T^{2m+1} \phi^{(2m)}(0) \int_0^{\infty} \frac{y^{2m}}{(2m)!}\, g'(t - y)\, \mathrm{d}y. \end{aligned} \tag{3.50}$$

The first term in the above expansion corresponding to $m = 0$ is simply given by

$$\begin{aligned} I^{(0)} &= \frac{\rho_f v_T^2 V_0}{A} \phi(0) g(t) \\ &= \int_{-\infty}^{+\infty} \frac{\rho_f v_T^2 V_0}{A} g(t) \delta(x_3) \phi(x_3)\, \mathrm{d}x_3, \end{aligned} \tag{3.51}$$

which when compared to (3.48) gives the following approximation for $p^{(0)}(x_3, t)$

$$p^{(0)}(x_3,t) \approx \frac{\rho_f v_T^2 V_0}{A} g(t) \delta(x_3). \tag{3.52}$$

Similarly, a multipole expansion of $p_{,3}^{(0)}(x_3, t)$ can be carried out resulting in the following approximation

$$p_{,3}^{(0)}(x_3,t) \approx \frac{\rho_f v_T^2 V_0}{A} g(t) \delta'(x_3). \tag{3.53}$$

Under these approximations, the force system in (3.40) has been localized at the origin. It consists of three mutually orthogonal dipoles, or equivalently, a monopole with moment $M_0 = \rho_f v_T^2 V_0 v_c^2 / v_s^2$ and a dipole in the x_3-direction with moment $M = -2(v_s^2/v_c^2) M_0$. This same result was obtained by Ben-Menahem and Kostek (1991), whose analysis assumed from the outset that a point monopole source in a fluid-filled borehole could be replaced by a localized mechanism in an infinite homogeneous medium.

To investigate the consequences of this approximation we compute, as before, the far-field displacements induced by such a localized force system. The far-field displacements can be computed as in (3.30) giving the following displacements

$$\begin{aligned} u_i(\mathbf{x},t) &= \frac{\rho_f v_T^2 V_0 \gamma_i}{4\pi\rho}\left[\frac{(v_c^2/v_s^2 - 2\cos^2\varphi)}{v_c^3}\;\frac{g'(t-|\mathbf{x}|/v_c)}{|\mathbf{x}|}\right. \\ &\quad \left. + \frac{(N^*_{\underline{ii}} - v_c^2/v_s^2 + 2\cos^2\varphi)}{v_s^3}\;\frac{g'(t-|\mathbf{x}|/v_s)}{|\mathbf{x}|}\right]. \end{aligned} \tag{3.54}$$

Using expressions (3.43) and (3.44) we can express the far-field displacements in terms of spherical coordinates as

$$u_R(R,\varphi,\theta,t) = \frac{\rho_f v_T^2 V_0}{4\pi\rho v_c}\;\frac{(1-2v_s^2\cos^2\varphi/v_c^2)}{v_s^2}\;\frac{g'(t-R/v_c)}{R}, \tag{3.55}$$

$$u_\varphi(R,\varphi,\theta,t) = \frac{\rho_f v_T^2 V_0}{2\pi\rho v_s}\;\frac{\sin\varphi\cos\varphi}{v_s^2}\;\frac{g'(t-R/v_s)}{R}. \tag{3.56}$$

Comparing these expressions with the ones derived earlier we notice that the bracketed term in the denominator of (3.45) and (3.46) is missing in both of these expressions. That term in the radiation pattern originates from the motion of the three mutually orthogonal dipole sources, as pointed out by Kurkjian *et al.* (1992). The numerical results in Ben-Menahem and Kostek (1991), for both the point source in a fluid-filled borehole and the above localized mechanism in an infinite solid medium, are in good agreement because their particular choice of parameters was such that $\pi/4 \leq \varphi \leq 3\pi/4$ and $v_T < v_s$.

3.3.3 Borehole in a transversely isotropic medium

We consider now a circular borehole in a transversely isotropic medium with symmetry axis along the x_3-direction, i.e., the borehole axis. The particular medium has the elastic properties of Cotton-Valley shale (Thomsen, 1986). In Table 3.1 we list its properties as well as those of the fluid-filled borehole. The elastic constants are expressed in terms of a local reference system, where the x_3-direction is taken along the symmetry axis of the material.

Using (3.27) we computed the radiation patterns of quasi-P (qP) and quasi-SV (qSV) waves generated by the tube wave in the borehole. These are shown in Figures 3.6 and 3.10, while their corresponding wavefront surfaces are shown in Figures 3.7

and 3.11. For comparison we also show the radiation patterns of $P-$ and SV-waves in an isotropic medium (Figures 3.8 and 3.12, respectively), with the same density as the transversely isotropic medium defined above but with compressional and shear wave speeds given by $v_c^2 = c_{33}/\rho$ and $v_s^2 = c_{44}/\rho$, respectively. The corresponding wavefront surfaces are shown in Figures 3.9 and 3.13. These radiation patterns could have also been obtained by the same technique as employed by Lee and Balch (1982), since the problem is amenable to analytical calculations due to the symmetry.

A case which cannot be analyzed by their technique is, for instance, that of a transversely isotropic medium with symmetry axis perpendicular to the borehole axis. We take the symmetry axis along the x_1-direction. In Figures 3.14 and 3.18 we show the q$P-$ and qSV-wave radiation patterns. The corresponding wavefront surfaces are shown in Figures 3.15 and 3.19. Here, the qSV polarization is such that the particle motion is in planes containing the x_1-axis. For comparison, we also show the P and SV radiation patterns for the isotropic medium defined above (Figures 3.16 and 3.20, respectively). The P-wave radiation patterns shown in Figures 3.12 and 3.16 are the same, but the SV radiation patterns in Figures 3.12 and 3.20 are different because of the different definitions of the SV polarization in both cases. The wavefront surfaces for the P and SV waves in the isotropic medium are shown in Figures 3.17 and 3.21, respectively. Finally, we show the SH radiation pattern in Figure 3.22 with the corresponding wavefront surface shown in Figure 3.23. We also show in Figures 3.24 and 3.25 the radiation pattern and wavefront surface for the isotropic medium, with the definition that the polarization vector is perpendicular to planes containing the x_1-axis.

We next consider a transversely isotropic (TI) medium with a cuspidal qSV wavefront. It consists of a mixture of fine layers involving two components (Miller, 1992) whose properties are listed in Table 3.2. The two components are mixed in a 19:1 ratio. This leads to an equivalent TI medium with properties given in Table 3.3. We first consider the case where the symmetry axis is parallel to the borehole axis (x_3). The properties of the fluid-filled borehole are given in Table 3.1. In Figure 3.26 we show the qP wavefront surface, where we have cut out one quarter of the surface to better reveal its shape. The indicated axes form a right-handed system, with the vertical axis being x_3. The surface is color coded linearly according to the magnitude of the far-field displacement. Figure 3.27 shows the qSV wavefront surface. Again the color represents the magnitude of the far-field displacement, with red and blue being high amplitude but with negative and positive Gaussian curvature of the slowness surface, respectively. In (3.30) we should replace g' by its Hilbert transform for arrivals corresponding to the red zones in Figure 3.27.

We now consider the case where the symmetry axis is perpendicular to the borehole axis. The wavefront surfaces for the qP-, qSV-, and SH-waves are shown in Figures 3.28, 3.29, and 3.30, respectively. The color coding for the first two of these figures is similar to the case above. In Figure 3.30 (SH wavefront) the color red is actually zero. It is interesting to note that in Figure 3.29 (qSV wavefront), the displacement in the x_1x_2-plane is only zero along the axes, whereas for an isotropic medium it would be zero on the entire plane.

3.4 Discussion and Conclusions

In this chapter we have considered the radiation problem from the equivalent source distribution in both fast and slow formations and have provided far-field expressions for the displacements. In slow (anisotropic) formations there can be either one or two "conical" waves arriving earlier than the direct wave from source to receiver. We have illustrated our results by plotting radiation patterns for quasi-P, quasi-SV, and SH-waves in isotropic and transversely isotropic media and the corresponding wavefront surfaces. We illustrate the cases where the borehole axis and the TI axis are parallel, and also when they are perpendicular. These two cases can be completely solved analytically. More general situations may require the numerical solution of sextic equations. It is interesting that the expression for the body-force distribution in the equivalent source is obtained as a product of two matrices, one a function of the material properties of the (anisotropic) medium, including its orientation relative to the borehole, and the other a function of the parameters of the elliptical cross-section of the borehole.

Finally, we considered the problem of computing the pressure field in one borehole induced by a volume injection source in another borehole. The far-field solution is obtained in closed form, and in particular it clearly shows the reciprocal nature of the problem.

ρ	2640 kg/m^3
c_{11}	74.73 GPa
c_{12}	14.75 GPa
c_{13}	25.29 GPa
c_{33}	58.84 GPa
c_{44}	22.05 GPa
c_{66}	29.99 GPa

ρ_f	1000 kg/m^3
v_f	1500 m/s
r_0	0.1 m

Table 3.1: Parameters for the Cotton-Valley shale and the fluid-filled borehole.

	medium 1	medium 2
ρ	2500 kg/m^3	1000 kg/m^3
v_c	2700 m/s	1500 m/s
v_s	1500 m/s	450 m/s

Table 3.2: Parameters for the layered medium.

ρ	2425 kg/m^3
c_{11}	17.02 GPa
c_{12}	6.32 GPa
c_{13}	5.44 GPa
c_{33}	13.45 GPa
c_{44}	2.40 GPa
c_{66}	5.35 GPa

Table 3.3: Equivalent TI parameters for a layered medium composed of two components (see Table 2.2) mixed in a 19:1 ratio.

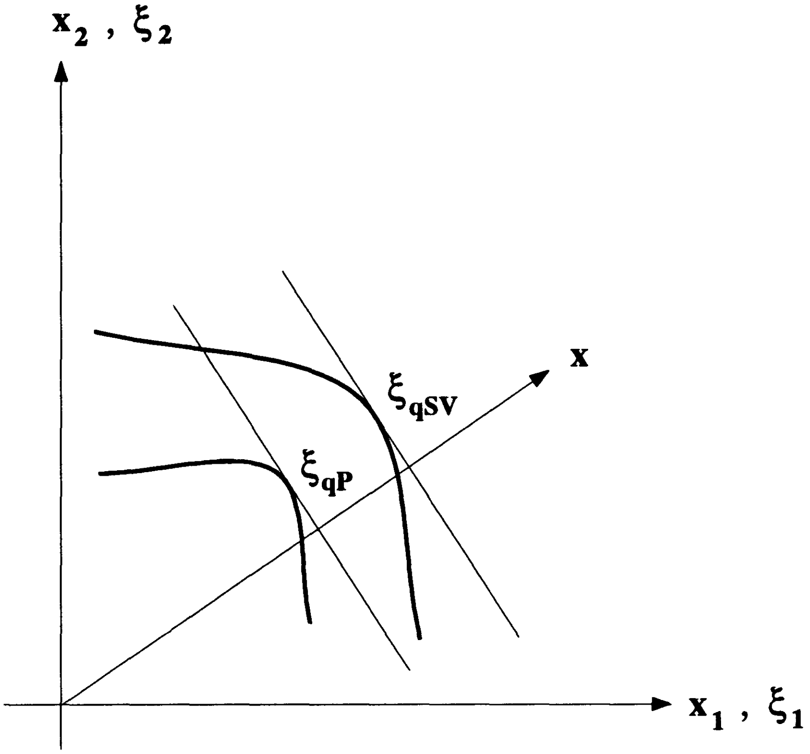

Figure 3.1: qP and qSV slowness surfaces for a TI medium with symmetry axis along the x_3-direction. The indicated points on the two slowness sheets (touched by the planes perpendicular to $\mathbf{x}$) give the most singular contribution at $\mathbf{x}$ in the far field.

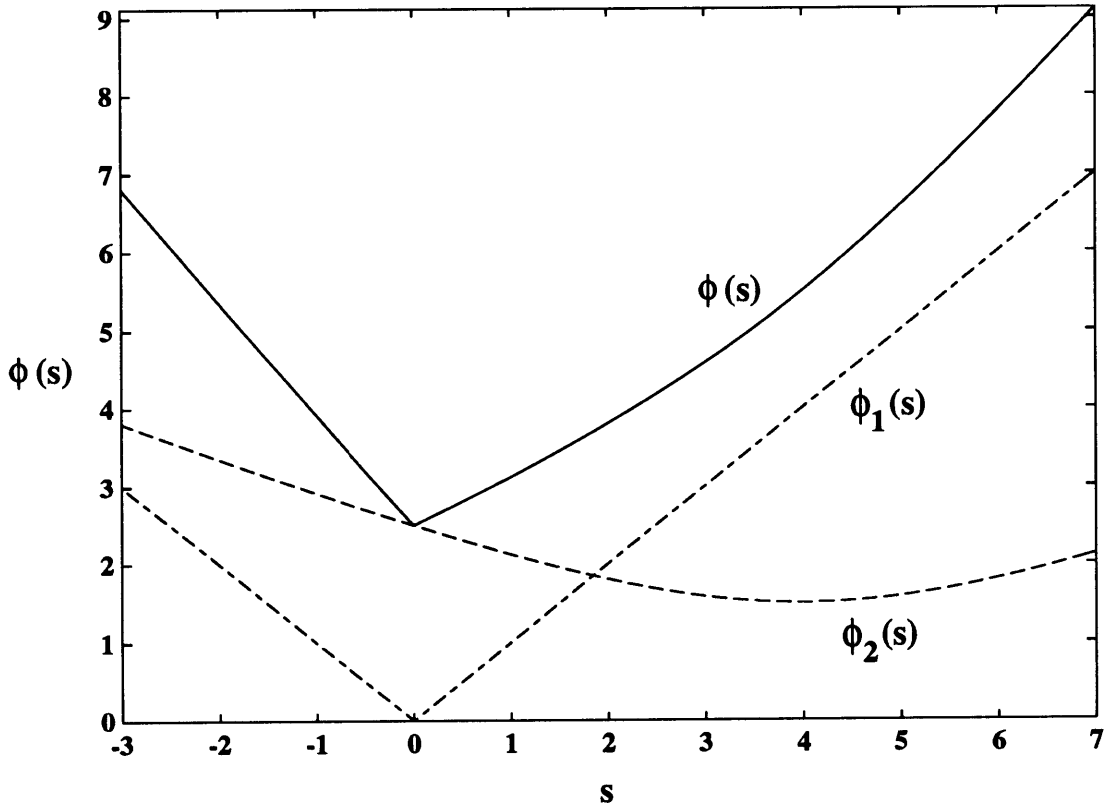

Figure 3.2: Phase function $\phi(s) = \phi_1(s) + \phi_2(s)$ for a fast formation. At $s = 0$, $\phi(s)$ has a finite jump discontinuity in its first derivative.

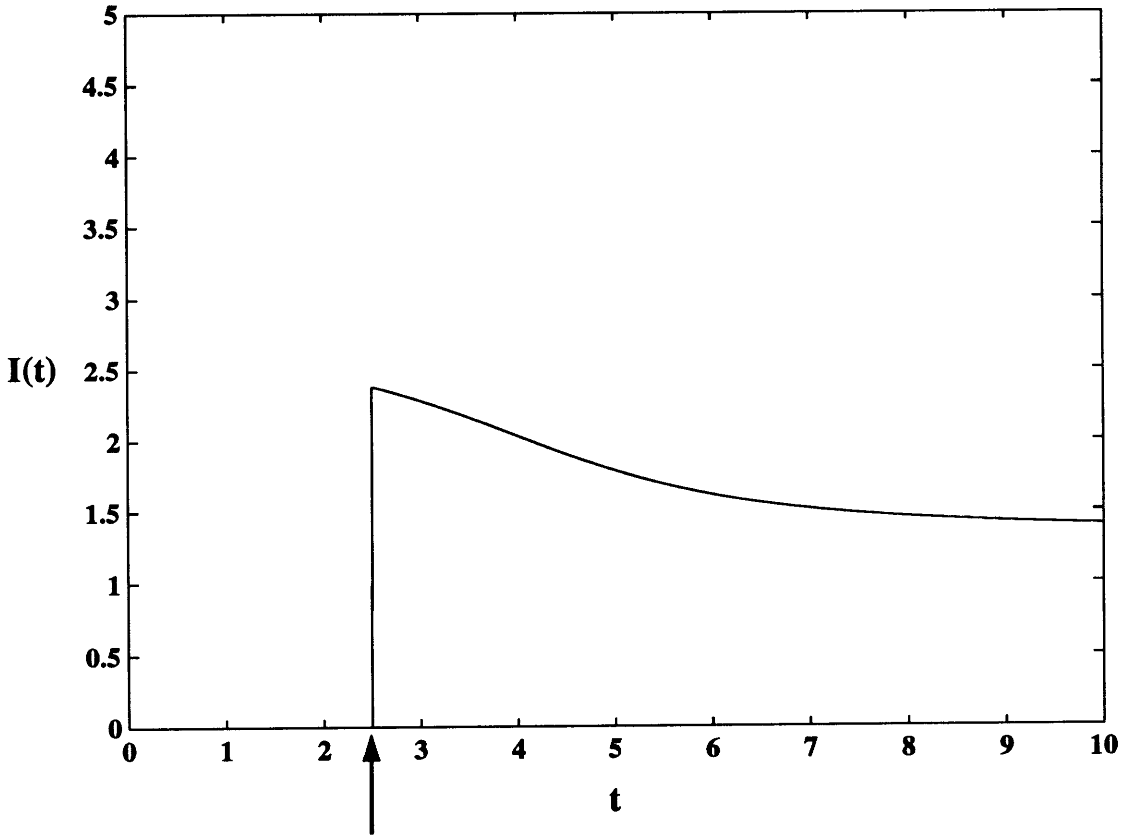

Figure 3.3: Graph of $I(t)$ for a fast formation. The arrow indicates the arrival time of a ray emanating directly from the source.

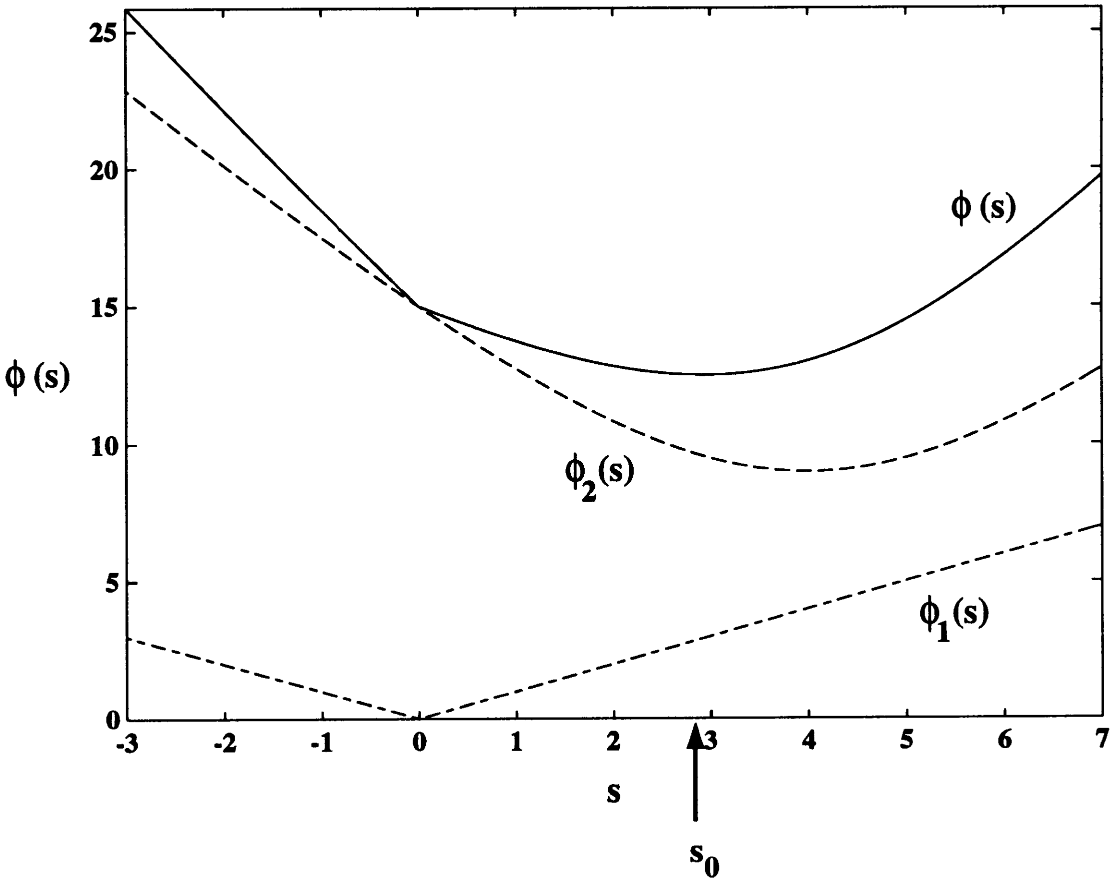

Figure 3.4: Phase function $\phi(s) = \phi_1(s) + \phi_2(s)$ for a slow formation. At $s = 0$, $\phi(s)$ has a finite jump discontinuity in its first derivative. The stationary point (a minimum) is shown at $s = s_0$.

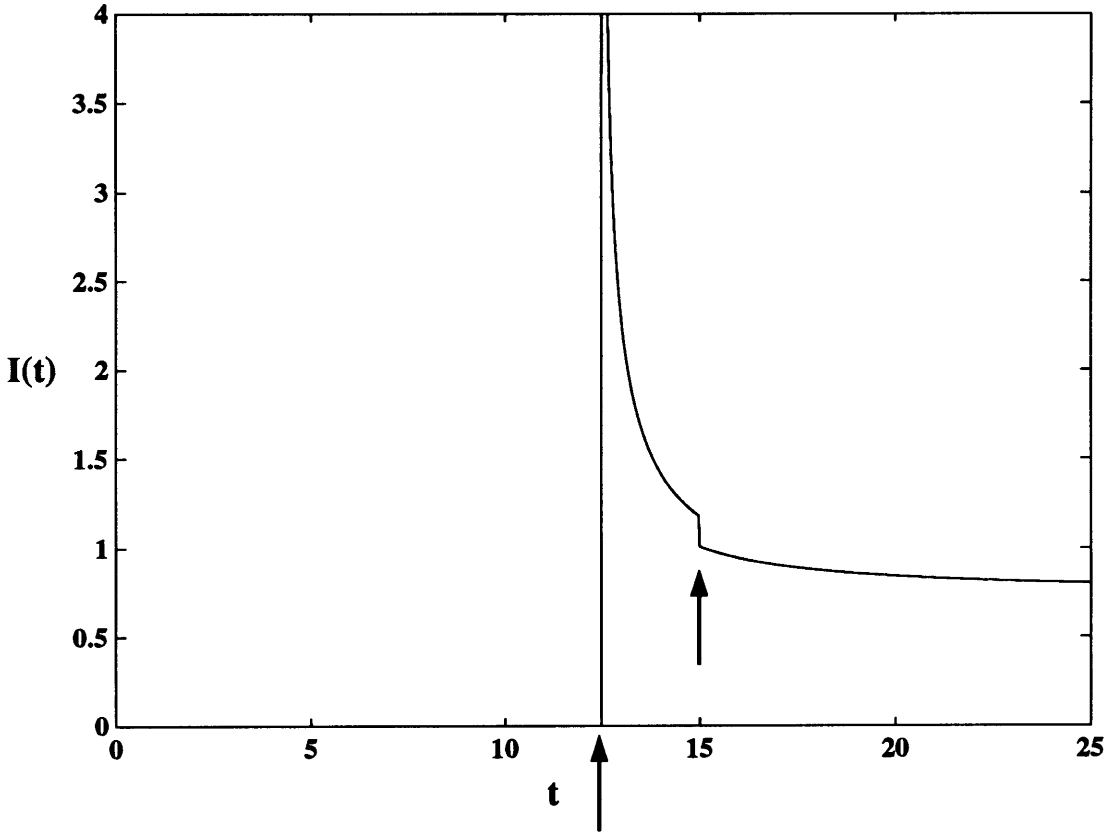

Figure 3.5: Graph of $I(t)$ for a slow formation. The first arrow indicates the arrival time of the "conical" wave. The second arrow indicates the arrival time of a ray emanating directly from the source.

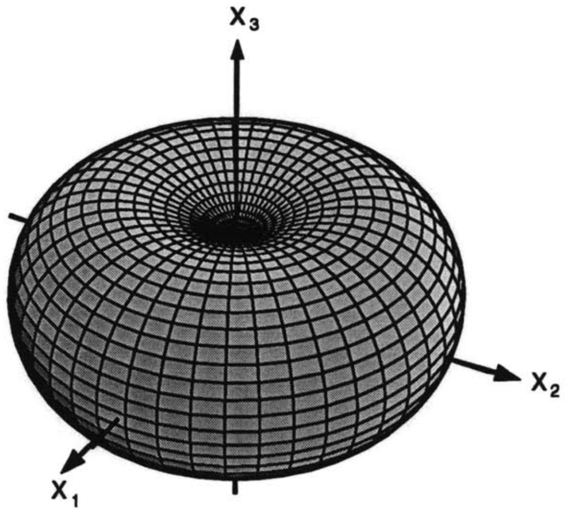

Figure 3.6: Radiation pattern of the qP-wave for symmetry axis along the x_3-direction (parallel to borehole axis).

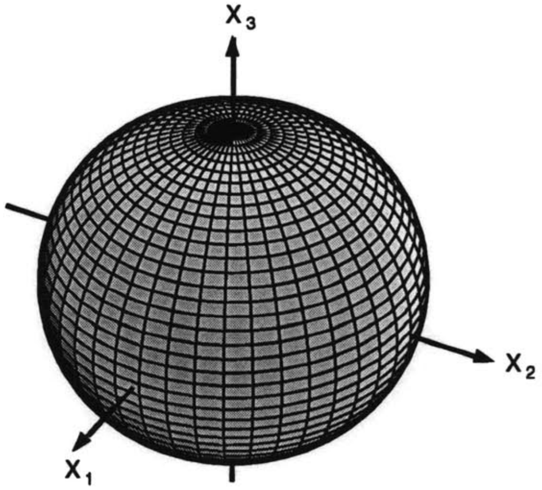

Figure 3.7: Wavefront surface of the qP-wave for symmetry axis along the x_3-direction (parallel to borehole axis).

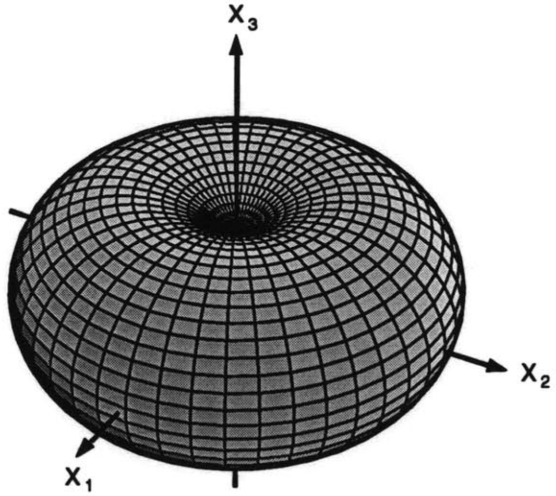

Figure 3.8: Radiation pattern of the P-wave for isotropic medium with $v_c^2 = c_{33}/\rho$ and $v_s^2 = c_{44}/\rho$.

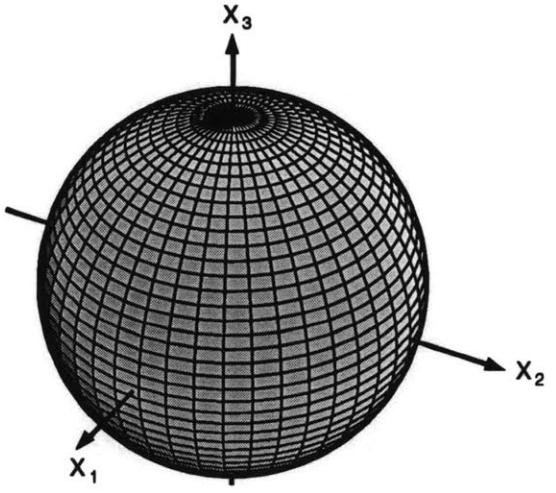

Figure 3.9: Wavefront surface of the P-wave for isotropic medium with $v_c^2 = c_{33}/\rho$ and $v_s^2 = c_{44}/\rho$.

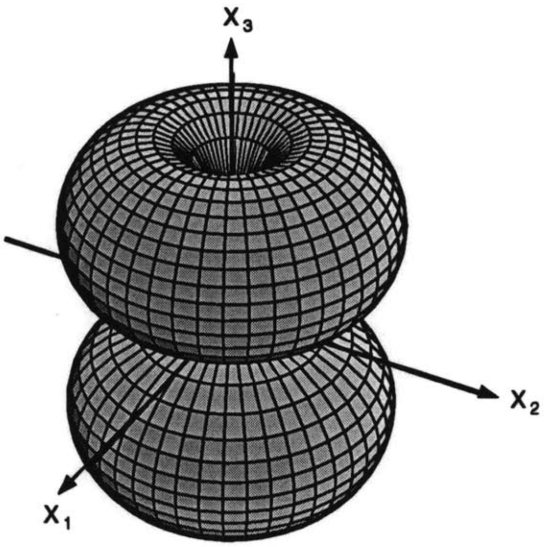

Figure 3.10: Radiation pattern of the qSV-wave for symmetry axis along the x_3-direction (parallel to borehole axis).

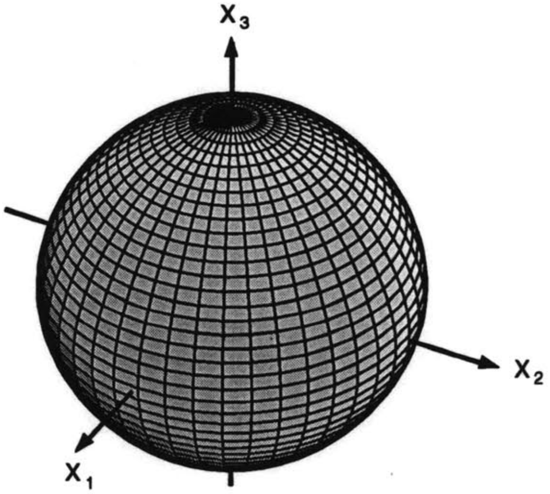

Figure 3.11: Wavefront surface of the qSV-wave for symmetry axis along the x_3-direction (parallel to borehole axis).

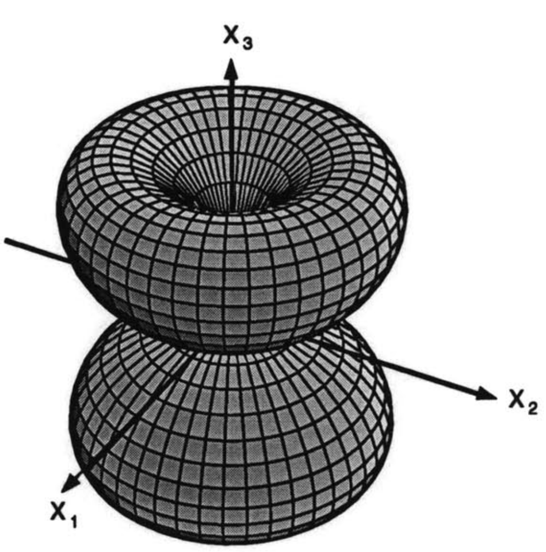

Figure 3.12: Radiation pattern of the *SV*-wave for isotropic medium with $v_c^2 = c_{33}/\rho$ and $v_s^2 = c_{44}/\rho$.

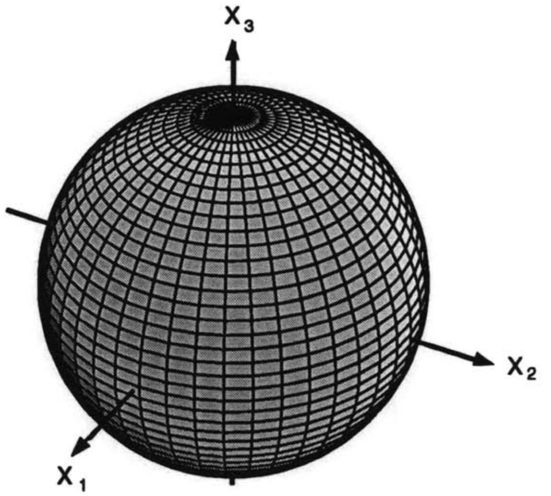

Figure 3.13: Wavefront surface of the *P*-wave for isotropic medium with $v_c^2 = c_{33}/\rho$ and $v_s^2 = c_{44}/\rho$.

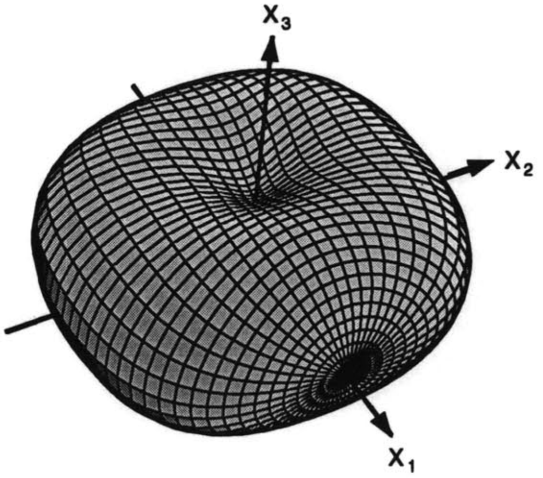

Figure 3.14: Radiation pattern of the qP-wave for symmetry axis along the x_1-direction (perpendicular to borehole axis).

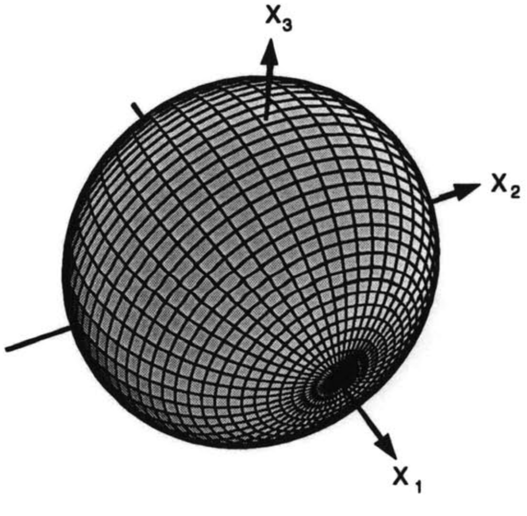

Figure 3.15: Wavefront surface of the qP-wave for symmetry axis along the x_1-direction (perpendicular to borehole axis).

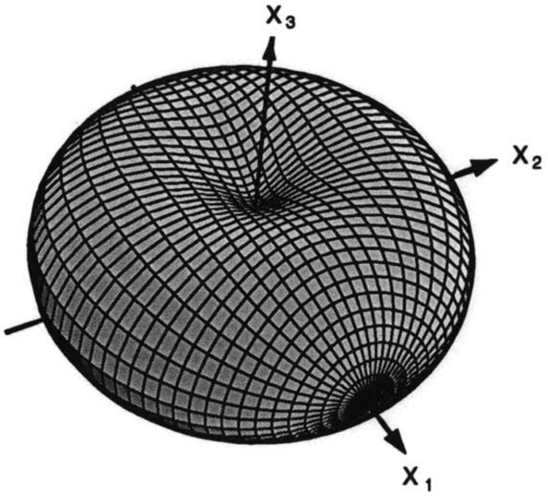

Figure 3.16: Radiation pattern of the P-wave for isotropic medium with $v_c^2 = c_{33}/\rho$ and $v_s^2 = c_{44}/\rho$.

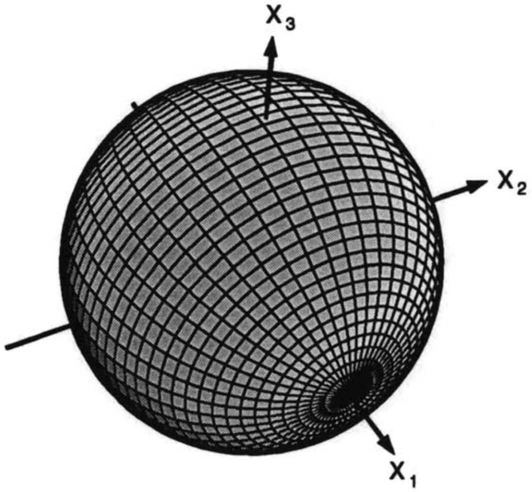

Figure 3.17: Wavefront surface of the P-wave for isotropic medium with $v_c^2 = c_{33}/\rho$ and $v_s^2 = c_{44}/\rho$.

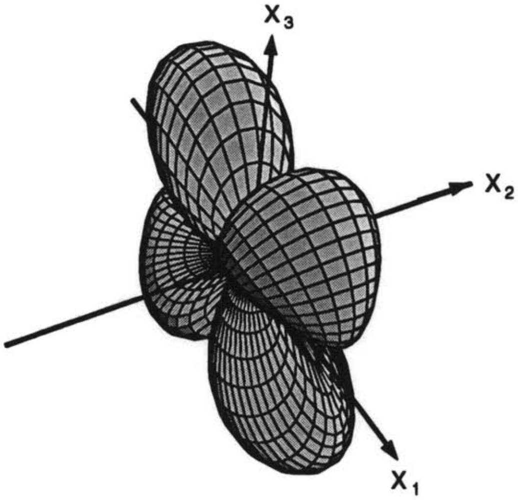

Figure 3.18: Radiation pattern of the qSV-wave for symmetry axis along the x_1-direction (perpendicular to borehole axis).

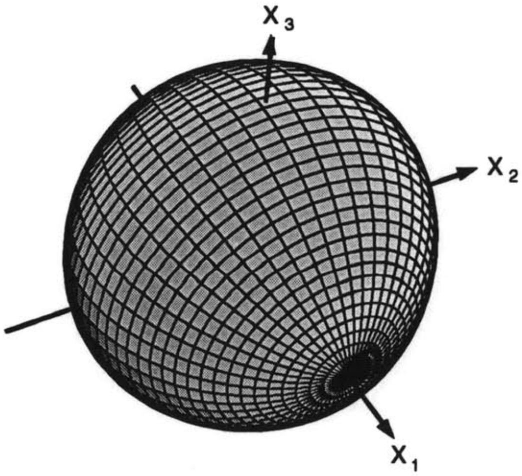

Figure 3.19: Wavefront surface of the qSV-wave for symmetry axis along the x_1-direction (perpendicular to borehole axis).

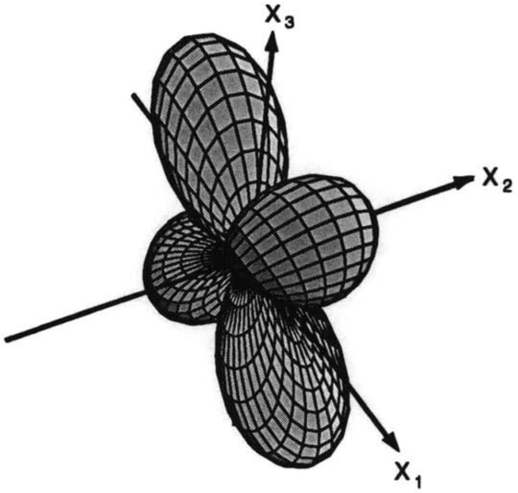

Figure 3.20: Radiation pattern of the SV-wave for isotropic medium with $v_c^2 = c_{33}/\rho$ and $v_s^2 = c_{44}/\rho$.

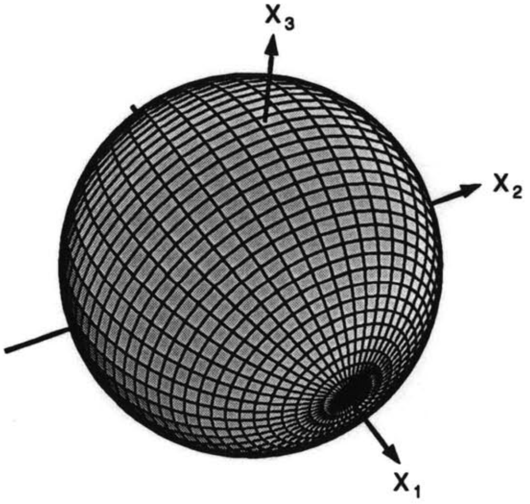

Figure 3.21: Wavefront surface of the SV-wave for isotropic medium with $v_c^2 = c_{33}/\rho$ and $v_s^2 = c_{44}/\rho$.

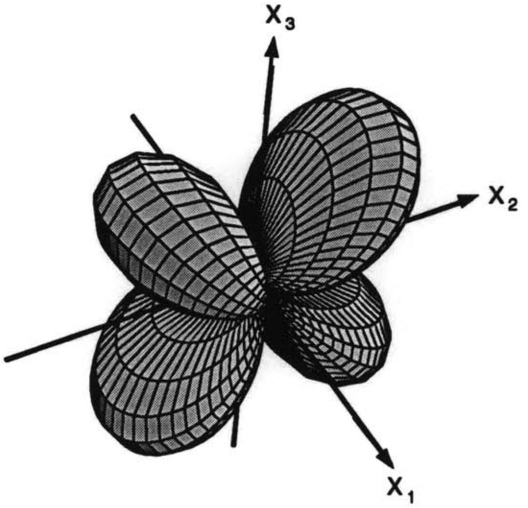

Figure 3.22: Radiation pattern of the SH-wave for symmetry axis along the x_1-direction (perpendicular to borehole axis).

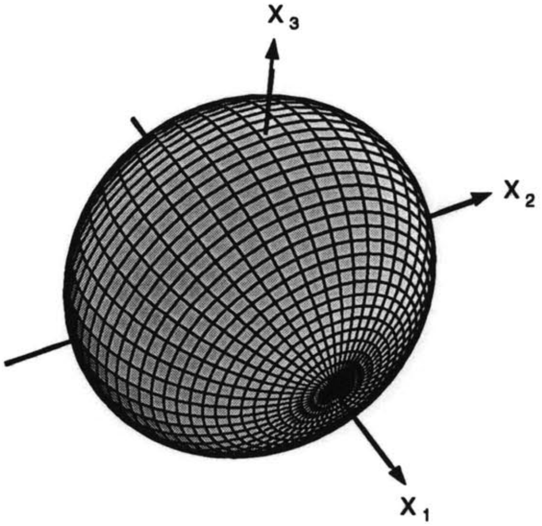

Figure 3.23: Wavefront surface of the SH-wave for symmetry axis along the x_1-direction (perpendicular to borehole axis).

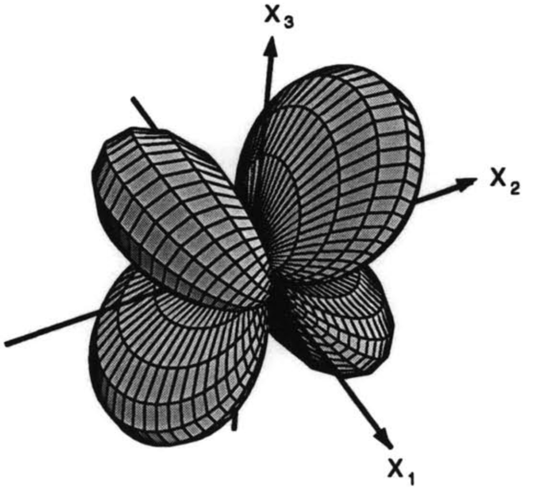

Figure 3.24: Radiation pattern of the SH-wave for isotropic medium with $v_c^2 = c_{33}/\rho$ and $v_s^2 = c_{44}/\rho$.

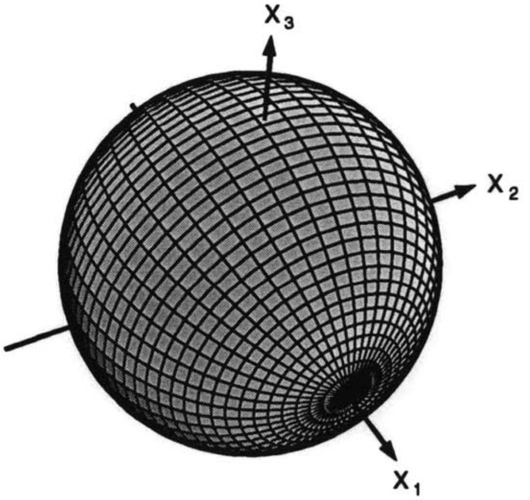

Figure 3.25: Wavefront surface of the SH-wave for isotropic medium with $v_c^2 = c_{33}/\rho$ and $v_s^2 = c_{44}/\rho$.

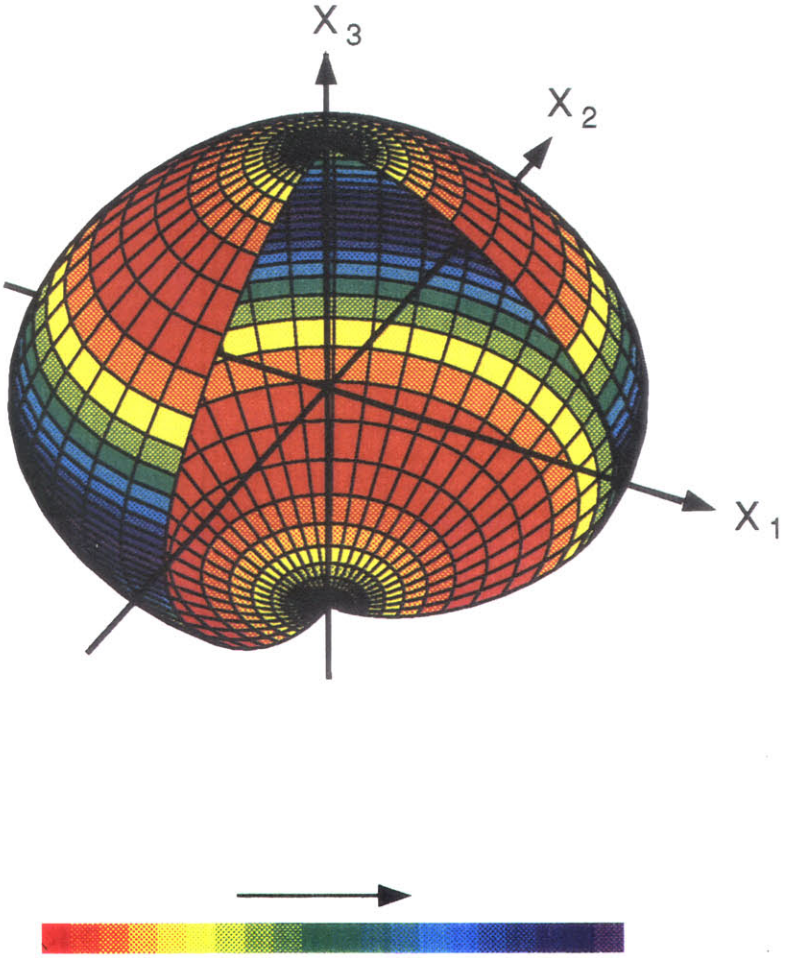

Figure 3.26: Wavefront surface of the qP-wave for symmetry axis along the x_3-direction (parallel to borehole axis). The color represents the magnitude of the displacement for this wave type, where red is low and blue is high.

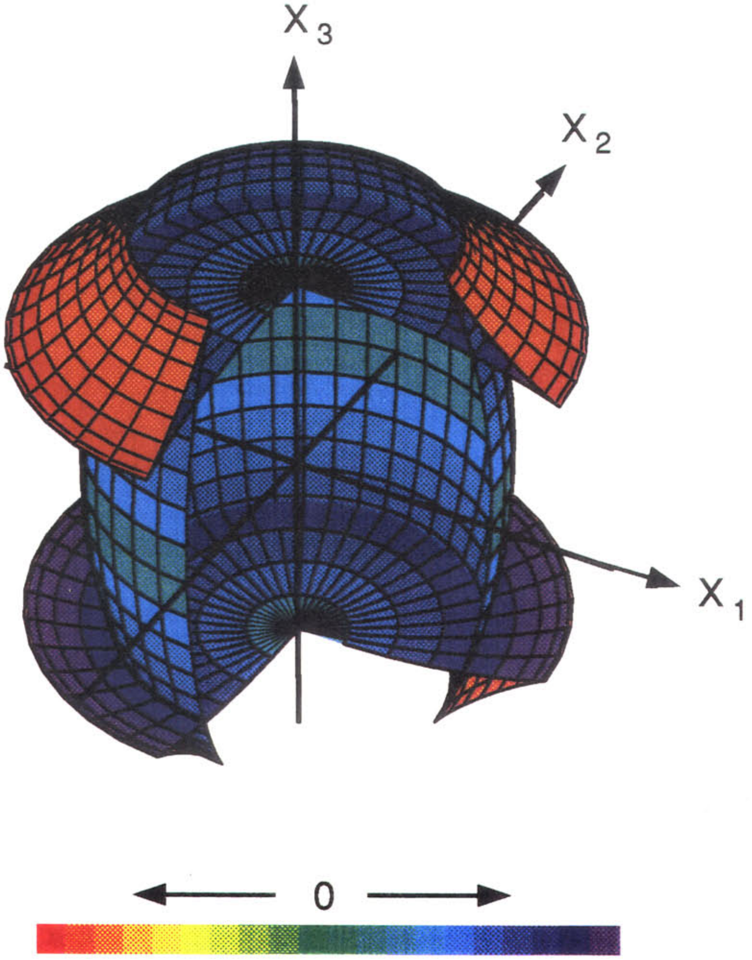

Figure 3.27: Wavefront surface of the qSV-wave for symmetry axis along the x_3-direction (parallel to borehole axis). The color represents the magnitude of the displacement for this wave type, where green is zero, red represents high magnitudes and negative Gaussian curvature of the slowness surface, and blue represents high amplitudes and positive Gaussian curvature.

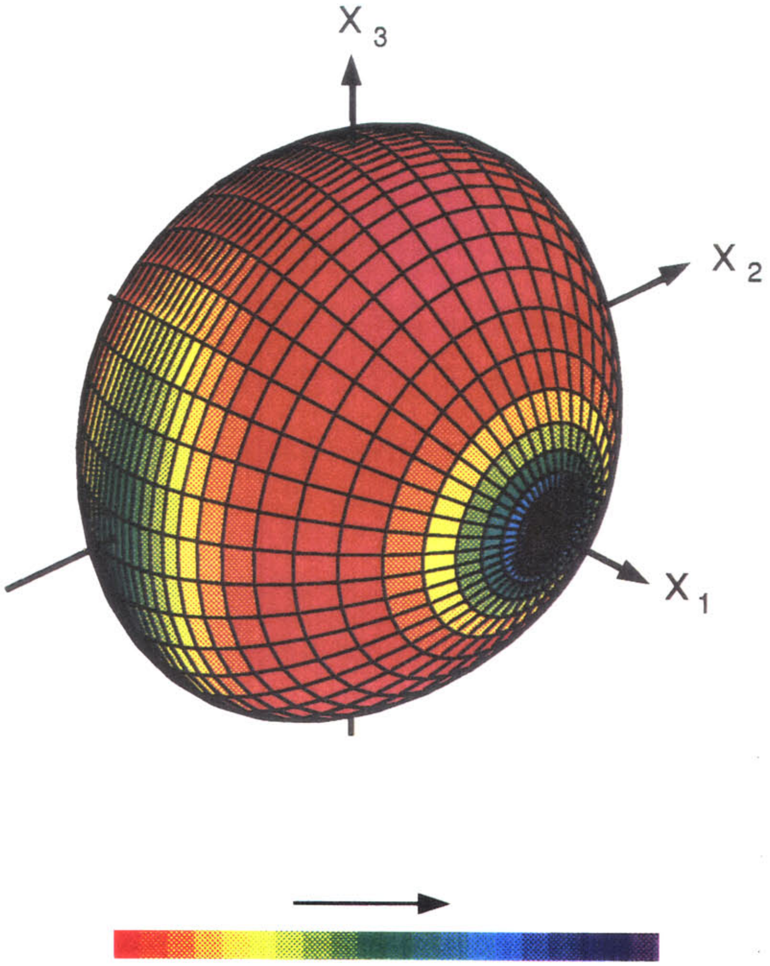

Figure 3.28: Wavefront surface of the qP-wave for symmetry axis along the x_1-direction (perpendicular to borehole axis). The color represents the magnitude of the displacement for this wave type, where red is low and blue is high.

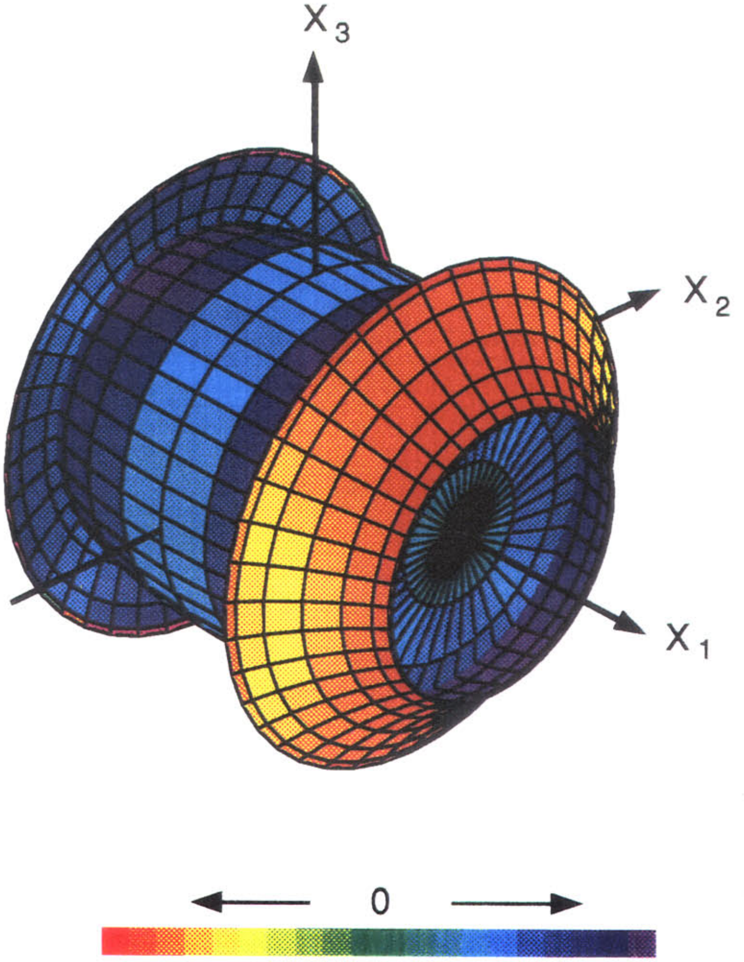

Figure 3.29: Wavefront surface of the qSV-wave for symmetry axis along the x_1-direction (perpendicular to borehole axis). The color represents the magnitude of the displacement for this wave type, where green is zero, red represents high magnitudes and negative Gaussian curvature of the slowness surface, and blue represents high amplitudes and positive Gaussian curvature.

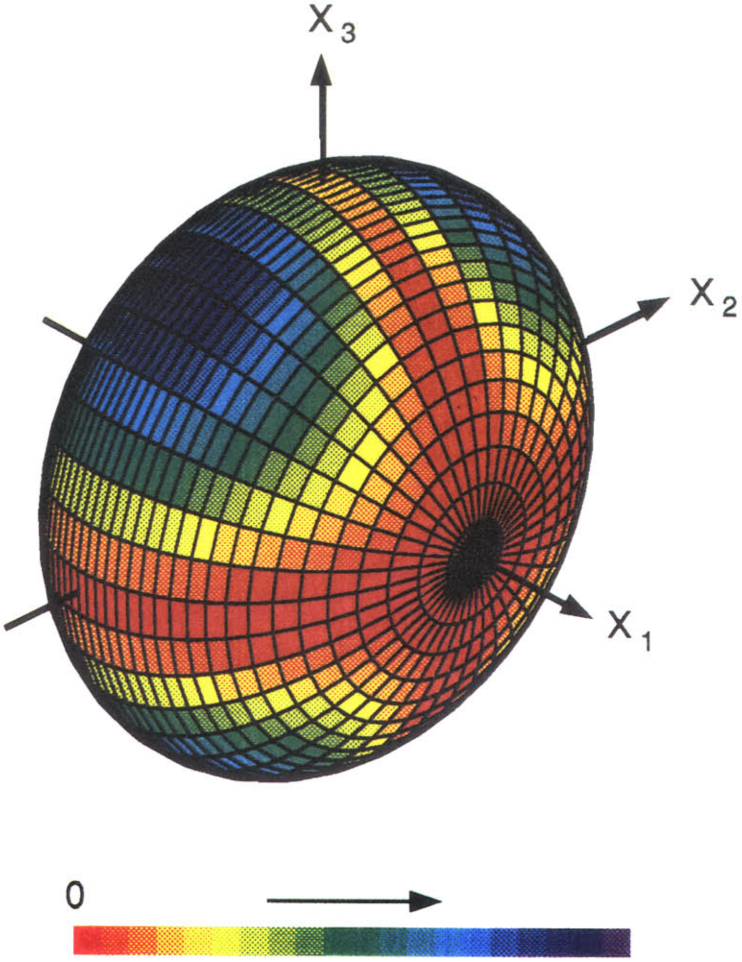

Figure 3.30: Wavefront surface of the SH-wave for symmetry axis along the x_1-direction (perpendicular to borehole axis). The color represents the magnitude of the displacement for this wave type, where red is zero and blue is high.

Chapter 4

Borehole Fractures: Numerical Models

4.1 Introduction

A Stoneley wave is an interfacial wave between two dissimilar elastic materials. In a fluid-filled borehole the Stoneley wave appears as a guided mode which, at low frequencies, is confined primarily to the fluid. When it encounters a *permeable* fracture, it sees this as a sharp impedance contrast and part of the energy is reflected backwards. Reflected tube waves (low-frequency Stoneley waves) have been used by Hornby *et al.* (1989) to locate fractures and estimate their effective aperture by using a simple analytical model. The approach considers horizontal as well as inclined parallel-plate models of fractures. Comparisons with laboratory data show that the simple analytical model tends to underestimate the reflection coefficient of Stoneley waves. The discrepancy probably results from the purely hydraulic model, which assumes the formation is rigid.

To account for the effects of the wall elasticity, Tang (1990) used a modal solution valid at low frequencies to derive expressions for the reflection and transmission coefficients of Stoneley waves from a horizontal parallel-plate model of a fluid-filled fracture. The reflection coefficients resulting from this model are higher than the ones predicted with the rigid formation assumption.

Modeling the effects of horizontal fractures in acoustic waveform logs was attempted by Stephen *et al.* (1985) who used a finite-difference (FD) method to integrate the equations of motion. In their work gradient zones were artificially introduced above and below the fracture because their technique could not account for discontinuities in the elastic properties such as fluid-solid interfaces. They considered a single fracture with an aperture of 8 cm. Stoneley wave reflections were observed, but their amplitudes were mainly controlled by the gradient zones rather than by the fracture itself.

In this chapter we present a mathematical model to account for the presence of horizontal fractures intersecting a fluid-filled borehole. The model is easily implemented with finite differences and allows for the simulation of fractures in general axi-symmetric inhomogeneous media. We concentrate on the effects of fractures on Stoneley waves and compare simulation results with existing analytical models.

4.2 The Fluid-Filled Borehole Model

In this section we restate the relevant equations of elastodynamics governing the propagation of waves in an elastic medium such as the fluid-filled borehole environment. We rewrite Equations (2.12) and (2.16) as

$$\rho \frac{\partial \mathbf{v}}{\partial t} = \nabla \cdot \boldsymbol{\tau}, \tag{4.1}$$

$$\frac{\partial \boldsymbol{\tau}}{\partial t} = \lambda(\nabla \cdot \mathbf{v})\mathbf{I} + \mu(\nabla \mathbf{v} + \mathbf{v}\nabla), \tag{4.2}$$

where $\mathbf{v}$ is the particle velocity. Equations (4.1) and (4.2) form a first-order hyperbolic system, which can be easily discretized by an explicit finite-difference scheme (Virieux, 1986). The main advantage of working with this first-order system rather than the second-order one in terms of displacements is that the stability relation is independent of Poisson's ratio, which allows for complex fluid-solid interfaces to be modeled implicitly just by setting the shear rigidity to zero in the fluid.

The discretized form of Equations (4.1) and (4.2) in cylindrical coordinates, applicable to the case of axial symmetry are presented in Appendix B. At the edges of the computational grid the finite-difference equations must be augmented by boundary conditions (refer to Figure B.1). The left ($r = 0$) edge of the grid is always a symmetry axis. At the right, upper, and lower edges of the grid, absorbing boundary conditions are applied (Kostek, 1991).

4.3 The Dynamic Fracture Model

We consider a fluid-filled axi-symmetric fracture intersecting a borehole. The fracture can be of variable aperture and of finite extent. Figure 4.1 shows a sketch of the borehole and fracture on the (r, z) plane. Considering the dynamics of two small elements connected with the upper and lower parts of the fracture, we obtain the following approximate equilibrium equations

$$\frac{\partial}{\partial t}\left(\frac{\rho^u v_z^u + \rho^l v_z^l}{2}\right) = \frac{\tau_{zz}^u - \tau_{zz}^l}{\Delta z}, \tag{4.3}$$

$$\frac{\partial}{\partial t}\left(\frac{\rho^u v_z^u - \rho^l v_z^l}{2}\right) = \frac{\tau_{zz}^u + \tau_{zz}^l + 2p}{\Delta z}, \tag{4.4}$$

where the superscripts l and u refer to the lower and upper parts of the fracture, respectively; Δz is the height of the two volume elements (the grid spacing in the vertical direction); and p is the pressure in the fluid inside the fracture, taken here as constant across the aperture. Equation (4.3) expresses the vertical motion of the center of mass of the two elements, while Equation (4.4) considers their relative motion.

Regarding the motion of the (ideal) fluid inside the fracture, we derive the following equation for the pressure

$$\frac{\partial^2 p}{\partial t^2} = v_f^2\left(\frac{\partial^2 p}{\partial r^2} + \frac{1}{r}\frac{\partial p}{\partial r} + \frac{1}{h}\frac{dh}{dr}\frac{\partial p}{\partial r}\right) - \rho_f v_f^2 \frac{\partial}{\partial t}\left(\frac{v_z^u - v_z^l}{h}\right), \tag{4.5}$$

where ρ_f and v_f are the density and the acoustic wave velocity of the fluid, respectively, and $h(r)$ is the fracture aperture. The last term on the right-hand side of (4.5) accounts for the pressure changes due to the relative motion of the upper and lower surfaces of the fracture. The remaining terms form a one-dimensional acoustic wave equations in cylindrical coordinates, for a fracture in a rigid formation with a slowly varying aperture.

4.4 Finite-Difference Implementation

The time evolution of the velocity and stress variables is carried out by using the discretized version of Equations (4.1) and (4.2), namely Equations (B.3)-(B.8) of Appendix B, ignoring the presence of the fractures. The stresses are then corrected by using properly discretized versions of Equations (4.3)-(4.5). In Figure 4.2 we show the layout of the grid upon the computational domain, and the location of the various quantities on the grid. The fracture is vertically positioned at $k = k_f$ and extends radially from $j = j_b$ to $j = j_f$. All quantities referring to the fluid inside the fracture are identified by either a superscript or a subscript "f". The actual algorithm is described next.

Velocities are updated first followed by the stresses,

$$\mathbf{v}^{n+1} \leftarrow \mathbf{v}^{n}, \tag{4.6}$$

$$\boldsymbol{\tau}^{n+3/2} \leftarrow \boldsymbol{\tau}^{n+1/2}. \tag{4.7}$$

The radial component of the particle velocity of the fluid in the fracture is updated by using the equation of motion

$$v_{r\ j}^{f\ n+1} = v_{r\ j}^{f\ n} + \frac{\Delta t}{\rho_f \Delta r}\left(p_{j+1/2}^{n+1/2} - p_{j-1/2}^{n+1/2}\right). \tag{4.8}$$

The stresses in the borehole next to the fracture are corrected by subtracting a uniform pressure induced by the squirting of fluid from the fracture,

$$\tau_{rr}^{n+3/2} \leftarrow \tau_{rr}^{n+3/2} - \Delta p/2, \tag{4.9}$$

$$\tau_{\theta\theta}^{n+3/2} \leftarrow \tau_{\theta\theta}^{n+3/2} - \Delta p/2, \tag{4.10}$$

$$\tau_{zz}^{n+3/2} \leftarrow \tau_{zz}^{n+3/2} - \Delta p/2, \tag{4.11}$$

where

$$\Delta p = -\rho_f\ v_f^2\ \Delta t\ \frac{h}{\Delta z}\ \frac{2j_f}{2j_f - 1}\ \frac{v_{r\ j_f}^{f\ n+1}}{\Delta r}. \tag{4.12}$$

This last expression approximates the constitutive relation in the fluid, $\partial p/\partial t = -\rho_f v_f^2 \nabla \cdot \mathbf{v}$.

Introducing the following quantities related to the fracture region

$$v_{z\ j+1/2}^{+\ n} = \frac{\rho_{j+1/2}^u v_{z\ j+1/2}^{u\ n} + \rho_{j+1/2}^l v_{z\ j+1/2}^{l\ n}}{2\bar{\rho}_{j+1/2}}, \tag{4.13}$$

$$v_{z\ j+1/2}^{-\ n} = \frac{\rho_{j+1/2}^u v_{z\ j+1/2}^{u\ n} - \rho_{j+1/2}^l v_{z\ j+1/2}^{l\ n}}{2\bar{\rho}_{j+1/2}}, \tag{4.14}$$

$$\bar{\rho}_{j+1/2} = \frac{\rho_{j+1/2}^u + \rho_{j+1/2}^l}{2}, \tag{4.15}$$

where $j_b \leq j \leq j_f - 1$, we can approximate Equations (4.3) and (4.4) as

$$v_{z\ j+1/2}^{+\ n+1} = v_{z\ j+1/2}^{+\ n} + \frac{\Delta t}{\bar{\rho}_{j+1/2}\Delta z} \left(\tau_{zz\ j+1/2}^{u\ n+1/2} - \tau_{zz\ j+1/2}^{l\ n+1/2}\right), \tag{4.16}$$

$$v_{z\ j+1/2}^{-\ n+1} = v_{z\ j+1/2}^{-\ n} + \frac{\Delta t}{\bar{\rho}_{j+1/2}\Delta z} \left(\tau_{zz\ j1/2}^{u\ n+1/2} + \tau_{zz\ j+1/2}^{l\ n+1/2} + 2p_{j+1/2}^{n+1/2}\right), \tag{4.17}$$

and thus obtain the updated velocities along the upper and lower faces of the fracture,

$$v_{z\ j+1/2}^{u\ n+1} = \frac{\bar{\rho}_{j+1/2}}{\rho_{j+1/2}^u} \left(v_{z\ j+1/2}^{+\ n+1} + v_{z\ j+1/2}^{-\ n+1}\right), \tag{4.18}$$

$$v_{z\ j+1/2}^{l\ n+1} = \frac{\bar{\rho}_{j+1/2}}{\rho_{j+1/2}^l} \left(v_{z\ j+1/2}^{+\ n+1} - v_{z\ j+1/2}^{-\ n+1}\right). \tag{4.19}$$

Using these velocities we recompute the normal stresses in the region around the fracture by means of Equations (B.5)-(B.7). Also, we set $\tau_{rz\ j}^{n+3/2} = 0$ for $j_b \leq j \leq j_f$.

The pressure in the fluid inside the fracture is updated by discretizing Equation (4.5). First, we express the last term on the right hand side of that equation in terms of the axial stresses and fluid pressure by manipulating Equations (4.3) and (4.4) to give

$$\rho_f v_f^2 \frac{\partial}{\partial t}\left(\frac{v_z^u - v_z^l}{h}\right) = \frac{2\rho_f v_f^2}{h\Delta z}\left(\frac{\tau_{zz}^u}{\rho^u} + \frac{\tau_{zz}^l}{\rho^l} + \frac{\rho^u + \rho^l}{\rho^u \rho^l} p\right). \tag{4.20}$$

In the case of constant fracture aperture, Equations (4.5) and (4.20) are approximated by

$$
\begin{aligned}
&p_{j+1/2}^{n+3/2} - 2p_{j+1/2}^{n+1/2} + p_{j+1/2}^{n-1/2} = \\
&\left(\frac{v_f \Delta t}{\Delta r}\right)^2 \left(p_{j+3/2}^{n+1/2} - 2p_{j+1/2}^{n+1/2} + p_{j-1/2}^{n+1/2} + \frac{p_{j+3/2}^{n+1/2} - p_{j-1/2}^{n+1/2}}{(2j+1)}\right) \\
&-\frac{2\rho_f v_f^2}{h\Delta z}\left[\gamma\left(\frac{\tau^{u\ n+1/2}_{zz\ j+1/2}}{\rho^u_{j+1/2}} + \frac{\tau^{l\ n+3/2}_{zz\ j+1/2}}{\rho^l_{j+1/2}} + \frac{\rho^u_{j+1/2} + \rho^l_{j+1/2}}{\rho^u_{j+1/2}\rho^l_{j+1/2}} p_{j+1/2}^{n+3/2}\right)\right. \\
&\left. +(1-\gamma)\left(\frac{\tau^{u\ n-1/2}_{zz\ j+1/2}}{\rho^u_{j+1/2}} + \frac{\tau^{l\ n-1/2}_{zz\ j+1/2}}{\rho^l_{j+1/2}} + \frac{\rho^u_{j+1/2} + \rho^l_{j+1/2}}{\rho^u_{j+1/2}\rho^l_{j+1/2}} p_{j+1/2}^{n-1/2}\right)\right], \qquad (4.21)
\end{aligned}
$$

where γ is a relaxation ("implicitness") parameter. We have used $\gamma = 0.51$ in all simulations presented in this paper. Equation (4.21) cannot be used to update the pressure at $j = j_f - 1/2$. We use a simple one-way approximation of (4.5) for this purpose.

This completes the updating of all the quantities related to the fracture and at the same time corrects the stresses around the fracture such that they can be propagated with the normal finite-difference scheme, which ignores the presence of the fracture.

4.5 Numerical Simulations

In this section we present the results of simulations for various situations of interest involving fractures. The attention is primarily on Stoneley wave interaction with fractures. Effects due to the elasticity of the formation, multiple fractures, and fractures in the presence of washouts are studied.

4.5.1 Borehole in a Homogeneous Formation

To validate the borehole finite-difference model, we simulate the simple situation of a circular borehole in a homogeneous formation (see Figure 4.3). The borehole and formation parameters are listed in Table 4.1. The excitation is from a point monopole source on the axis, with a time variation given by the second derivative of the Blackman-Harris window centered at 10 kHz (Harris, 1978). The offset of the first receiver from the point source is 1 m, and the inter-receiver spacing is 0.2 m. The finite-difference and real axis integration (RAI) method (Tsang and Rader, 1979) waveforms for this model are shown in Figure 4.4, where the compressional, shear, and Stoneley wave arrivals are clearly seen.

The excellent match between the analytical and numerical waveforms validates the borehole propagation portion of the model. The very small differences, most noticeable at the largest offset, are due to plotting interpolation, finite-difference grid dispersion, and to numerical approximations made in the RAI computations. The absence of spurious artificial edge reflections is indicative of the good performance of the absorbing boundary conditions.

4.5.2 Static Fracture Displacement

To illustrate some of the capabilities of the model, we carried out a computation of the static displacements induced by a uniform pressure distribution in the borehole in the presence of a finite-size fracture (refer to Figure 4.5). To model this situation with the explicit finite-difference scheme we apply a constant pressure to the surfaces of the borehole and fracture and evolve the equations in time until they relax to the final static solution. To check the results we also computed the displacements by a direct finite-element (FE) solution of the Lamé equations of static elasticity theory. The upper and outer radial boundaries were placed far enough from the fracture region that the displacements on these boundaries could be specified as those occurring in an infinite medium in the absence of the fracture. The radial and vertical displacements along the upper surface of the fracture are presented in Figure 4.6. The two methods are in good agreement.

4.5.3 Single Horizontal Fracture

Under the assumption of a rigid formation, Hornby *et al.* (1989) derived the following expression for the complex reflection coefficient of a tube wave propagating along a borehole in the presence of an infinite horizontal fracture

$$R(\omega) = -\frac{ihH_1^{(1)}(ka)/aH_0^{(1)}(ka)}{1 + ihH_1^{(1)}(ka)/aH_0^{(1)}(ka)}, \tag{4.22}$$

where $k = \omega/v_f$ is the wave number of the tube wave, a is the borehole radius, and h is the fracture aperture (refer to Figure 4.7). Implicit in Equation (4.22) is the fact that the fracture aperture h must be small with respect to the wavelength of the tube wave. We will rederive this equation in the next chapter.

In order to simulate a rigid formation with the finite-difference scheme, we artificially boost the density of the elastic medium while keeping the compressional and shear velocities the same. This has the advantage of increasing the stiffness of the medium and at the same time preserving the finite-difference stability relation. In Figures 4.8 and 4.9 we show the waveforms for the rigid and elastic cases, respectively. The parameters for the borehole and formation are listed in Table 4.2. The fracture aperture in both cases is $h = 0.5$ cm. The inter-receiver spacing is 0.5 m, and the distance between the point source and the first receiver is 2 m. To simulate the rigid case the density of the formation was increased by a factor of 1000. The point source time pulse is as in the previous case but with a center frequency of 1 kHz. At these frequencies the compressional and shear head waves are not very well excited, therefore their amplitudes are not visible in any of the responses. Only the direct and reflected Stoneley waves are seen. The phase change of the reflected wavelet is evident.

To estimate the magnitude of the reflection coefficient, we time window the direct and reflected Stoneley waves and compute their spectral ratio. In Figure 4.10 we show the magnitude of the Stoneley wave reflection coefficient computed from the finite-difference waveforms as well as from Equation (4.22). Notice the good agreement obtained for the rigid case. As expected, the reflection coefficient in the elastic model is higher than the one from the rigid model. This fact will be further explored in the next chapter.

4.5.4 Double Fractures

When multiple fractures are present, it is possible to distinguish their reflections if they are far apart. However, if they are closely spaced it is not obvious whether they behave additively as a single fracture even when the wavelength is much larger than the distance between the fractures. To study this problem we simulated the presence of two 0.25 cm fractures spaced 7 cm apart (refer to Figure 4.11). The borehole and formation parameters are as in Table 4.2. Figure 4.12 shows the waveforms for a rigid formation, where the source function is the same as in the previous case but with a center frequency of 3.1 kHz. The borehole parameters are given in Table 4.2. The inter-receiver spacing is 0.25 m, and the distance between the point source and the first receiver is 1 m. The magnitudes of the reflection coefficients estimated from the waveforms for the cases of a single fracture with aperture $h = 0.5$ cm and double fractures, each with an aperture of $h = 0.25$ cm, are shown in Figure 4.13. Also shown are the low-frequency approximation given by Equation (4.22) for a single fracture and a similar result for double fractures (Spring and Dudley, 1992). Again, we see good agreement between numerical and analytical results. At low frequencies (below 1 kHz) the two fractures behave as a single one with double the aperture. Above 1 kHz we see an increasing separation between the two sets of curves, with the double fracture showing a lower reflection coefficient. Notice that the separation occurs at wavelengths on the order of 1.5 m, which is much greater than the separation between the fractures.

4.5.5 Fractures in the Presence of a Washout

In real situations the fracture region around the borehole is enlarged by washouts of cave-ins caused by the drilling process. This is bound to change the character of the reflected Stoneley signals. To study this effect we model a fracture which intersects the borehole at a washout of rectangular cross section (refer to Figure 4.14). The formation is assumed to be rigid and the borehole parameters are given in Table 4.2. The material parameters are the same as in the previous example. The source center frequency is 1 kHz, the inter-receiver spacing is 0.5 m, and the first receiver is offset 2 m from the source. The fracture offset is 5.5 m from the source. The parameters of the washout are $b = 6$ cm and $c = 4$ cm. The corresponding waveforms are shown in Figure 4.15. The magnitude of the reflection coefficient estimated from a single waveform is plotted in Figure 4.16, together with the low-frequency approximation given by Equation (4.22). Also shown in this figure is the magnitude of the reflection coefficient given by $R(\omega) \approx i\omega V/2\pi v_f a^2$ for a washout of volume V. At very low frequencies the washout-fracture system behaves as if there was no washout. At frequencies above 650 Hz the system behaves as if there were only a washout, with the fluid contained in its volume controlling the reflection of Stoneley waves.

4.6 Discussion and Conclusions

In this chapter we have developed a model which accounts for all interactions between borehole waves and an intersecting fluid-filled fracture. The model lends itself to efficient numerical implementation, e.g., finite-difference method. Since actual fracture apertures are on the order of few millimeters, it is computationally prohibitive to accommodate for an accurate discretization of the fracture region and at the same time propagate the wavefields to actual ranges of interest. Our model, however, does not suffer from this problem since the smaller the fracture aperture the more accurate the model becomes.

Although we have concentrated on the effects of fractures on Stoneley waves, the model is general enough that it can be used to study the effects of fractures and other inhomogeneities on head waves and borehole modes. Comparisons with analytic solutions for the interaction of a Stoneley wave with a fluid-filled fracture in a rigid formation show that the scheme is very effective in modeling thin fractures. The numerical simulations show that the magnitude of the Stoneley wave reflection coefficient is larger for an elastic formation when compared to that for a rigid one. This result is important since it indicates that an interpretation of the Stoneley wave reflectivity according to (4.22) would lead to an overestimation of the fracture aperture h, and thus of the fracture conductivity. Simulations of double fractures show that the interaction between the two fractures has an appreciable effect on the Stoneley reflectivity even when the distance between the fractures is small compared to the wavelength. Here the effect is contrary to that of the elasticity of the formation, therefore Equation (4.22) underestimates the total fracture aperture. Finally, we simulated the effects of a washout-fracture system and showed that at low enough frequencies the effects of the washout can be neglected, since the reflectivity is totally dominated by the fracture characteristics. At higher frequencies, however, the effects of the washout are significant and would lead to a grossly overestimated fracture aperture, if not properly taken into account.

a	0.1	m
ρ_f	1000	kg/m^3
v_f	1500	m/s
ρ	2500	kg/m^3
v_c	4000	m/s
v_s	2310	m/s

Table 4.1: Parameters for the borehole in a homogeneous formation.

a	0.1	m
ρ_f	1000	kg/m^3
v_f	1500	m/s
ρ	2500	kg/m^3
v_c	5000	m/s
v_s	3000	m/s

Table 4.2: Borehole and formation parameters for the fracture cases.

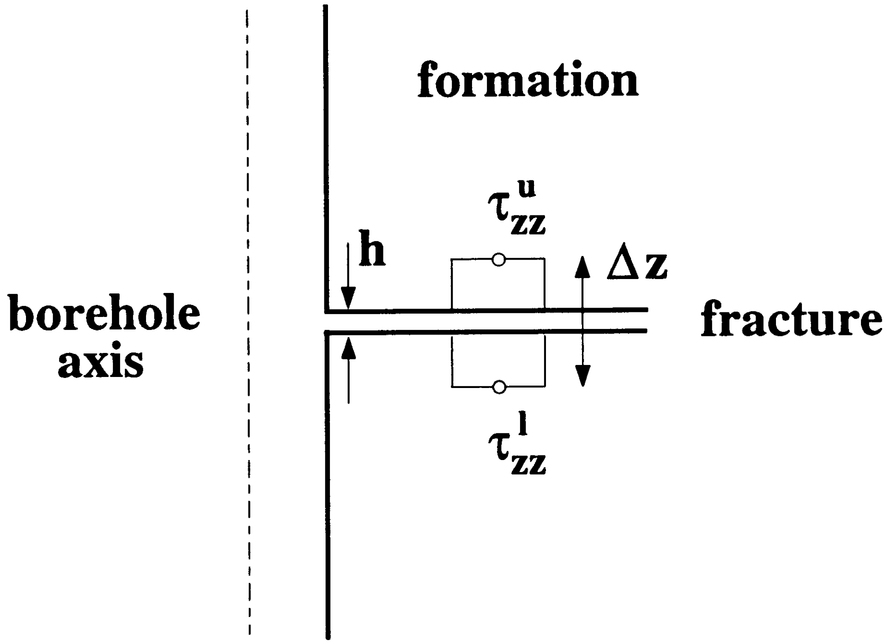

Figure 4.1: Dynamic fluid-filled fracture model.

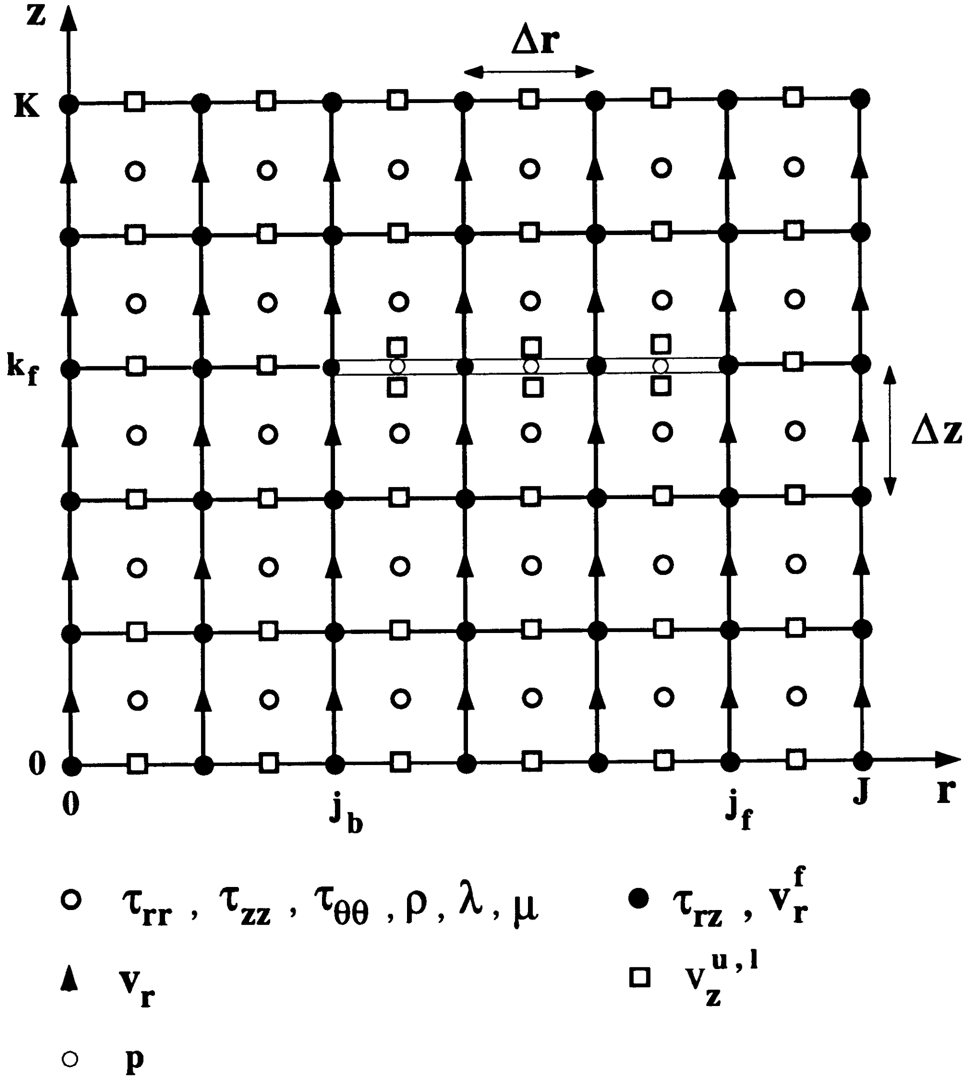

Figure 4.2: Staggered finite-difference grid showing the placement of field variables and elastic parameters. The horizontal fluid-filled fracture is shown at $z = k_f \Delta z$.

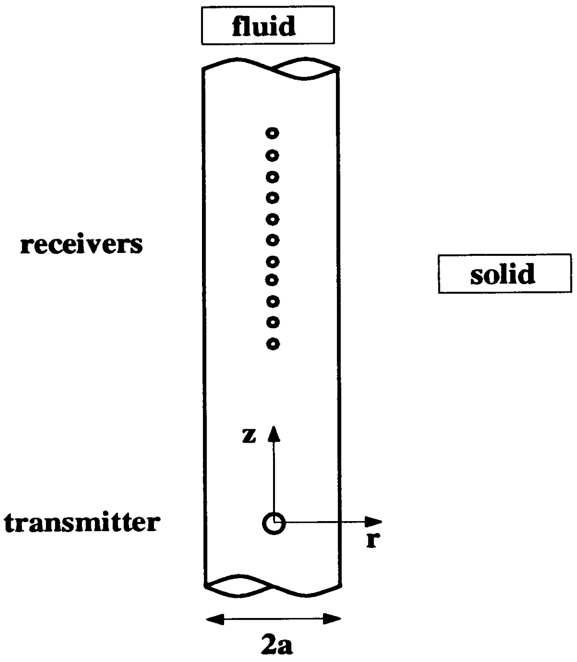

Figure 4.3: Fluid-filled borehole in a homogeneous formation.

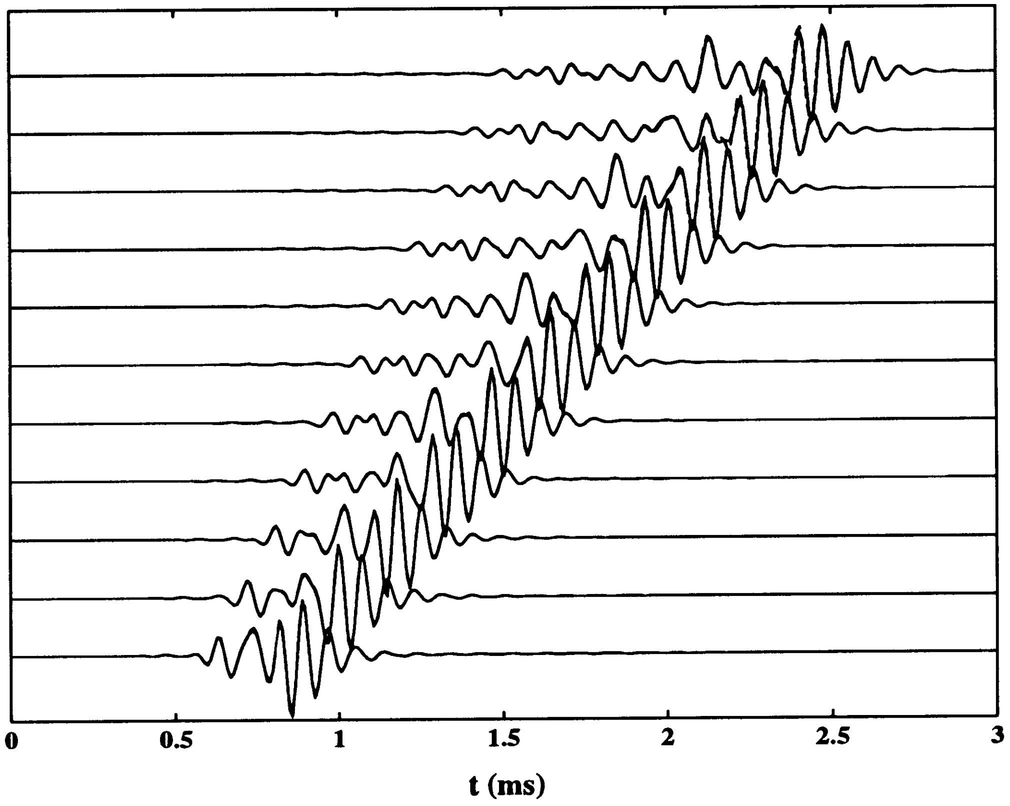

Figure 4.4: Finite-difference (solid) and RAI (dashed) waveforms for the homogeneous formation.

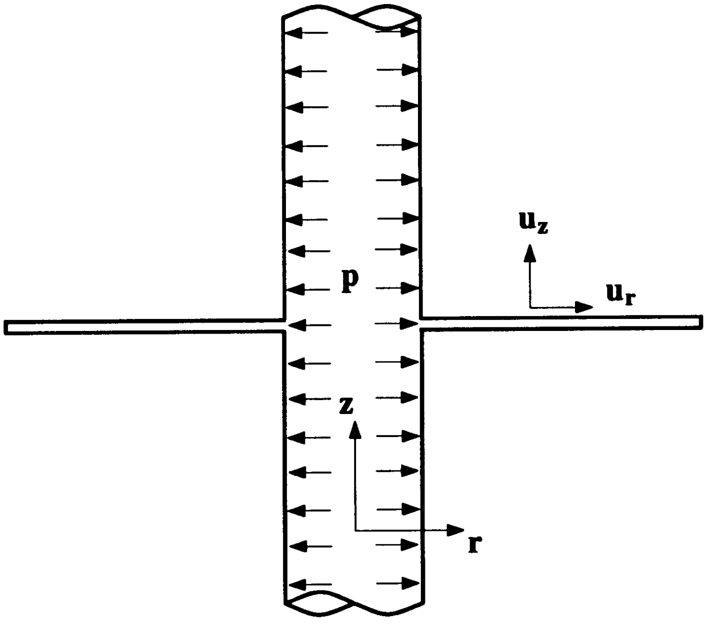

Figure 4.5: Opening of a finite sized fracture due to a static pressure in the borehole.

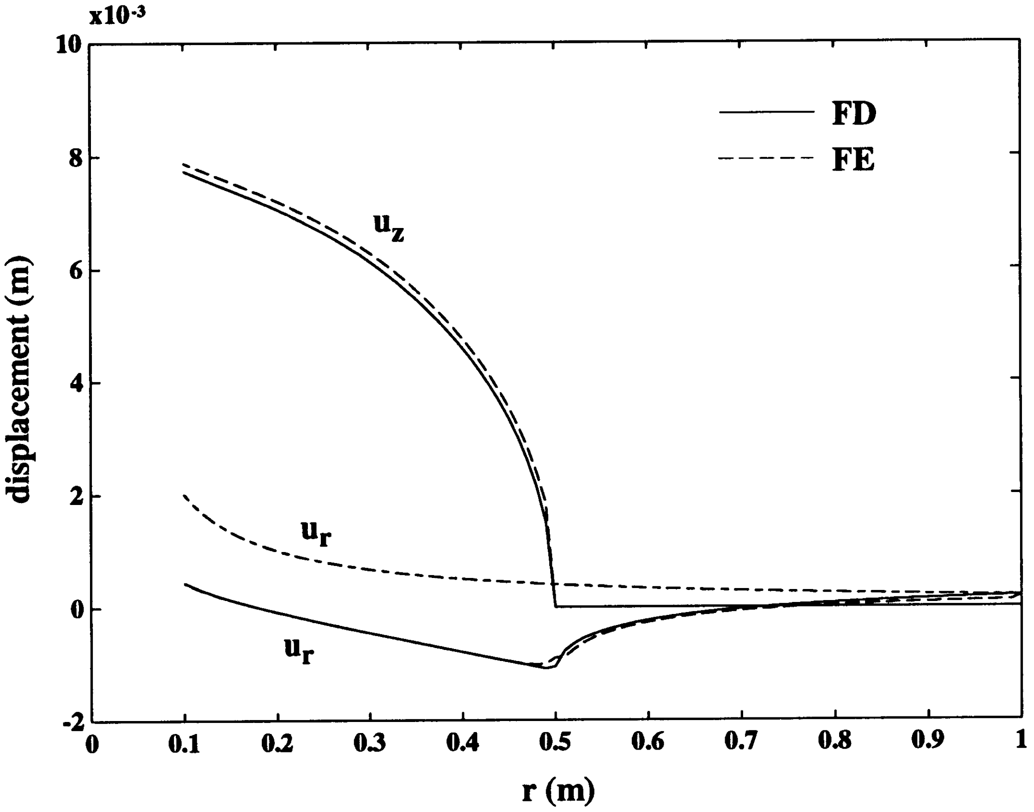

Figure 4.6: Static fracture displacements. The dot-dashed curve corresponds to the radial displacement given by $u_r(r) = pa^2/2\mu r$, due to a uniform pressure on the borehole wall in the absence of the fracture.

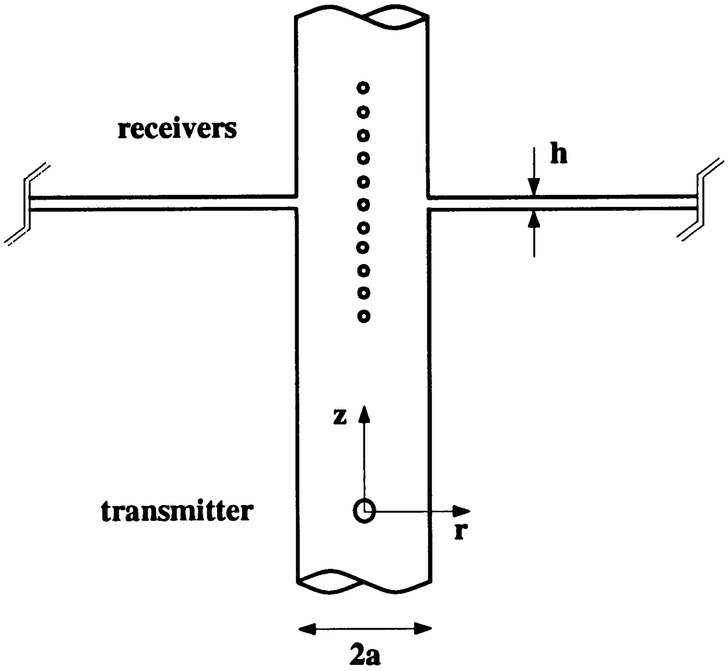

Figure 4.7: Horizontal fluid-filled fracture intersecting a borehole ($a = 10$ cm, $h = 0.5$ cm).

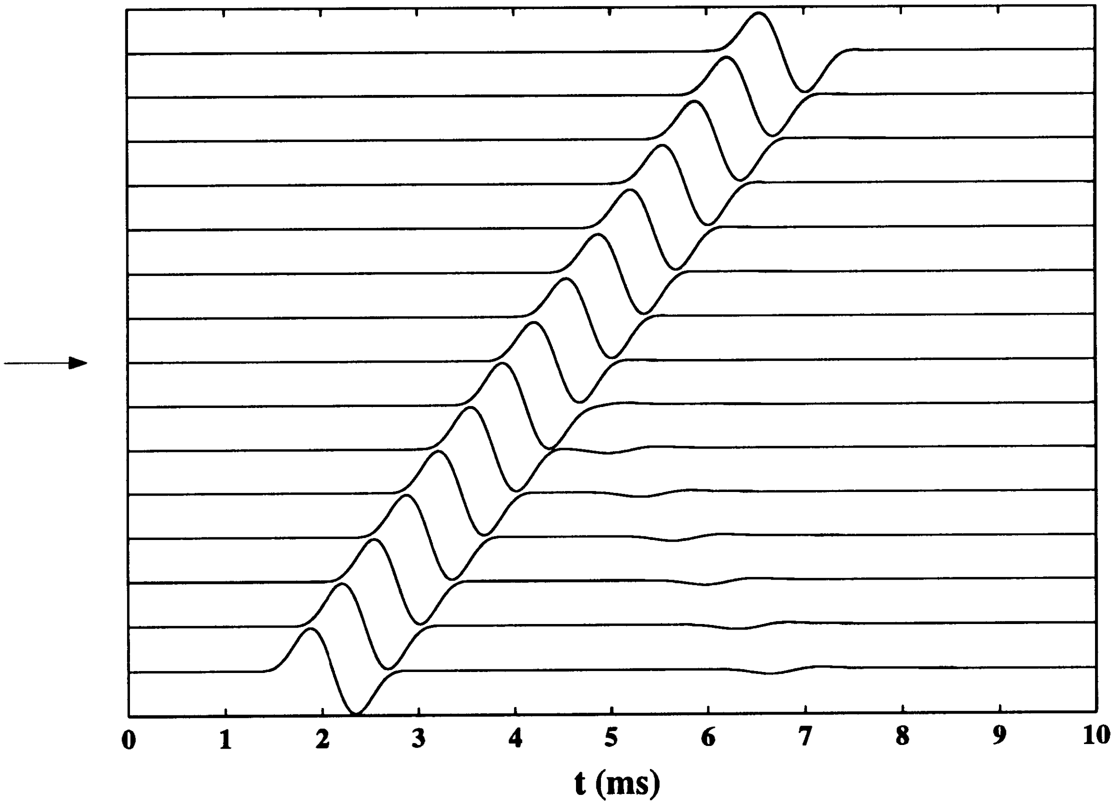

Figure 4.8: Borehole finite-difference waveforms for a rigid formation. The arrow indicates the location of the fluid-filled fracture ($h = 0.5$ cm).

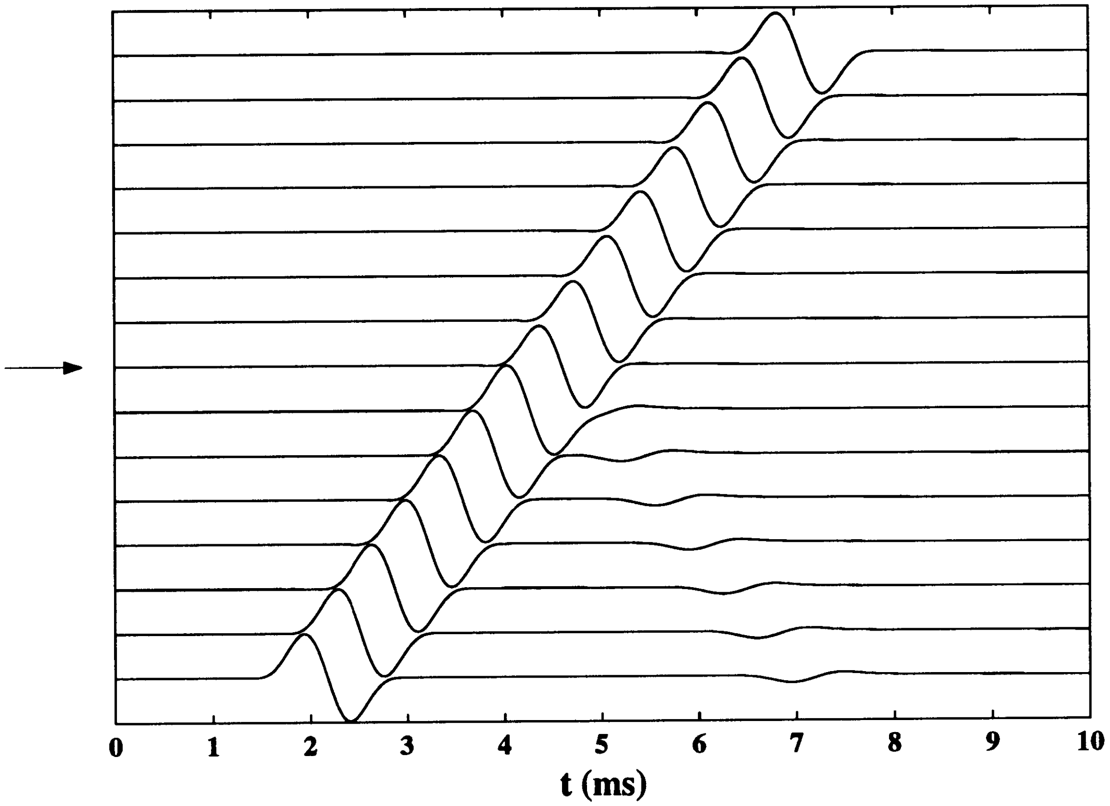

Figure 4.9: Borehole finite-difference waveforms for an elastic formation. The arrow indicates the location of the fluid-filled fracture ($h = 0.5$ cm).

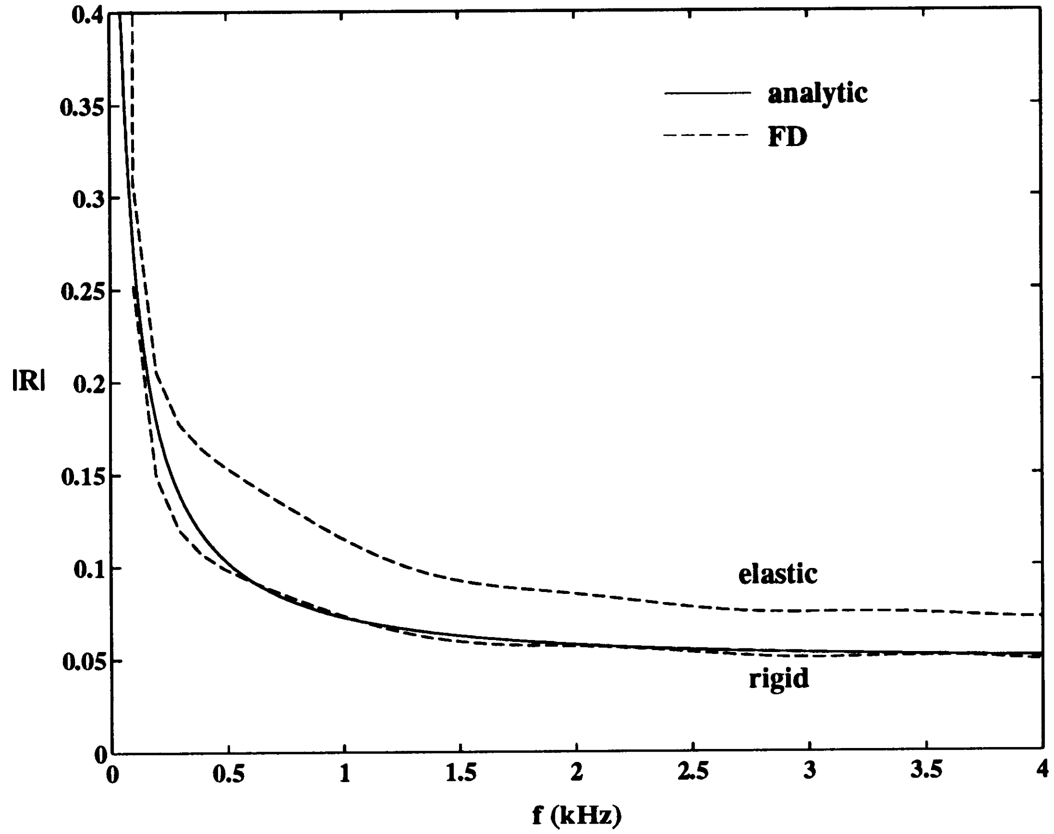

Figure 4.10: Magnitude of the Stoneley wave reflection coefficient for a 0.5 cm aperture fluid-filled fracture.

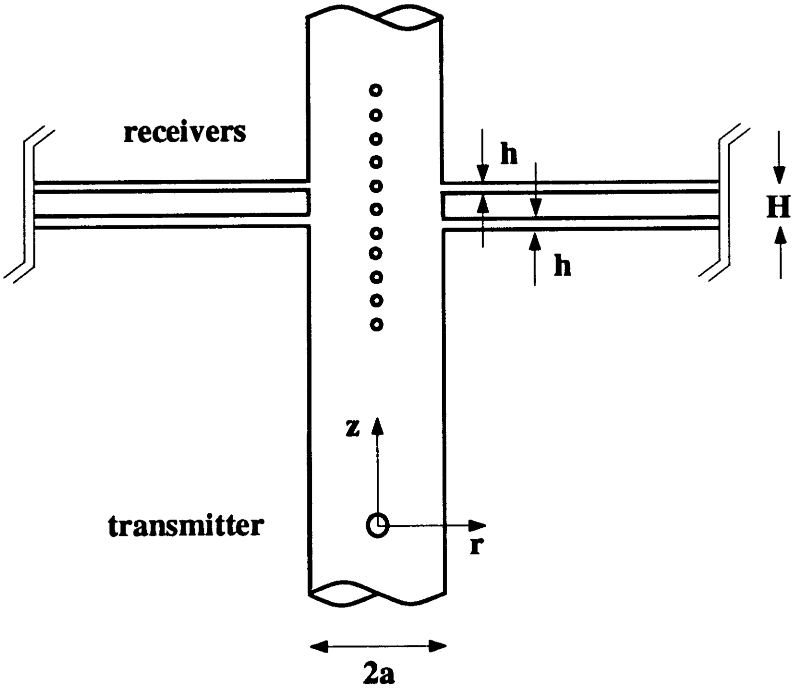

Figure 4.11: Horizontal fluid-filled fractures intersecting a borehole (a = 10 cm, h = 0.25 cm, H = 7 cm).

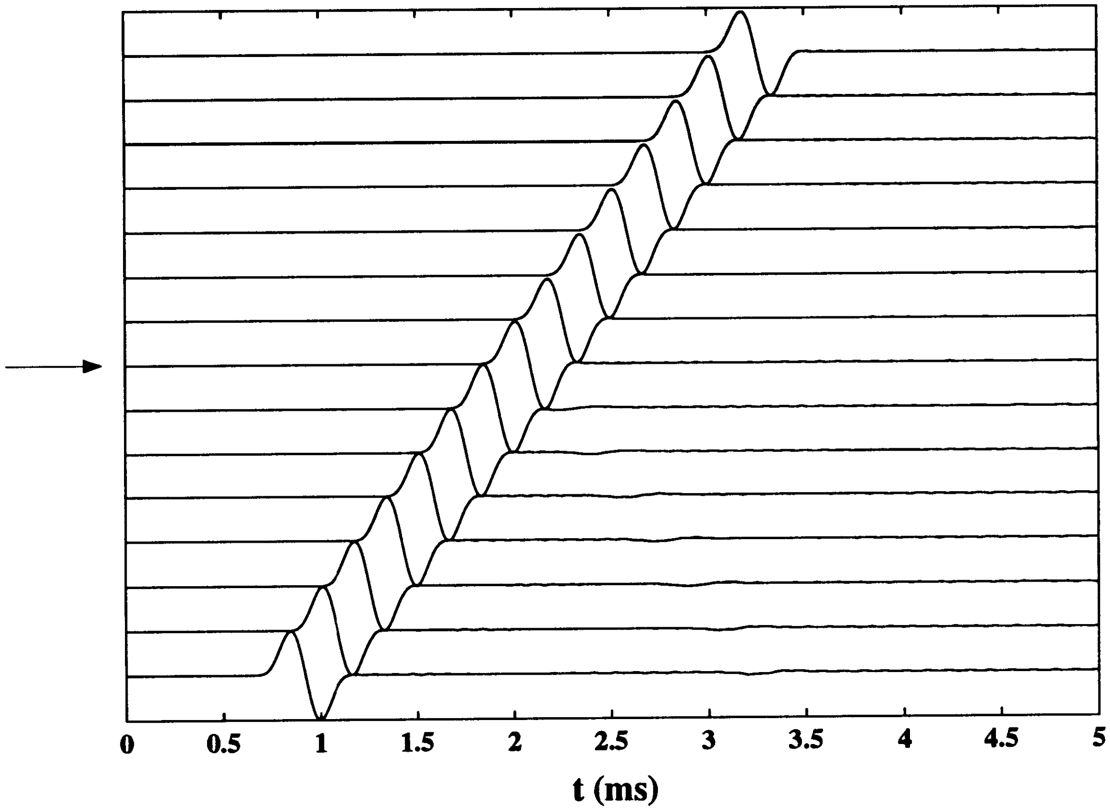

Figure 4.12: Borehole finite-difference waveforms for a rigid formation. The arrow indicates the location of the midpoint between the two fluid-filled fractures (h = 0.25 cm).

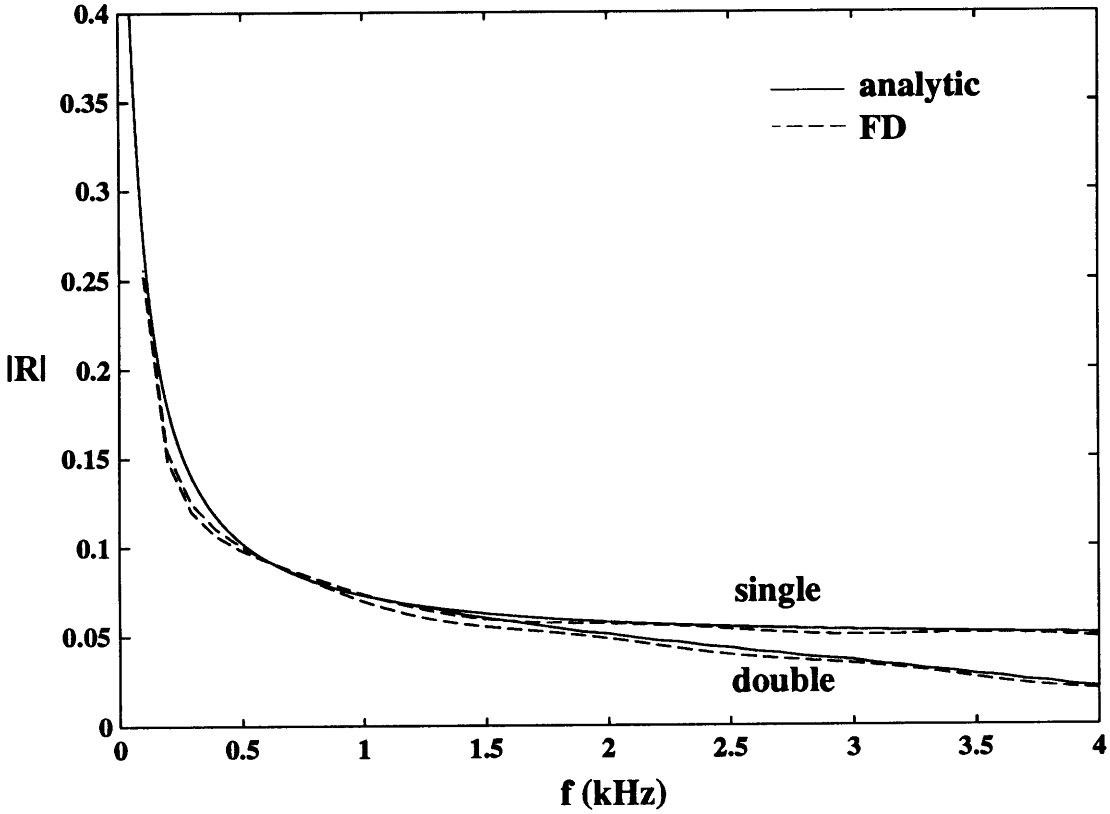

Figure 4.13: Magnitude of the Stoneley wave reflection coefficient for two 0.25 cm aperture fluid-filled fractures 7 cm apart.

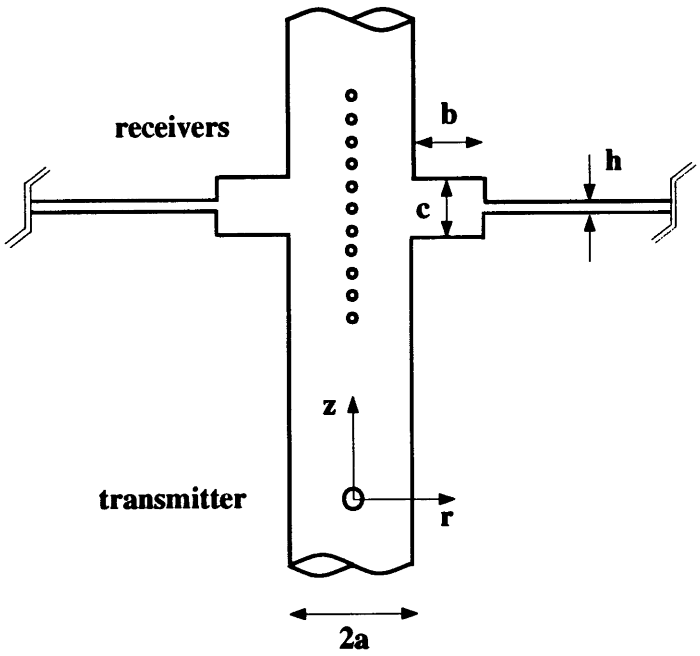

Figure 4.14: Horizontal fluid-filled fracture intersecting a borehole at a washout ($a = 10$ cm, $b = 6$ cm, $c = 4$ cm, $h = 0.5$ cm).

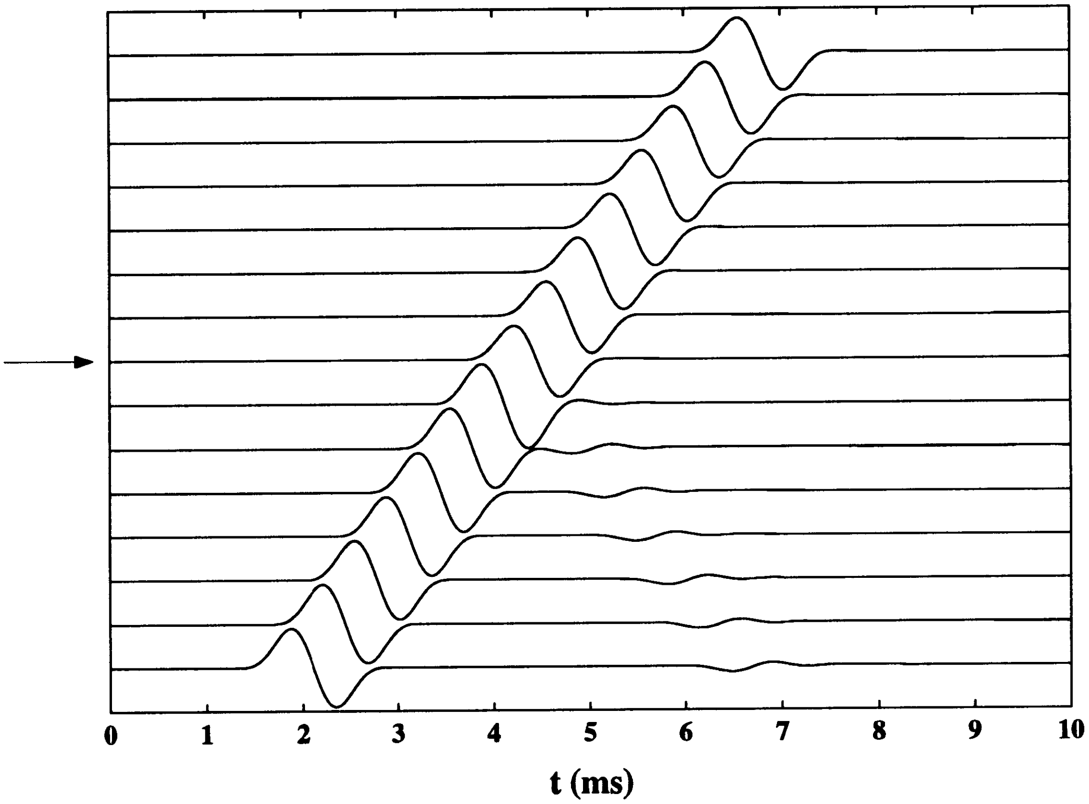

Figure 4.15: Borehole finite-difference waveforms for a rigid formation. The arrow indicates the location of the washout and fluid-filled fracture ($h = 0.5$ cm).

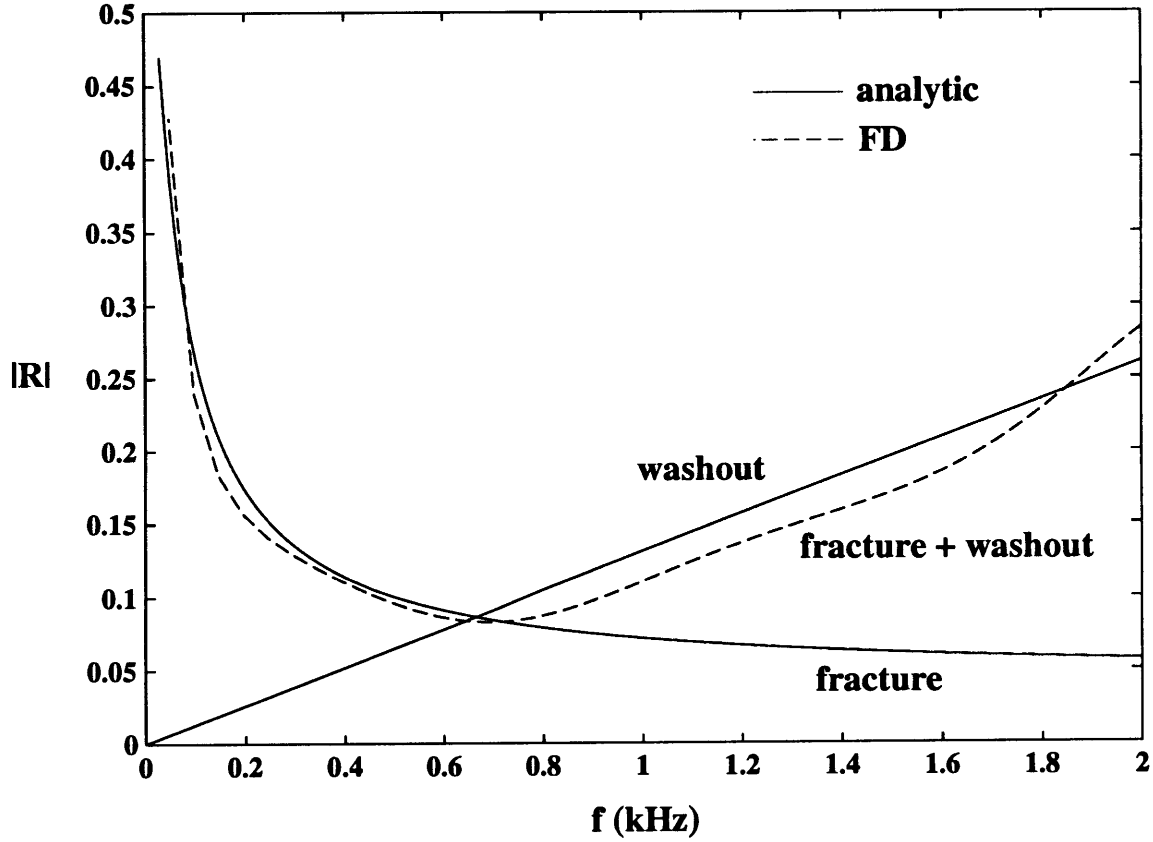

Figure 4.16: Magnitude of the Stoneley wave reflection coefficient for the combined washout and fluid-filled fracture. The straight line starting at the origin is the magnitude of the reflection coefficient of the washout itself, $|R(f)| \approx fV/v_f a^2$ (low-frequency approximation), where V is the volume of the washout.

Chapter 5

Borehole Fractures: Analytical Models

5.1 Introduction

In the previous chapter we presented numerical simulation results that showed a variety of important effects on the propagation of Stoneley waves and their interactions with fluid-filled fractures intersecting a borehole. In particular we focussed on the reflection phenomenon which arises when a Stoneley wave encounters a permeable fracture. Similarly, borehole enlargements (*e.g.*, washouts) give reflections that are qualitatively indistinguishable from fracture reflections. In combination with open fractures, borehole enlargements can severely alter the Stoneley wave reflection coefficient. While our numerical fracture model can treat the realistic geometries of fractures and washouts, it is of limited use as a practical model for obtaining fracture parameters from data such as the reflectivity of Stoneley waves, since it is computationally intensive. We have also shown that the formation elasticity significantly changes the reflection coefficient of Stoneley waves from a fluid-filled fracture, thus rendering Equation (4.22) inapplicable for most cases of interest.

Multiple fractures also complicate the interpretation of Stoneley wave reflections. Figure 5.1 shows data collected from a well drilled in crystalline rocks. On the left part of that figure two images corresponding to the reflected amplitude from a borehole televiewer (BHTV) and the formation microscanner are shown. It is clear from these images that the zone between 610-615 feet is highly fractured, whereas at a depth of approximately 607 feet, two individual horizontal fractures are present. The question thus arises of how Stoneley waves would interact with such features, and furthermore what kind of information can be extracted from the reflectivity.

In the next sections we develop analytical models which incorporate knowledge such as the volume of the washout and the formation elastic properties to predict the reflectivity of Stoneley waves from fractures. We also establish the equivalence between fractured and permeable zones insofar as they affect Stoneley wave propagation. It is thus suggested, following Tang and Cheng (1993), that the fundamental parameter of interest in highly fractured zones is the effective permeability rather than the total fracture aperture.

5.2 Borehole Washouts and Fractures

We assume that the fracture is perpendicular to the borehole axis and that the region where the fracture intersects the borehole is enlarged, such as shown in Figure 4.14. The shape of the enlarged region, heretofore referred generically as a "washout", is arbitrary and with a characteristic diameter of L. We assume that L and the borehole radius (a) are both smaller than the characteristic wavelength. Let V be the volume of the washout and d the radius of the region where the fracture intersects the washout. We will further assume that the formation is rigid and that the frequency is low enough such that the tube wave is the dominant mode. Designating the borehole region above the fracture by (I) and that below by (II), with the fracture being located at $z = 0$, we can express the tube wave pressure in these regions as

$$p^{I} = e^{ikz} + R(\omega)e^{-ikz}, \tag{5.1}$$

$$p^{II} = T(\omega)e^{ikz}, \tag{5.2}$$

where $k = \omega/v_f$ and $R(\omega)$ and $T(\omega)$ are the reflection and transmisssion coefficients of the fracture-washout system. In the long wavelength approximation the pressure in the washout region is uniform and equals that at $z = 0$. Therefore the following continuity equation for the borehole pressure can be written

$$p^I = p^{II}, \quad \text{at} \quad z = 0. \tag{5.3}$$

Compatible with the assumptions we have made, the continuity of fluid mass can be expressed as

$$A(v_z^I - v_z^{II}) = q(\omega), \quad \text{at} \quad z = 0, \tag{5.4}$$

where $A = \pi a^2$ is the cross sectional area of the borehole, $v_z^{I,II}$ are the vertical particle velocities, and q is given by

$$\begin{aligned} q(\omega) &= -\int_S \mathbf{v} \cdot \mathbf{n} \mathrm{d}S \\ &= -\left[\frac{\mathrm{i}kV}{\rho_f} + \frac{2\pi dh}{\mathrm{i}\rho_f v_f} \frac{H_1^{(1)}(kd)}{H_0^{(1)}(kd)} \right] p, \end{aligned} \tag{5.5}$$

where the integration is over the surface of the washout. In Equation (5.5), the first term inside the brackets represents the effect of the compressibility of the fluid in the washout volume, whereas the second represents the flow into the fracture. The pressure p in that equation is taken at $z = 0$.

Combining Equations (5.1)-(5.5) and solving for the reflection coefficient we obtain

$$R(\omega) = \frac{i[kV/2\pi a^2 - dhH_1^{(1)}(kd)/a^2 H_0^{(1)}(kd)]}{1 - i[kV/2\pi a^2 - dhH_1^{(1)}(kd)/a^2 H_0^{(1)}(kd)]}. \tag{5.6}$$

This expression is simple enough that it can be used as a model to predict the effective fracture aperture. The parameters such as V and d can be obtained from caliper logs. In Figure 5.2 we show the magnitude of the reflection coefficient as obtained from (5.6) as well as that obtained from the finite-difference fracture model (same as in Figure 4.16). The parameters for this model are the same as those of Section 4.5.5. The good agreement between the two models show that Equation (5.6) captures the essential features of the fracture-washout system. Obviously the analytic model is applicable only at low frequencies as assumed above where, to lowest order, only the volume of the washout is considered. Shape dependent factors would obviously have to be considered in order to extend this model to higher frequencies.

5.3 Formation Elasticity Effects

In this section we will develop a model of a borehole-fracture system that allows for the elasticity of the formation. In Figure 5.3 we show the geometry of this problem. At low enough frequencies the Stoneley wave in the borehole can be approximated by a tube wave with uniform pressure distribution across the borehole, as we have shown in Chapter 1. The pressure field in region (I) below the fracture consists of the incident and reflected fields

$$p^I = e^{ik_T z} + R(\omega)e^{-ik_T z}, \tag{5.7}$$

and that of region (II) above the fracture is

$$p^{II} = T(\omega)e^{ik_T z}, \tag{5.8}$$

where $k_T = \omega/v_T$. The tube wave velocity, v_T, is as given in Section 3.3.1. The Stoneley wave in an elastic medium is not very dispersive, thus justifying the use of the low frequency limit for its phase velocity.

As the tube wave interacts with the fluid-filled fracture it will couple energy into a mode which propagates outward into the fracture. In Appendix C we derive the dispersion relation for axi-symmetric modes in a fluid-filled fracture. In terms of the dimensionless radial wave number ($\bar{k}_r = k_r h$) and frequency ($\bar{\omega} = \omega h/v_f$) this dispersion relation takes the following form

$$\coth\left(\frac{1}{2}\sqrt{\bar{k}_r^2 - \bar{\omega}^2}\right) + \frac{\rho}{\rho_f}\frac{\sqrt{\bar{k}_r^2 - \bar{\omega}^2}}{(\bar{\omega}\epsilon_s/\epsilon)^4}\left\{\frac{[2\bar{k}_r^2 - (\bar{\omega}\epsilon_s/\epsilon)^2]^2}{\sqrt{\bar{k}_r^2 - (\bar{\omega}\epsilon_c/\epsilon)^2}} - 4\bar{k}_r^2\sqrt{\bar{k}_r^2 - (\bar{\omega}\epsilon_s/\epsilon)^2}\right\} = 0, \tag{5.9}$$

where ϵ, ϵ_c, and ϵ_s are defined in Appendix C. The fundamental mode which exists for all wavelengths has a phase velocity which is smaller than the acoustic wave velocity of the fluid. At high frequencies this mode becomes the Stoneley wave propagating along the fluid-solid interfaces. This mode is the two-dimensional analogue of the Stoneley wave in a fluid-filled borehole. At low frequencies, however, there is a fundamental difference between this mode and the tube wave. The compliance of the formation under a static pressure increase in the borehole is finite and equals μ^{-1}. In the fluid-filled fracture case the compliance of the two half spaces due to a static pressure in the fluid is infinite, thus leading to a phase velocity which approaches zero in the low frequency limit. From (5.9) it can be shown that

$$\lim_{\bar{k}_r \to 0} \bar{\omega}^2 = 2\bar{k}_r^2 \frac{\epsilon^2}{\epsilon_s^2}(1 - \frac{\epsilon_c^2}{\epsilon_s^2})$$

$$\times \left\{ \frac{2}{\bar{k}_r} \frac{\rho_f}{\rho} - \left[\frac{\epsilon_c^2}{\epsilon_s^2} \left(2 - \frac{\epsilon_c^2}{\epsilon_s^2} \right) + 2\frac{\epsilon^2}{\epsilon_s^2} \left(\frac{\epsilon_c^2}{\epsilon_s^2} - 1 \right) - \frac{1}{2} \right] \right\}^{-1} . \qquad (5.10)$$

In Figure 5.4 we show the phase velocity of this fundamental mode for a formation with properties as given in Table 4.2. The fracture aperture is taken as $h = 0.5$ cm. Notice that (5.10) is a good approximation for exact dispersion obtained by numerically tracking the roots of (5.9).

The pressure field in the fracture thus takes the form of an outgoing cylindrical wave given by

$$p_f(r,\omega) = p_f(a,\omega) \frac{H_0^{(1)}(k_r r)}{H_0^{(1)}(k_r a)}, \qquad (5.11)$$

where $p_f(a,\omega)$ is the pressure at the borehole wall and taken the same as $p(z = 0,\omega)$. Notice we have assumed that the pressure is uniform across the fracture aperture, since the wavelength is much larger than the aperture. We can now set up the problem as in the previous section and express the continuity conditions at $z = 0$ as

$$p^I - p^{II} = 0, \qquad (5.12)$$

$$A(v_z^I - v_z^{II}) = q(\omega). \qquad (5.13)$$

The flow into the fracture is given by

$$\begin{aligned} q(\omega) &= -\int_S \mathbf{v} \cdot \mathbf{n} dS \\ &= -\frac{2\pi a h k_r}{i\rho_f \omega} \frac{H_1^{(1)}(k_r a)}{H_0^{(1)}(k_r a)} p, \end{aligned} \qquad (5.14)$$

where $p = p(z = 0, \omega)$, and (ω, k_r) satisfy Equation (5.9). From Equations (5.7), (5.8), (5.12)-(5.13) we can solve for the reflection and transmission coefficients, thus obtaining

$$R(\omega) = -\frac{\mathrm{i}hk_r H_1^{(1)}(k_r a)/aH_0^{(1)}(k_r a)}{k_T + \mathrm{i}hk_r H_1^{(1)}(k_r a)/aH_0^{(1)}(k_r a)}, \tag{5.15}$$

$$T(\omega) = \frac{k_T}{k_T + \mathrm{i}hk_r H_1^{(1)}(k_r a)/aH_0^{(1)}(k_r a)}. \tag{5.16}$$

If the formation is rigid, then $k_r = k_T = \omega/v_f$ and Equations (5.15) and (5.16) reduce to those obtained by Hornby *et al.* (1989).

In Figure 5.5 we show the magnitude of the reflection coefficient for a fracture with an aperture of 0.5 cm. The borehole and formation properties are given in Table 4.2. For the purpose of comparison we also plot in that figure the results of the finite-difference computation performed in the previous chapter. Notice the good agreement between the finite-difference estimates of the reflection coefficient versus Equation (5.15). The predictions from Equation (5.15) are virtually indistinguishable whether we use the exact [Equation (5.9)] or the approximate [Equation (5.10)] dispersion relations.

5.4 Fractured and Permeable Zones

As illustrated in Figure 5.1, the occurrence of multiple fractures is not rare but actually quite common, such as in carbonate formations. Their effects on the reflection and/or transmission of tube waves is important and we will develop some simple analytical models to better understand these effects. We will, however, assume that the formation is rigid for simplicity.

For a single fracture we can simply set $k_r = k_T = k = \omega/v_f$ in (5.15) and (5.16) to get

$$R(\omega) = -\frac{\mathrm{i}hH_1^{(1)}(ka)/aH_0^{(1)}(ka)}{1 + \mathrm{i}hH_1^{(1)}(ka)/aH_0^{(1)}(ka)}, \tag{5.17}$$

$$T(\omega) = \frac{1}{1 + \mathrm{i}hH_1^{(1)}(ka)/aH_0^{(1)}(ka)}. \tag{5.18}$$

In Figure 5.6 we show the magnitudes of the reflection and transmission coefficients for a fracture with $h = 0.5$ cm. Notice that as $\omega \to 0$ we have $R(\omega) \to -1$ for an inviscid fluid since the fracture acts as a pressure release surface. We will next build upon this model by including multiple fractures and the viscosity of the fluid.

5.4.1 Multiple Fractures

Referring to Figure 5.7, let us focus our attention at the pressure field above and below a particular fracture located at $z = z_i$ $(i = 1, ..., N)$. The pressure field in region $z_{i-1} < z < z_i$ is given by

$$p^{(i)} = \begin{bmatrix} e^{\mathrm{i}(kz-\omega t)} & e^{\mathrm{i}(-kz-\omega t)} \end{bmatrix} \begin{bmatrix} U^{(i)}(\omega) \\ D^{(i)}(\omega) \end{bmatrix}, \tag{5.19}$$

and that in the region $z_i < z < z_{i+1}$ is

$$p^{(i+1)} = \begin{bmatrix} e^{\mathrm{i}(kz-\omega t)} & e^{\mathrm{i}(-kz-\omega t)} \end{bmatrix} \begin{bmatrix} U^{(i+1)}(\omega) \\ D^{(i+1)}(\omega) \end{bmatrix}, \tag{5.20}$$

where $U(\omega)$ and $D(\omega)$ are the amplitude of the upgoing and downgoing waves, respectively.

The continuity conditions at the fracture locations $z = z_i$ are expressed as

$$p^{(i)} - p^{(i+1)} = 0, \tag{5.21}$$

$$A\left(v_z^{(i)} - v_z^{(i+1)}\right) = q^{(i)}(\omega), \tag{5.22}$$

where

$$\begin{aligned} q^{(i)}(\omega) &= -\int_{S_i} \mathbf{v} \cdot \mathbf{n} dS \\ &= -\frac{2\pi a h_i}{\mathrm{i}\rho_f v_f} \frac{H_1^{(1)}(ka)}{H_0^{(1)}(ka)} p_i. \end{aligned} \tag{5.23}$$

In (5.23) p_i is the borehole pressure at $z = z_i$. The upgoing and downgoing amplitudes are related by the reflection coefficient as

$$D^{(i)}(\omega) = R^{(i)}(\omega)\, U^{(i)}(\omega), \quad (i = 1, ..., N). \tag{5.24}$$

The system of equations (5.21)-(5.24) can be solved recursively by starting at the uppermost region $(N+1)$ where

$$R^{(N+1)}(\omega) \equiv 0. \tag{5.25}$$

In the next section we will show results from such a calculation.

5.4.2 Viscous Effects

In all previous models the effects of fluid viscosity have been neglected since the viscous skin depth $\delta = \sqrt{2\eta/\rho_f\omega}$ was small when compared to h (η is the fluid viscosity). When we consider fractured zones such as shown in Figure 5.1 it may be necessary to consider these effects as the fracture apertures become of the order of tens of μm. Also, from a theoretical viewpoint it is useful to describe the medium as a porous permeable medium (Biot, 1956, 1962; Johnson, 1986), characterized by a permeability κ_0, and where viscosity effects become significantly important.

Our intention is to generalize the procedure of the previous section but with the inclusion of viscous effects in the fracture. We will do so by starting from a general formalism for acoustics in porous media such as developed in Johnson *et al.* (1987). Let $\mathbf{v}$ be a macroscopically averaged fluid velocity, defined in such a way that $\phi\mathbf{v}\cdot\mathbf{n}A$ is the amount of fluid crossing a macroscopic surface of area A having an outward normal $\mathbf{n}$; ϕ is the porosity of the medium. The fluid velocity and the macroscopic pressure gradient driving the flow are related through

$$\alpha(\omega)\rho_f\frac{\partial \mathbf{v}}{\partial t} = -\nabla p, \tag{5.26}$$

$$\phi\mathbf{v} = -\frac{\kappa(\omega)}{\eta}\nabla p, \tag{5.27}$$

where $\alpha(\omega)$ and $\kappa(\omega)$ are the dynamic tortuosity and permeability, respectively. From (5.26) and (5.27) we get the relationship between these two quantities

$$\alpha(\omega) = \frac{\mathrm{i}\eta\phi}{\kappa(\omega)\omega\rho_f}. \tag{5.28}$$

The constitutive relation for the fluid is given by

$$\frac{\partial p}{\partial t} = -\rho_f v_f^2 \nabla \cdot \mathbf{v}. \tag{5.29}$$

Assuming $e^{-i\omega t}$ dependence for all variables, we get from Equations (5.26)-(5.29) the following equation for the pressure

$$\nabla^2 p + \alpha(\omega)\, k^2\, p = 0, \tag{5.30}$$

where $k = \omega/v_f$. We notice that Equation (5.30) is the same as that obtained for an inviscid fluid, but with a renormalized fluid speed $\tilde{v}_f = v_f/\sqrt{\alpha(\omega)}$.

Returning to the problem of a single fracture filled with a viscous fluid, we can express the pressure disturbance in the fracture, as excited by the tube wave in the borehole, in the following form

$$p_f(r,\omega) = p_f(a,\omega)\frac{H_0^{(1)}(\tilde{k}r)}{H_0^{(1)}(\tilde{k}a)}, \tag{5.31}$$

where $\tilde{k} = \sqrt{\alpha(\omega)}\,\omega/v_f$, and $p_f(a,\omega)$ is the pressure at the borehole wall taken the same as $p(z=0,\omega)$. The frequency dependent tortuosity given by Johnson *et al.* (1987) can be expressed in terms of the parameters for a planar fracture of constant aperture h as

$$\alpha(\omega) = 1 + \frac{12i\eta}{h^2\omega\rho_f}\left(1 - \frac{ih^2\omega\rho_f}{36\eta}\right)^{1/2}. \tag{5.32}$$

The formalism used in the previous section can now be generalized by simply replacing the expression obtained for the flow into the fracture [Equation (5.23)] by that derived from (5.31). For a single fracture we thus get

$$R(\omega) = -\frac{ihH_1^{(1)}(\tilde{k}a)/a\sqrt{\alpha(\omega)}H_0^{(1)}(\tilde{k}a)}{1 + ihH_1^{(1)}(\tilde{k}a)/a\sqrt{\alpha(\omega)}H_0^{(1)}(\tilde{k}a)} \tag{5.33}$$

$$T(\omega) = \frac{1}{1 + ihH_1^{(1)}(\tilde{k}a)/a\sqrt{\alpha(\omega)}H_0^{(1)}(\tilde{k}a)}. \tag{5.34}$$

To illustrate these results we consider a fracture zone of width $H = 1.524$ m (5 feet) with N uniformly spaced fractures, all with the same aperture $h_i = h$ $(i = 1, ..., N)$.

The total fracture aperture is taken as $\sum_{i=1}^{N} h_i = 5.6$ mm. In Figure 5.8 we show the magnitude of the tube wave reflection coefficient for the cases where the number of fractures is $N = 21, 41, 61, 81$, and 101. The notches in this figure correspond to frequencies ω_n at which $n\lambda_n/2 = H$ $(n = 1, 3, \ldots)$, where λ_n is the wavelength at frequency ω_n. Notice that as frequency increases, the viscous effects become less important $(\delta \ll h)$ and all curves tend to overlay. In Figure 5.9 we show the magnitude of the tube wave reflection coefficient for a single fracture with an aperture of 5.6 mm and for a collection of 101 fractures with the same total aperture. In this latter case we computed the reflection coefficient with and without viscous effects. At very low frequencies the single and the inviscid multiple fracture cases give the same results as expected, where the tube wave sees only the total aperture. At higher frequencies, however, there are significant differences between these two cases since it will depend on how the total aperture is distributed in the borehole. The two models for the multiple fractures (viscous and non-viscous) give the same reflection coefficient at high frequencies, since the viscous skin depth becomes much smaller than the individual fracture aperture. At low frequencies they give drastically different results since now the viscous skin depth becomes comparable to the fracture aperture.

5.4.3 Permeable Zone

In this section we will compare the results obtained for the multiple fractures with viscous effects taken into account and that for a permeable layer of thickness H and permeability κ_0 (refer to Figure 5.10). This latter problem can be formulated just as the multiple fracture case by assuming that in the borehole region opposite the permeable layer there are upgoing and downgoing waves propagating with wavenumber k^*. We will take k^* as that arising from an infinite permeable medium surrounding the borehole. It is easy to show that an approximate form for k^* is given by

$$k^* = \sqrt{k^2 - \frac{2\,\mathrm{i}\,k\,\eta\,\phi}{\alpha(\omega)}[\alpha(\omega) - 1]^{\frac{1}{2}}\,\frac{H_1^{(1)}([\alpha(\omega) - 1]^{\frac{1}{2}}\,k\,a)}{H_0^{(1)}([\alpha(\omega) - 1]^{\frac{1}{2}}\,k\,a)}}. \tag{5.35}$$

This equation agrees with that obtained by Tang and Cheng (1993). The frequency dependent tortuosity is given by (Johnson *et al.*, 1987)

$$\alpha(\omega) = \alpha_\infty + \frac{i\,\eta\,\phi}{\kappa_0\,\omega\,\rho_f}\left(1 - \frac{4\,\mathrm{i}\,\alpha_\infty\,\kappa_0\,\omega\,\rho_f}{\eta\,\Lambda^2\,\phi^2}\right)^{\frac{1}{2}}, \tag{5.36}$$

where α_∞ is the high frequency limit of the tortuosity which can be obtained from electrical conductivity measurements, and Λ is a characteristic length related to the *dynamically connected* pore sizes (Johnson *et al.*, 1986). To compare with the multiple fracture cases we take $\Lambda = h$, $\kappa_0/\phi = h^2/12$, and $\alpha_\infty = 1$. In Figure 5.11 we show the tube wave reflection coefficient for the multiple fracture case ($N = 101$) and the permeable layer. The good agreement shows the equivalence of the two approaches. Obviously at high frequencies the small differences come from the intrinsic discreteness of the fractures when compared to the continuous porous permeable layer.

5.5 Discussion and Conclusions

Inasmuch as open fluid-filled fractures reflect impinging tube waves, other factors such as the environmental condition of the borehole also give rise to reflections. Furthermore, the elasticity of the formation as well as the presence of multiple fractures will affect the actual magnitude of the reflection. Simple models which ignore these factors cannot be used for quantitative interpretation based on reflection/transmission of tube waves. In this chapter we have developed a series of models, which, due to their analytic nature, lend themselves to practical implementation. In this vein, we obtained a model for interpreting the tube wave reflection coefficient when the borehole region near the fracture has been washed out or caved in. An estimate of the volume of this region is needed, and can be obtained independently from caliper logs. A frequent problem which leads to false fracture identification is caused by regions where only washouts or caves exist, since by themselves they cause tube wave reflections. We have shown that the behaviour of the reflection coefficient versus frequency can be used to identify these cases.

The elasticity of the formation also affects the reflection of tube waves. The simple analytical model we have developed uses information from the head wave arrivals,*i.e.*, the compressional and shear wave speeds, to predict the reflectivity of tube waves. It can be used to invert for the fracture aperture, which otherwise would be overestimated by a model based on a rigid formation assumption.

Finally we showed the equivalence between a fractured zone and a layer composed of a permeable material characterized by a permeability κ_0. The question of when to use a single equivalent fracture versus a distributed multiple fracture model (or its equivalent) can be addressed by the character of the reflection coefficient versus frequency. Notches in the response curve indicate that a finite thickness zone is present. Alternatively, this question can be answered readily if borehole scans (ultrasonic or electrical) are available.

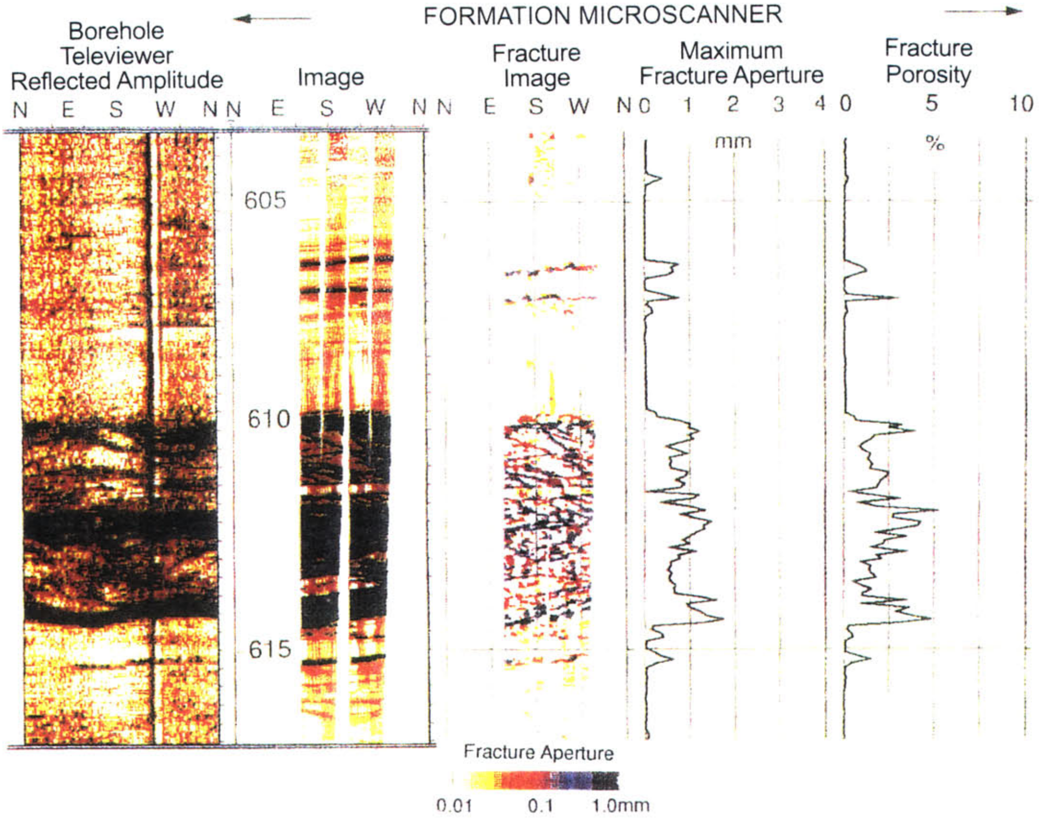

Figure 5.1: Display of the ultrasonic borehole scan (BHTV), the electrical borehole scan, and the fracture-aperture and fracture-porosity computation from the borehole scan [from Hornby *et al.* (1992)].

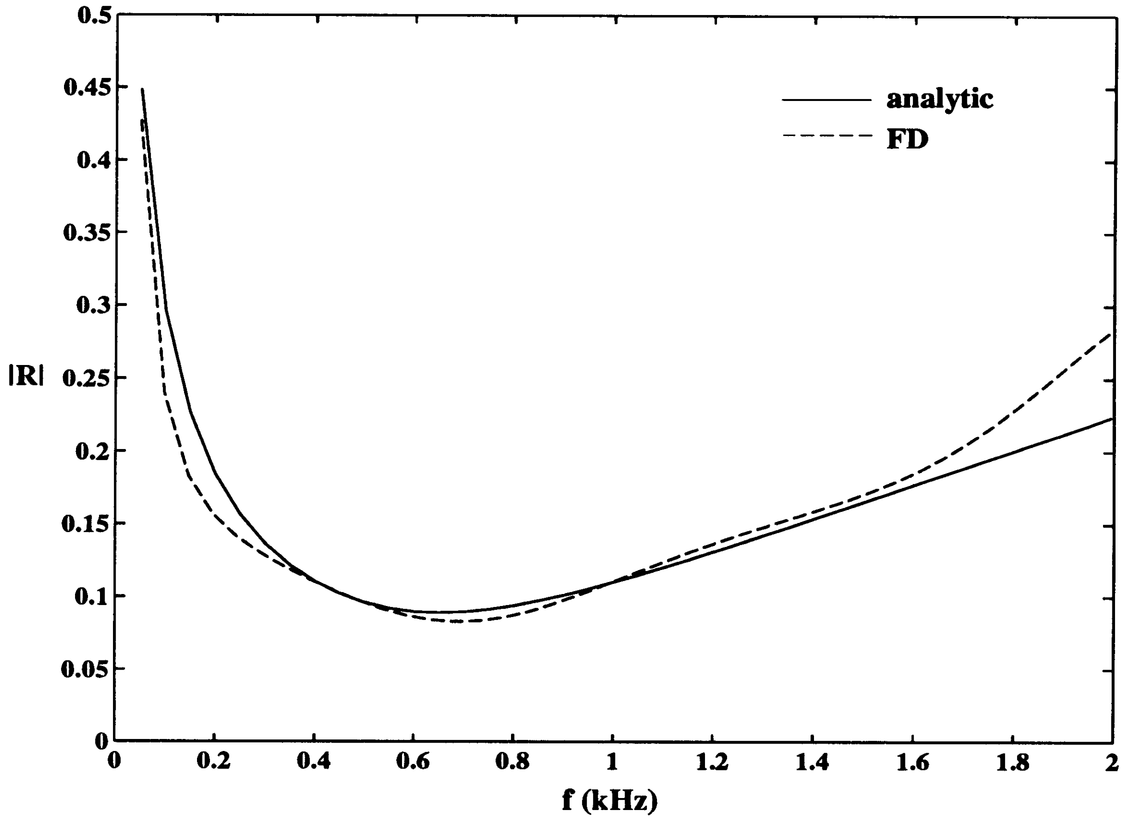

Figure 5.2: Magnitude of the Stoneley wave reflection coefficient for the combined washout and fluid-filled fracture (rigid formation).

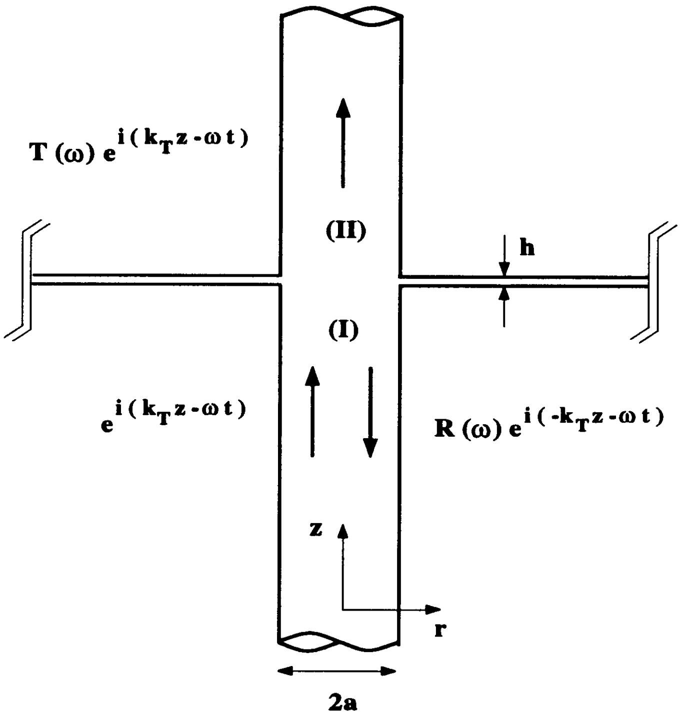

Figure 5.3: Horizontal fluid-filled fracture intersecting a borehole in an elastic formation. Incident, transmitted, and reflected waves are indicated.

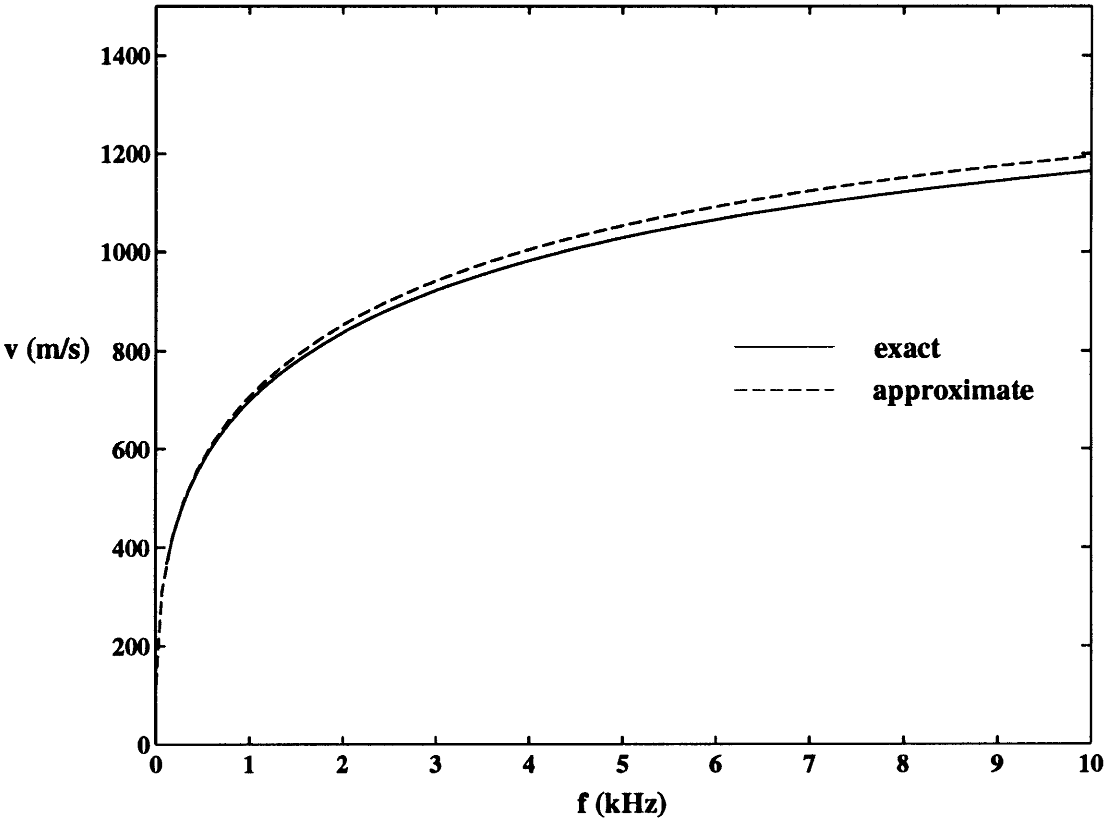

Figure 5.4: Velocity dispersion of the fundamental mode in a fluid-filled fracture bounded by two elastic half spaces.

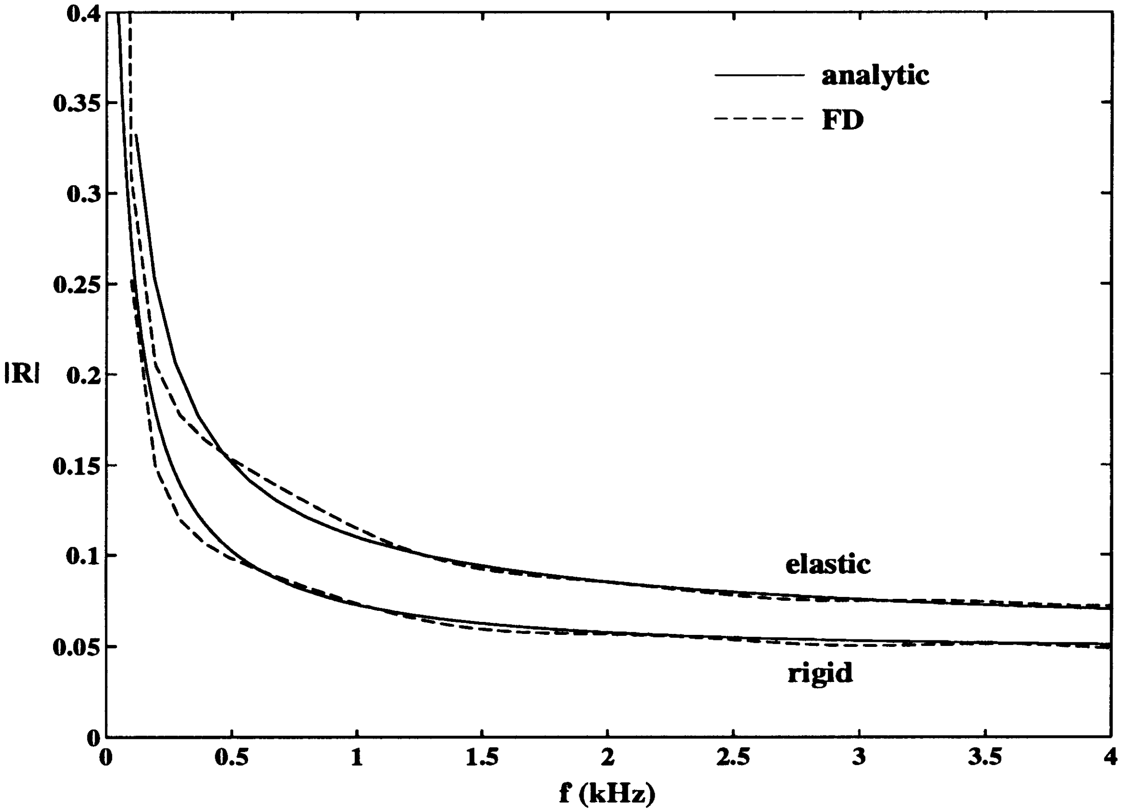

Figure 5.5: Magnitude of the Stoneley wave reflection coefficient for a 0.5 cm aperture fluid-filled fracture.

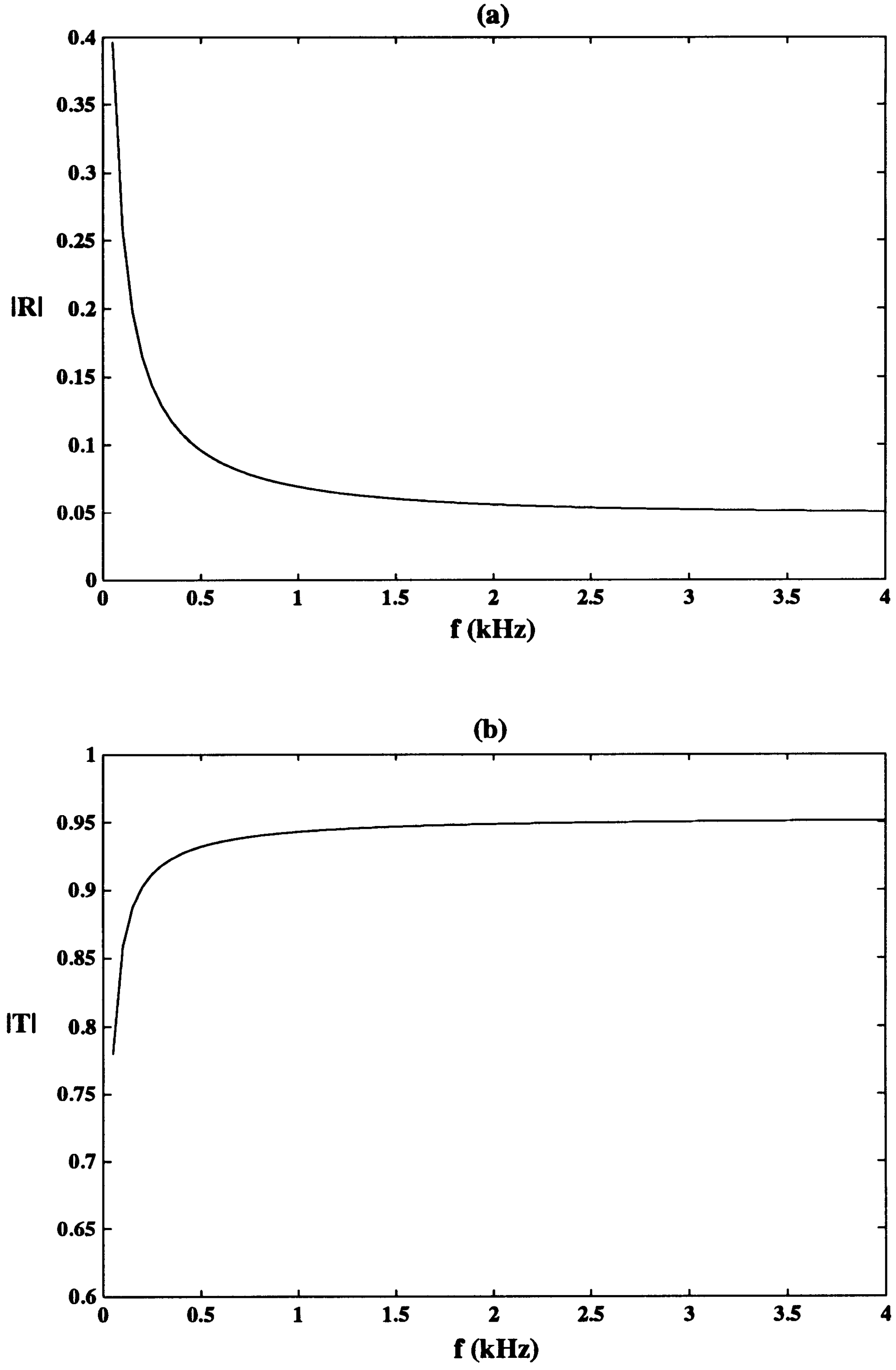

Figure 5.6: Magnitude of the Stoneley wave reflection (a) and transmission (b) coefficients for a 0.5 cm aperture fluid-filled fracture.

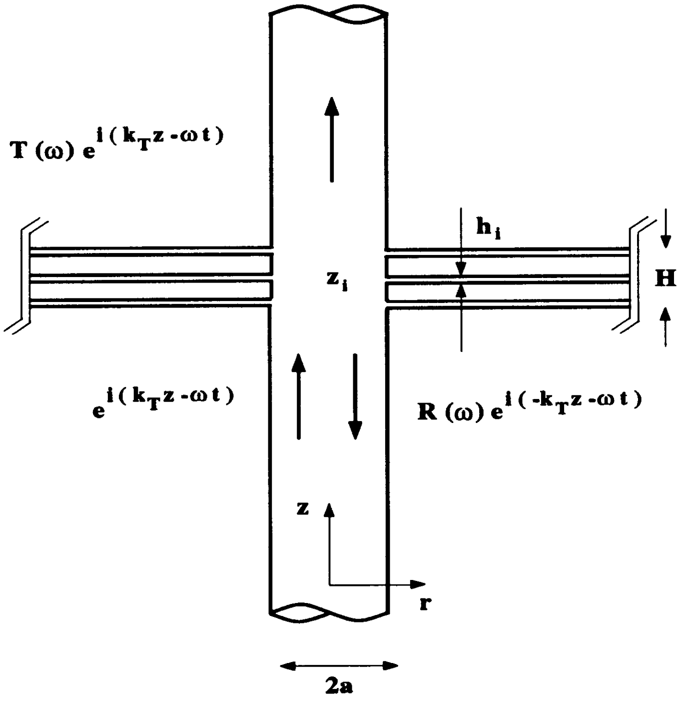

Figure 5.7: Horizontal fluid-filled fractures intersecting a borehole. Incident, transmitted, and reflected waves are indicated.

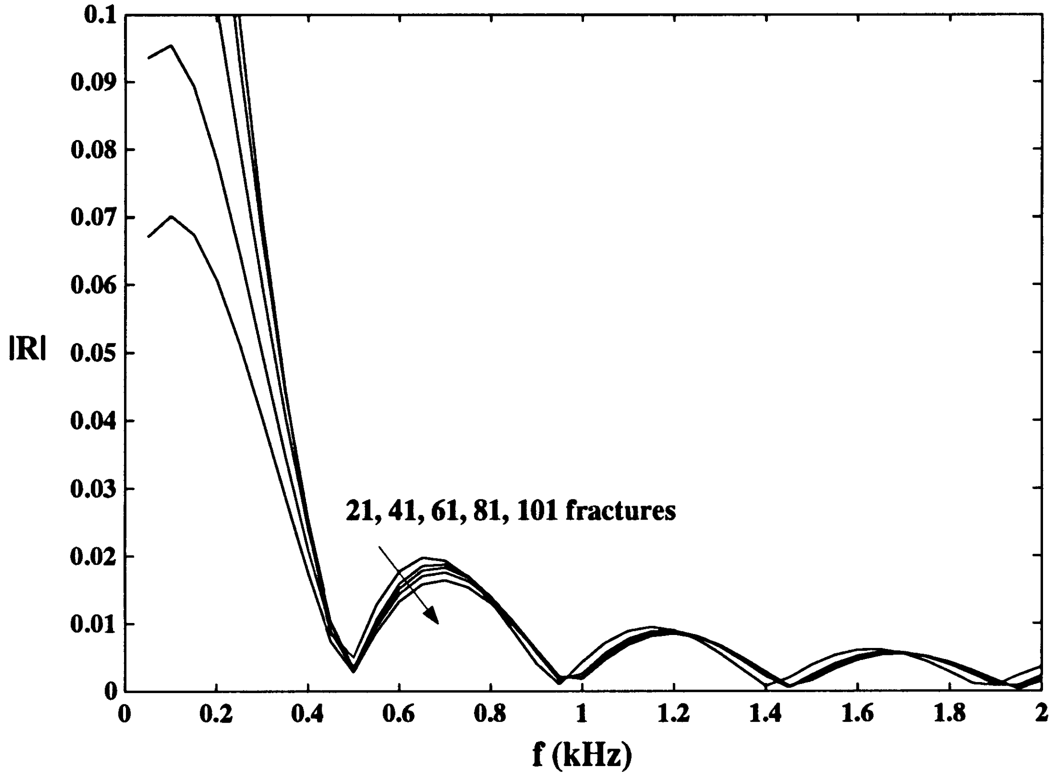

Figure 5.8: Magnitude of Stoneley wave reflection coefficient for multiple fractures.

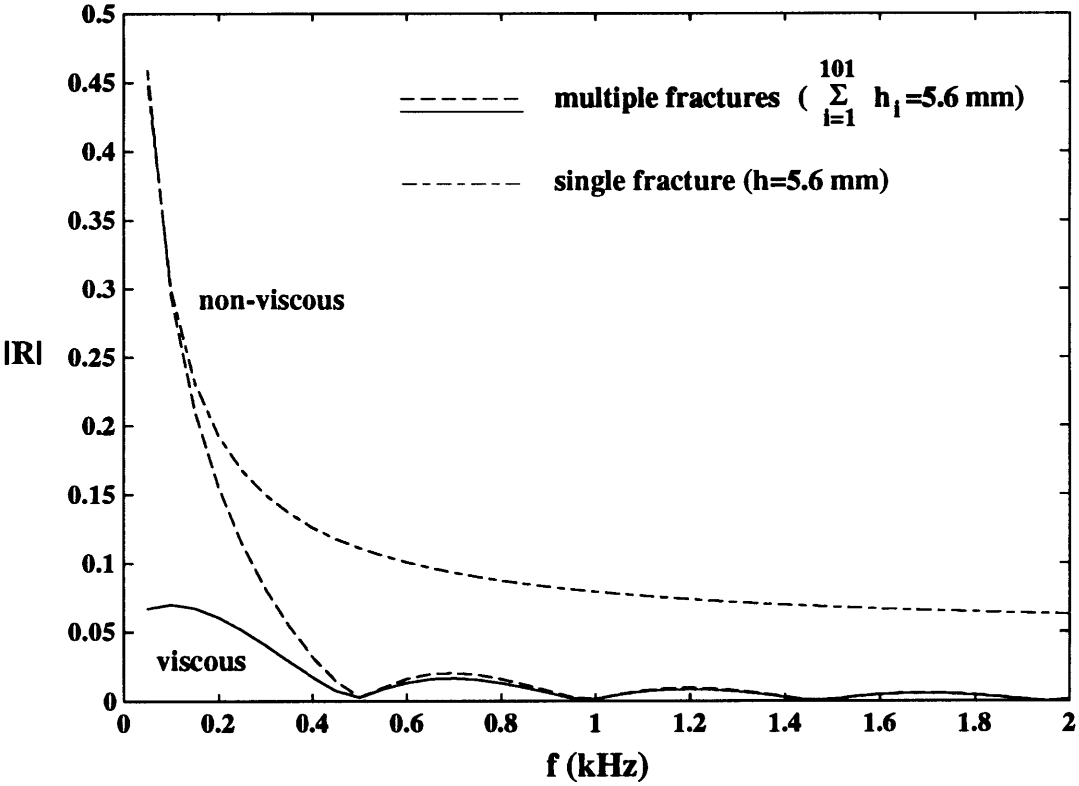

Figure 5.9: Magnitude of Stoneley wave reflection coefficient for single and multiple fractures with and without viscous effects taken into consideration.

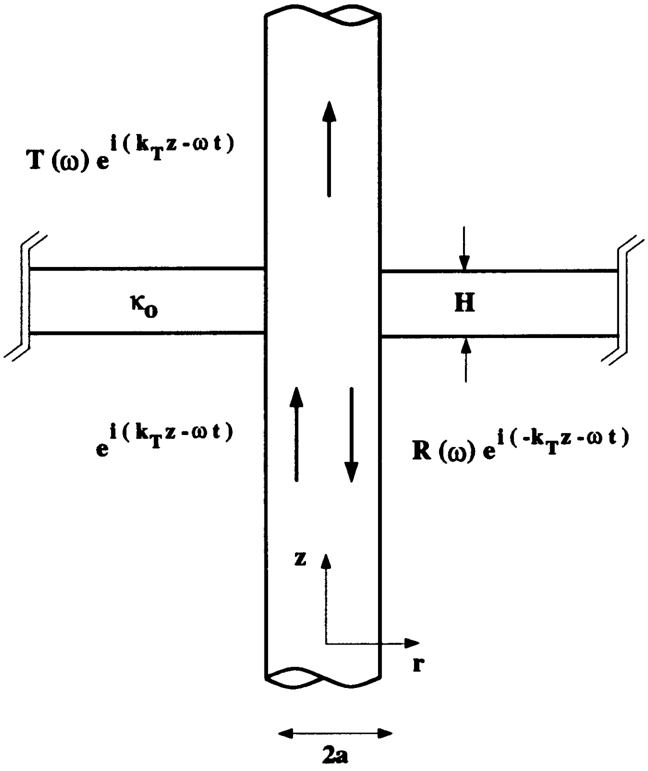

Figure 5.10: Permeable layer intersecting a borehole.

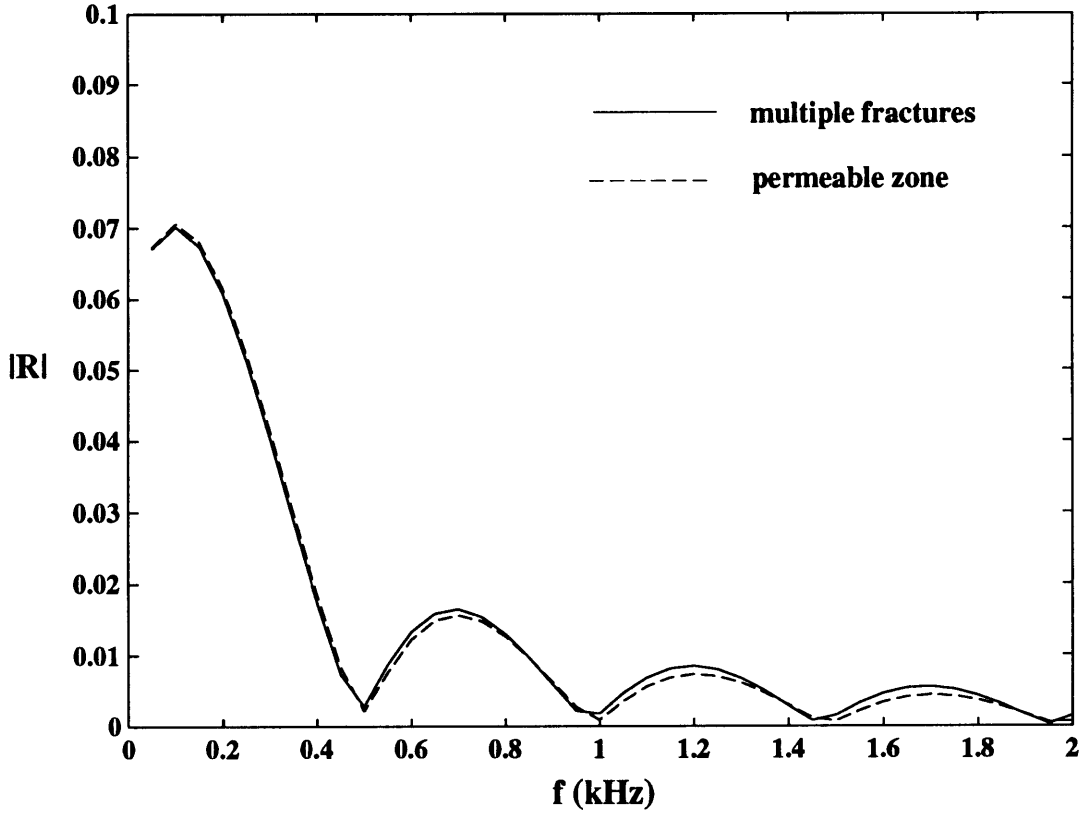

Figure 5.11: Magnitude of Stoneley wave reflection coefficient for multiple fractures and a permeable layer.

Chapter 6

Nonlinear Effects

6.1 Introduction

The simple fact that a solid expands when its temperature is raised shows the anharmonicity of the interatomic potential. In fact, first-order asymmetry of interatomic forces manifests itself macroscopically in terms of the so-called third-order elastic constants. Measuring these constants allows for the evaluation of first-order anharmonic terms of the interatomic potential, which has many applications in solid-state physics. In addition, the microstructure of the solid, such as dislocations, micropores, microcrevices, etc., also gives rise to an additional nonlinear behaviour which can often dominate the effect due to asymmetry of interatomic forces.

The third-order elastic constants [see Brugger (1964) for a thermodynamic definition] can be determined from velocity measurements on small amplitude sound waves in statically stressed media (Hughes and Kelly, 1953). Sedimentary rocks can have enormously large values of the third-order elastic constants. To illustrate this fact we consider the dependence of the compressional (v_c) and shear (v_s) wave speeds on confining pressure. These are best expressed in terms of the dimensionless parameters given by (Hughes and Kelly, 1953; Toupin and Bernstein, 1961)

$$
\begin{aligned}
\rho_0 \frac{\mathrm{d}v_c^2}{\mathrm{d}P} &= -\frac{7\lambda + 10\mu + c_{111} + 2c_{112}}{3\lambda + 2\mu}, \\
\rho_0 \frac{\mathrm{d}v_s^2}{\mathrm{d}P} &= -\frac{3\lambda + 6\mu + c_{111}/2 - c_{123}/2}{3\lambda + 2\mu},
\end{aligned}
\qquad (6.1)
$$

where c_{111}, c_{112}, and c_{123} are the so-called third-order elastic constants for an isotropic solid, and ρ_0 is its density in the undeformed state. The relationship between these constants and others which have appeared in the literature is shown in Table D.1 of Appendix D. In Table 6.1 we list some values of the dimensionless quantities in Equation (6.1) for a variety of materials.

In Figure 6.1 we plot the compressional and shear wave speeds for a dry Boise sandstone (Toksöz *et al.*, 1976) as a function of pressure. The solid lines are simply smooth curves constructed for the purposes of differentiation, according to (6.1). The results are plotted in Figure 6.2 where we see that for this rock the size of the nonlinear parameters relative to the linear can be orders of magnitude larger than for the materials listed in Table 6.1. Indeed nonlinear phenomena seem to be easily observed in rocks (Johnson *et al.*, 1987; Johnson and Shankland, 1989; Johnson *et al.*, 1991; Meegan *et al.*, 1992; Johnson *et al.*, 1992).

The microstructure of the rocks (microcracks, grain-to-grain contacts, etc.) clearly give rise to this highly nonlinear behaviour. These structural inhomogeneities act as nucleation sites for failure, whose initial stages are accompanied by the movement of dislocations, the development of a system of microcracks, the opening of the microcracks and pores, the formation of macrocracks, and finally, failure. Laboratory studies (Shkolnik *et al.*, 1990) showed that higher-order elastic constants are much more sensitive than the linear constants to detect such inhomogeneities. Thus, there is the possibility of directly assessing the mechanical behaviour of rocks, which is very important for predicting borehole stability during drilling, hydraulic fracturing, and sanding during production (Holt *et al.*, 1989).

As a means of measuring in-situ rock nonlinearity, we study in this chapter the effects of prestressing the formation around the borehole and its effects on the phase velocity of borehole modes. The formalism is general and valid for all borehole modes, but we concentrate on the effects on Stoneley waves.

In the following sections we derive the relevant equations for small amplitude wave propagation in a prestressed medium, and a perturbation theory for computing the change in modal phase velocity. We show computational results for a borehole in a moderately nonlinear formation.

6.2 Small on Large Theory

In this section we will develop the relevant equations that govern wave propagation under prestress. Previous work related to crystals can be found in Tiersten (1978), Sinha and Tiersten (1979), and Sinha (1982). In the usual manner, we define three states of the material: the *undeformed*, the *intermediate*, and the *dynamic*. In the undeformed or reference condition the material is unstressed with position vector $\mathbf{X}$. The intermediate or initial state corresponds to the stressed but static configuration, with associated position vector $\mathbf{x}$. We are interested in the dynamic or present state in which there is further deformation above and beyond that due to the stress. Let $\mathbf{y}$ denote the positions in the dynamic state, and define the associated displacements $\mathbf{w}$ and $\mathbf{u}$ by

$$\begin{aligned} \mathbf{x}(\mathbf{X}) &= \mathbf{X} + \mathbf{w}(\mathbf{X}), & (6.2) \\ \mathbf{y}(\mathbf{X}, t) &= \mathbf{X} + \mathbf{w}(\mathbf{X}) + \mathbf{u}(\mathbf{X}, t), & (6.3) \end{aligned}$$

$\mathbf{X}$ and $\mathbf{y}$ are sometimes referred to as Lagrangian and Eulerian coordinates, respectively. The equations for motion are (Eringen and Suhubi, 1974)

$$\rho_0 \frac{\partial^2 \mathbf{y}}{\partial t^2} = \nabla_X \cdot \mathbf{S}. \qquad (6.4)$$

Here, ρ_0 is the density in the reference state, and $\mathbf{S}$ is the Piola- Kirchhoff stress tensor of the first kind. The subscript in ∇_X means that partial differentiations are with respect to the reference coordinates $\mathbf{X}$. Assuming the existence of a strain energy function U per unit mass, then it may be shown that (Eringen and Suhubi, 1974)

$$S_{Mi} = \rho_0 \, y_{i,N} \frac{\partial U}{\partial E_{MN}}, \tag{6.5}$$

where " $_{,N}$ " denotes $\partial / \partial X_N$, and the summation convention on repeated subscripts is assumed $(i, N, M = 1, 2, 3)$. The Lagrangian (Green) strain tensor is given by

$$E_{MN} = \frac{1}{2}(y_{i,M} \, y_{i,N} - \delta_{MN}). \tag{6.6}$$

Note that the Piola-Kirchhoff stress tensor is not symmetric, $S_{Mi} \neq S_{iM}$.

We now make the "small on large" assumption that

$$\mathbf{u} \ll \mathbf{w}, \tag{6.7}$$

and that the associated deformation gradients are similarly related, $\partial \mathbf{u} / \partial \mathbf{X} \ll \partial \mathbf{w} / \partial \mathbf{X}$. Then it is possible to expand quantities for the dynamic state about their values in the intermediate state. Expanding Equations (6.5) and (6.6) for small-on-large deformations yields

$$S_{Mi} = S^1_{Mi} + G_{MiQk} \, u_{k,Q} + \dots \,, \tag{6.8}$$

where the superscript " ^{1} " denotes quantities in the intermediate state, *i.e.*, with $\mathbf{u} = \mathbf{0}$, and

$$G_{MiQk} = \left. \frac{\partial S_{Mi}}{\partial u_{k,Q}} \right|_1 . \tag{6.9}$$

Using Equations (6.2), (6.5), and (6.6), we find

$$\begin{aligned} G_{MiQk} &= \rho_0 \left. \frac{\partial U}{\partial E_{MQ}} \right|_1 \delta_{ik} + \rho_0 \left. \frac{\partial^2 U}{\partial E_{MN} \partial E_{QP}} \right|_1 (\delta_{iN} + w_{i,N})(\delta_{kP} + w_{k,P}) \\ &\approx \rho_0 \left. \frac{\partial U}{\partial E_{MQ}} \right|_1 \delta_{ik} + \rho_0 \left. \frac{\partial^2 U}{\partial E_{Mi} \partial E_{Qk}} \right|_1 \\ &\quad + \rho_0 \left. \frac{\partial^2 U}{\partial E_{Mi} \partial E_{QP}} \right|_1 w_{k,P} + \rho_0 \left. \frac{\partial^2 U}{\partial E_{MP} \partial E_{Qk}} \right|_1 w_{i,P} \,, \end{aligned} \tag{6.10}$$

where we have ignored terms of quadratic or higher order in $w_{i,P}$. We next assume that U can be expanded as

$$\rho_0 U = \frac{1}{2} C_{ABCD} E_{AB} E_{CD} + \frac{1}{6} C_{ABCDEF} E_{AB} E_{CD} E_{EF} + \dots . \tag{6.11}$$

Then it is straightforward to show, using (6.10), (6.11), and $E^1_{AB} = \frac{1}{2}(w_{A,B} + w_{B,A}) + \dots$, that

$$\begin{aligned} G_{MiQk} &= C_{MiQk} + C_{MQPl}\, w_{l,P}\, \delta_{ik} \\ &\quad + C_{MiQP}\, w_{k,P} + C_{MPQk}\, w_{i,P} + C_{MiQkPl}\, w_{l,P} . \end{aligned} \tag{6.12}$$

The most general form of the stress is thus

$$S_{Mi} = S_{Mi}\big|_1 + G_{MiQk}\, u_{k,Q} + O(u^2_{k,Q}). \tag{6.13}$$

The effective linear elastic moduli depend upon the prestrain according to

$$G_{MiQk} = C_{MiQk} + B_{MiQkPl}\, w_{l,P} , \tag{6.14}$$

where the second-order moduli C_{MiQk} are independent of the prestrain and satisfy the usual symmetries for anisotropic linear elasticity,

$$C_{ABCD} = C_{BACD} , \qquad C_{ABCD} = C_{CDAB} . \tag{6.15}$$

Also,

$$B_{MiQkPl} = C_{MiQkPl} + C_{MQPl}\, \delta_{ik} + C_{MiQP}\, \delta_{kl} + C_{MPQk}\, \delta_{il} , \tag{6.16}$$

where C_{MiQkPl} are the third-order moduli, with symmetries

$$C_{ABCDEF} = C_{BACDEF} , \qquad C_{ABCDEF} = C_{CDABEF} = C_{EFCDAB} . \tag{6.17}$$

In general the effective moduli G_{MiQk} possess none of the symmetries given in (6.15). We conclude this subsection by noting that the equilibrium equations for the small deformation follows from (6.4) and the fact that the intermediate state is one of static equilibrium, as

$$\rho_0 \frac{\partial^2 u_i}{\partial t^2} = (G_{MiQk}\, u_{k,Q})_{,M} . \tag{6.18}$$

These equations are expressed in terms of the reference or Lagrangian coordinates, $\mathbf{X}$, as distinct from both the initial (intermediate) coordinates $\mathbf{x}$ and the present or Eulerian coordinates, $\mathbf{y}$.

6.3 Modal Perturbation Theory

We now consider the effects of the prestress on modes in a borehole. Our analysis follows that of Sinha *et al.* (1992). The stressed medium is viewed as a perturbation of the original material. Formal perturbation methods can be used if we introduce a small parameter, $\epsilon \ll 1$, such that

$$\begin{aligned} G_{MiQk} &= C_{MiQk} + \Delta C_{MiQk} \\ &= C_{MiQk} + \epsilon\, \Delta \hat{C}_{MiQk} . \end{aligned} \tag{6.19}$$

Note that the unperturbed moduli C_{MiQk} satisfy the symmetries (6.15) but the perturbed moduli ΔC_{MiQk} do not. The modes and the resonance frequencies are expanded as

$$\mathbf{u} = \mathbf{u}^{(0)} + \epsilon\, \mathbf{u}^{(1)} + \dots , \tag{6.20}$$

$$\omega = \omega^{(0)} + \epsilon\, \omega^{(1)} + \dots . \tag{6.21}$$

For simplicity, we have not labelled these variables with an index for the modal order, $m = 0, 1, 2, \dots$. We then substitute these expansions into the equations of motion (6.18), assuming time dependence of the form $e^{-i\omega t}$. Comparing terms of similar powers in ϵ implies a sequence of equations, the first two of which are

$$O(1): \quad C_{MiQk}\, u^{(0)}_{k,QM} + \rho_0 \left(\omega^{(0)}\right)^2 u^{(0)}_i = 0 \tag{6.22}$$

$$\begin{aligned} O(\epsilon): \quad C_{MiQk}\, u^{(1)}_{k,QM} + \rho_0 \left(\omega^{(0)}\right)^2 u^{(1)}_i &= -\Big[\left(\Delta \hat{C}_{MiQk}\, u^{(0)}_{k,Q}\right)_{,M} \\ &\quad + 2\, \rho_0\, \omega^{(0)}\, \omega^{(1)}\, u^{(0)}_i\Big] . \end{aligned} \tag{6.23}$$

Thus, $\mathbf{u}^{(0)}$ is the mode for the unstressed medium, and $\omega^{(0)}$ is the associated frequency.

We next multiply the $O(\epsilon)$ equation by $u_i^{(0)}$ and integrate by parts over the entire volume. In simplifying the integral we use the fact that the Piola-Kirchhoff stress due to the dynamic motion is, from (6.13),

$$\begin{aligned} P_{Mi} &= G_{MiQk}\, u_{k,Q}^{(0)} + \ldots \\ &= P_{Mi}^{(0)} + \epsilon\, P_{Mi}^{(1)} + \ldots . \end{aligned} \tag{6.24}$$

The interface contitions are that the traction associated with $\mathbf{P}$ is everywhere continuous, and hence the tractions due to $\mathbf{P}^{(0)}$ and $\mathbf{P}^{(1)}$ are each continuous across the interface. Also, the condition at infinity requires that the fields decay to zero, implying that both the leading order and $O(\epsilon)$ fields behave likewise. Focusing on the $O(\epsilon)$ tractions, we see that

$$\begin{aligned} &\int_V u_i^{(0)} \left[C_{MiQk}\, u_{i,QM}^{(1)} + (\Delta\hat{C}_{MiQk}\, u_{k,Q}^{(0)})_{,M}\right] \mathrm{d}V \\ &= \int_V u_i^{(0)}\, P_{Mi,M}^{(1)}\, \mathrm{d}V \\ &= \int_V u_{i,M}^{(0)}\, P_{Mi}^{(1)}\, \mathrm{d}V \\ &= \int_V u_{i,M}^{(0)} \left(C_{MiQk}\, u_{k,Q}^{(1)} + \Delta\hat{C}_{MiQk}\, u_{k,Q}^{(0)}\right) \mathrm{d}V\,, \end{aligned} \tag{6.25}$$

where $\mathrm{d}V = \mathrm{d}X_1\mathrm{d}X_2\mathrm{d}X_3$ is the volume in the reference configuration. Using this and the $O(1)$ equation for $u_i^{(0)}$, we find from the $O(\epsilon)$ equation that

$$\omega^{(1)} = \frac{\int_V \Delta\hat{C}_{MiQk}\, u_{k,Q}^{(0)}\, u_{i,M}^{(0)}\, \mathrm{d}V}{2\,\omega^{(0)} \int_V \rho_0\, u_{i,M}^{(0)}\, u_{i,M}^{(0)}\, \mathrm{d}V}\,. \tag{6.26}$$

We can eliminate the explicit dependence upon the perturbation parameter, and rewrite this in physical form as

$$\Delta\omega = \frac{\int_V \Delta C_{MiQk}\, u_{k,Q}^{(0)}\, u_{i,M}^{(0)}\, \mathrm{d}V}{2\,\omega^{(0)} \int_V \rho_0\, u_{i,M}^{(0)}\, u_{i,M}^{(0)}\, \mathrm{d}V}\,. \tag{6.27}$$

The frequency perturbations $\Delta\omega$ are added to the eigen-frequency $\omega^{(0)}$ for various values of the wavenumber along the borehole axis, k_z, to obtain the final dispersion curves for the prestressed state. The fractional change in phase velocity is given by

$$\frac{\Delta v}{v} = \frac{\Delta\omega}{\omega^{(0)}}\,. \tag{6.28}$$

6.4 Stoneley Waves in a Pressurized Borehole

In this section we consider the effects on the Stoneley wave due to a pressurization of the borehole (see Figure 6.3). This is perhaps the only available method to induce changes in the stresses around the borehole in order to probe the nonlinearity of the formation. Although the method developed in the previous section is valid for all modes, we will only consider the Stoneley mode ($m = 0$).

An important feature of Equation (6.27) is that the volume integral in the numerator can be separated into two independent contributions coming from the borehole fluid and formation. By subtracting the borehole fluid induced velocity change from the total velocity change, we can obtain the acousto-elastic response of the formation which is of primary interest in this study. We will assume that the formation is initially isotropic and thus characterized by two second-order elastic constants ($c_{11} = \lambda + 2\mu, c_{66} = \mu$) and three third-order elastic constants ($c_{111}, c_{112}, c_{123}$), where we use the abbreviated Voigt notation for these constants.

6.4.1 The Intermediate Stressed State

When the borehole pressure is increased by P_0, the deformations of the borehole fluid and formation are governed by the static equations of equilibrium, and continuity of radial component of particle displacement and radial stress at the borehole wall. The static deformation of the surrounding formation yields the following displacements, stresses, and strains

$$w_R = \frac{P_0 a^2}{2c_{66} R}, \quad w_Z = 0, \tag{6.29}$$

$$T_{RR} = -\frac{P_0 a^2}{R^2}, \quad T_{\theta\theta} = \frac{P_0 a^2}{R^2}, \quad T_{ZZ} = 0, \tag{6.30}$$

$$E_{RR} = -\frac{P_0 a^2}{2c_{66} R^2}, \quad E_{\theta\theta} = \frac{P_0 a^2}{2c_{66} R^2}, \quad E_{ZZ} = 0, \tag{6.31}$$

where (R, Z) are the radial and axial coordinates in the reference state, and we have defined $\mathbf{T} = \mathbf{S}^1$ and $\mathbf{E} = \mathbf{E}^1$. The borehole radius in the reference state is a. Note that, in this particular situation, the assumption of either plane stress or plane strain leads to the same results. Figure 6.4 shows the radial (T_{RR}) and circumferential ($T_{\theta\theta}$) stress distributions away from the borehole. Both of these stresses exhibit R^{-2} dependence, implying that the formation will have less influence on the Stoneley wave at low frequencies. The corresponding displacements, stresses, and strains in the borehole fluid take the following form

$$w_R^f = \frac{P_0 R}{2c_{66}}, \quad w_Z^f = -\frac{P_0(c_{66} + c_{11}^f)Z}{c_{66}c_{11}^f}, \tag{6.32}$$

$$T_{RR}^f = T_{\theta\theta}^f = T_{ZZ}^f = -P_0, \tag{6.33}$$

$$E_{RR}^f = \frac{P_0}{2c_{66}}, \quad E_{\theta\theta}^f = \frac{P_0}{2c_{66}}, \quad E_{ZZ}^f = -\frac{P_0(c_{66} + c_{11}^f)}{c_{66}c_{11}^f}, \tag{6.34}$$

where c_{11}^f is the bulk modulus of the fluid. This completes the definition of the stressed state of the medium.

6.4.2 Computational Results

In this section we will present the results of the Stoneley wave dispersion before and after pressurization of a fluid-filled borehole surrounded by an isotropic nonlinear formation. The borehole radius is taken as $a = 0.1$ m. The density and elastic properties of the fluid (water) and formation (Boise sandstone) are listed in Table 6.2. The nonlinear behavior of the fluid is usually expressed in terms of the parameters A and B appearing in the equation of state (Beyer, 1960). Recently, a relationship between the third-order elastic constants of a fluid and its parameter A and B has been established by Kostek *et al.* (1993), whose derivation can be found in Appendix D.

In Figure 6.5 we show the Stoneley wave dispersion curves before and after the pressurization (solid lines). The dashed line denotes the contribution of the borehole fluid to the total velocity change. Notice that in the low frequency limit the change in the tube wave speed after pressurization is solely due to the acousto-elastic effect of the borehole fluid. This observation is in agreement with an independent calculation of the tube wave speed. An asymptotic analysis ($\omega \to 0$) for the fractional change in the tube wave velocity due to the formation only, in the presence of principal stresses

T_{RR}, $T_{\phi\phi}$, and T_{ZZ}, $(\omega \to 0)$ leads to

$$\left(\frac{\Delta v_T}{v_T}\right)_{\text{form}} = \frac{\rho_0^f v_T^2 a^2}{8\pi c_{66}^2} \int_0^{2\pi} \mathrm{d}\theta \int_a^\infty \frac{\mathrm{d}R}{R^3}$$

$$\times \frac{2}{(1+\nu)c_{66}} \left\{ \left[\frac{1}{4}(1-\nu)(c_{111}-c_{112}) - \frac{1}{2}\nu(c_{112}-c_{123}) + c_{66} \right] (T_{RR} + T_{\theta\theta}) \right.$$

$$\left. + \left[\frac{1}{2}(c_{112}-c_{123}) - \frac{1}{2}\nu(c_{111}-c_{112}) - \nu c_{66} \right] T_{ZZ} \right\}, \qquad (6.35)$$

where $\nu = (c_{11} - 2c_{66})/2(c_{11} - c_{66})$ is the formation Poisson's ratio. From (6.30) we see that, due to this particular prestress system, the fractional change in the velocity due to the formation is $(\Delta v_T/v_T)_{\text{form}} = 0$, in accordance with our numerical results. Therefore, at low frequencies the only contribution to the change in the tube wave velocity comes from the pressure effect on the nonlinear fluid. Figure 6.6 illustrates the fractional change in the Stoneley wave phase velocity as a function of frequency. As expected from the stress distribution shown in Figure 6.4, $\Delta v/v$ increases with frequency. However, the acousto-elastic contribution from the borehole fluid decreases with increasing frequency. At 8 kHz we find that the total change in the Stoneley wave velocity before and after pressurization of 13.79 MPa (2000 psi) is approximately 3.0%. The liquid contribution is about 1.7%.

6.5 Discussions and Conclusion

In this chapter we have developed a perturbation model to study the velocity changes in borehole modes which incorporates nonlinear contributions due to prestresses, in particular, the effects of a static increase in the borehole pressure. We have shown that at low frequencies, stress induced velocity change is basically controlled by the borehole fluid but at higher frequencies there is a significant contribution from the formation. By estimating the nonlinearity of the fluid at low frequencies we can thus separate the contributions at higher frequencies, and have a direct measure of the nonlinearity of the formation. Therefore, by running acoustic logs before and after pressurization we can get a direct measure of the nonlinearity of the rock.

The wave speed changes that we report in this paper are obviously dependent on the degree of nonlinearity of the formation. The parameters that we have used are typical of some consolidated rocks, but there is evidence that they could be much higher for weaker rocks, or even strong rocks but at high stresses such as found around boreholes.

Material	$\rho_0 \mathrm{d}v_s^2/\mathrm{d}P$	$\rho_0 \mathrm{d}v_p^2/\mathrm{d}P$
Water[a]	0	5.0
Benzene[a]	0	9.0
Polystyrene[b]	1.6	11.6
PMMA[c]	3.0	15.0
Pyrex[b]	-2.8	-8.6
Fused Silica[d]	-1.4	-4.3
Alumina[e]	1.1	4.5
Aluminum[f]	2.9	12.4
Nickel-Steel[g]	1.6	2.8
Armco-Iron[b]	5.7	9.3
Steel (Hecla)[f]	1.5	7.5
Molybdenum[f]	1.1	3.5
Tungsten[f]	0.7	4.6
Magnesium[f]	1.5	6.9
Niobium[h]	0.3	6.2
Gold[i]	0.9	6.4

Table 6.1: Dimensionless dependence of sound speed on pressure for some common materials.

[a] Coppens *et al.* (1965)
[b] Hughes and Kelly (1953)
[c] Asay *et al.* (1969)
[d] Bogardus (1965)
[e] Schreiber and Anderson (1966)
[f] Smith *et al.* (1966)
[g] Crecroft (1962)
[h] Graham *et al.* (1968)
[i] Montgomery *et al.* (1967)

	fluid	solid
ρ_0	1000 kg/m^3	2135 kg/m^3
c_{11}	2.25 GPa	19.5 GPa
c_{66}	-	6.5 GPa
c_{111}	-22.5 GPa	-3467 GPa
c_{112}	-13.5 GPa	-1155 GPa
c_{123}	-9.0 GPa	-1541 GPa

Table 6.2: Parameters for water and Boise sandstone.

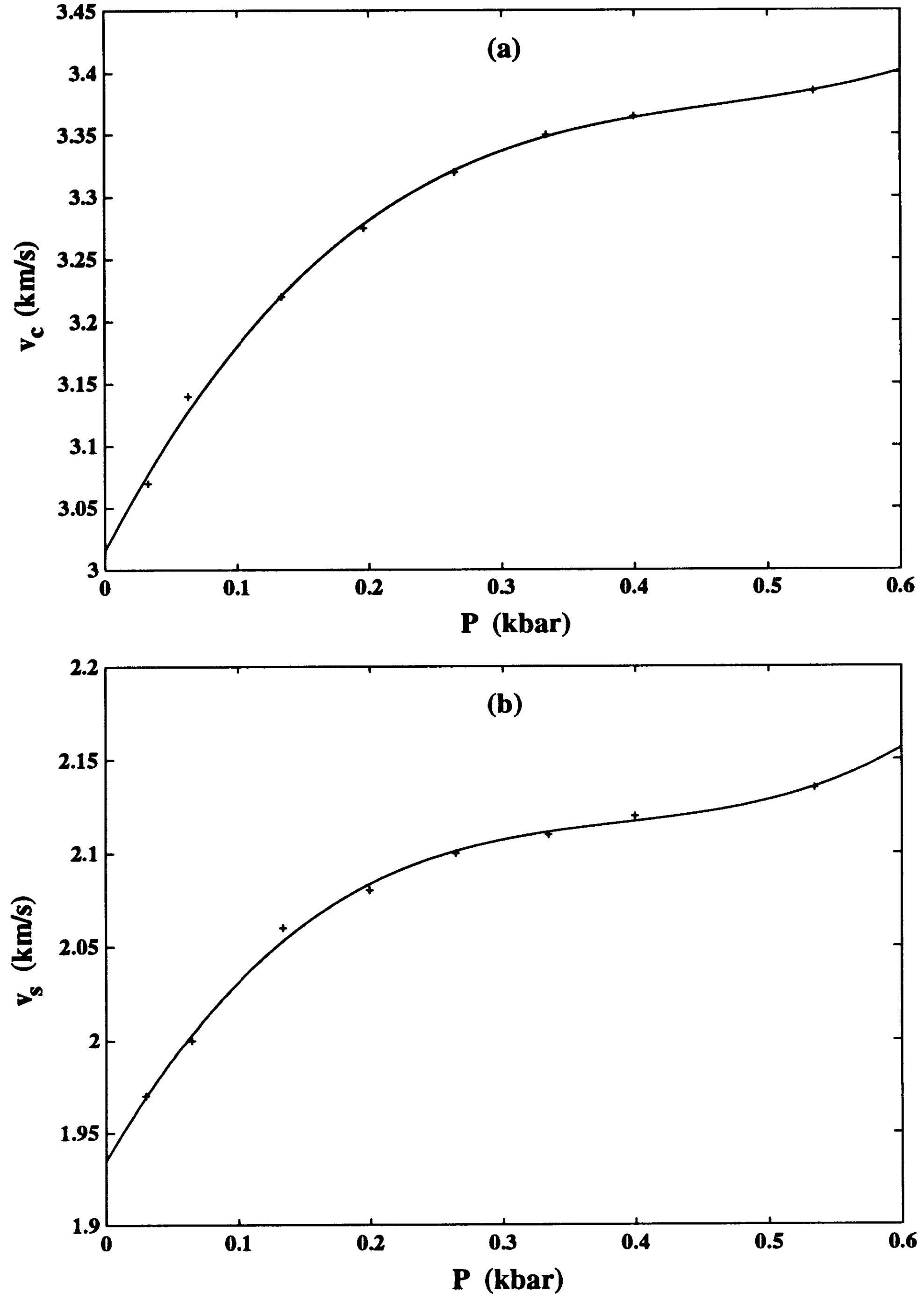

Figure 6.1: Compressional (a) and shear (b) wave speeds for a dry Boise Sandstone as a function of pressure (from Toksöz *et al.*, 1976). The solid curves are simple analytic functions constructed to fit the data.

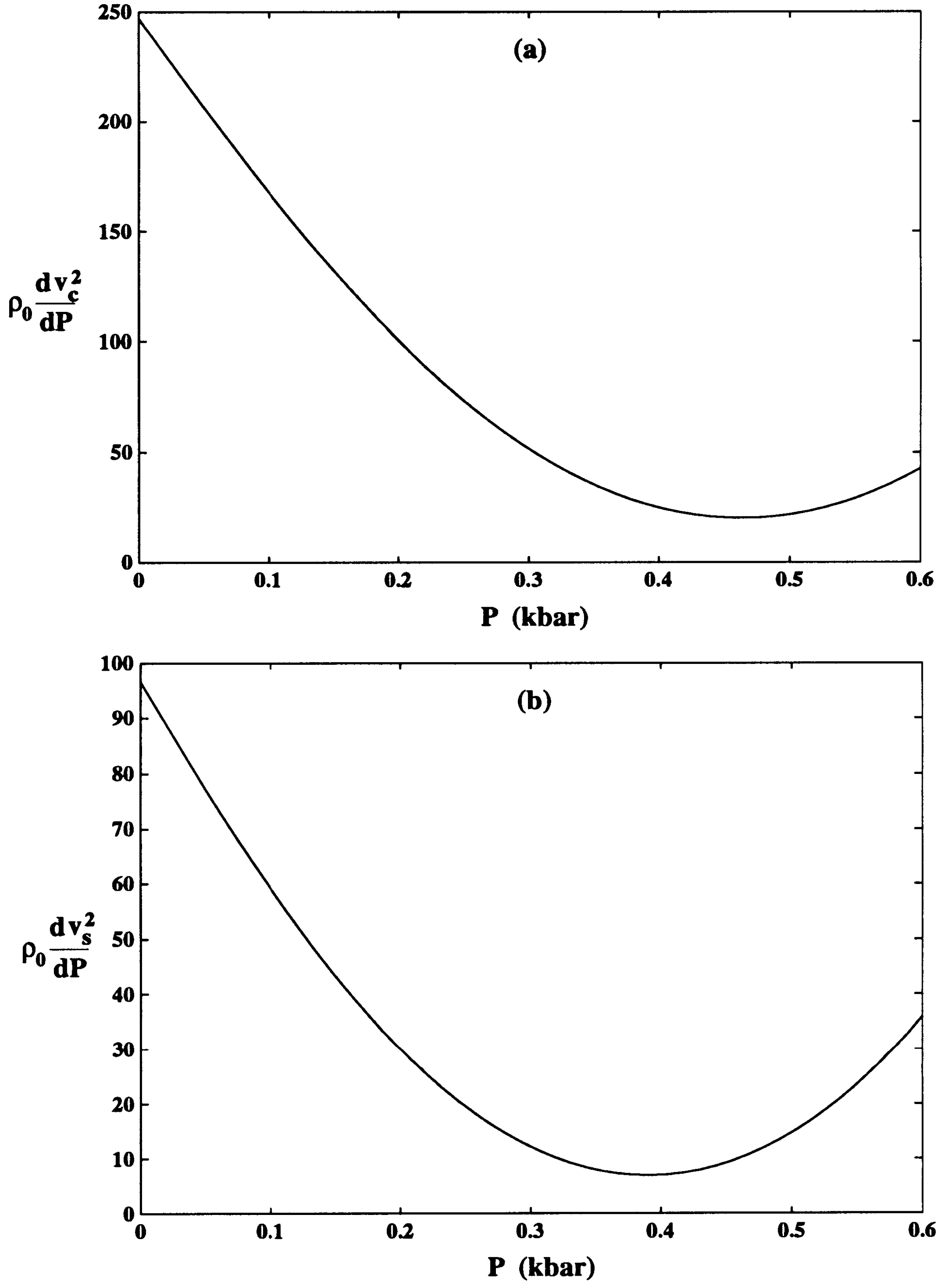

Figure 6.2: The dimensionless quantities $\rho_0 \mathrm{d}v^2/\mathrm{d}P$ for compressional (a) and shear (b) wave speeds in the Boise Sandstone of Figure 6.1. The derivative was taken from the analytic curves in Figure 6.1.

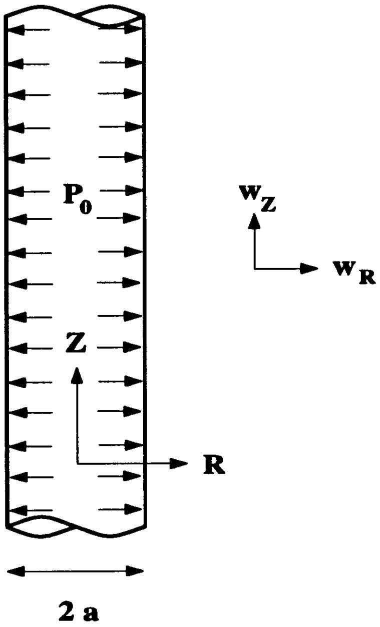

Figure 6.3: Schematic diagram of a pressurized borehole.

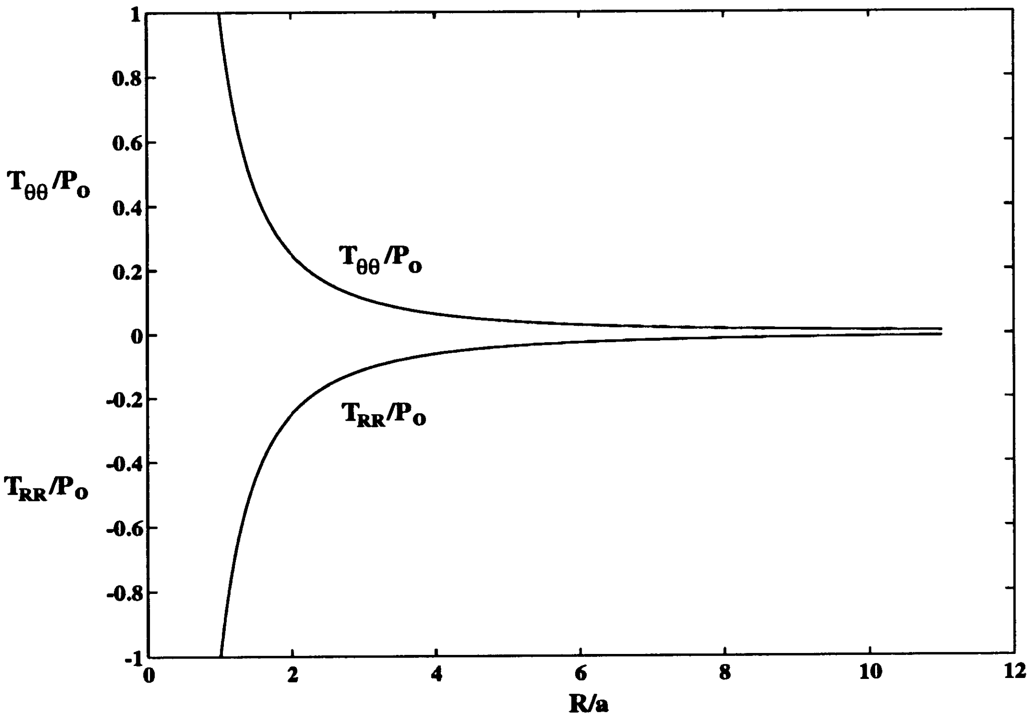

Figure 6.4: Radial and tangential stress distributions around a pressurized borehole.

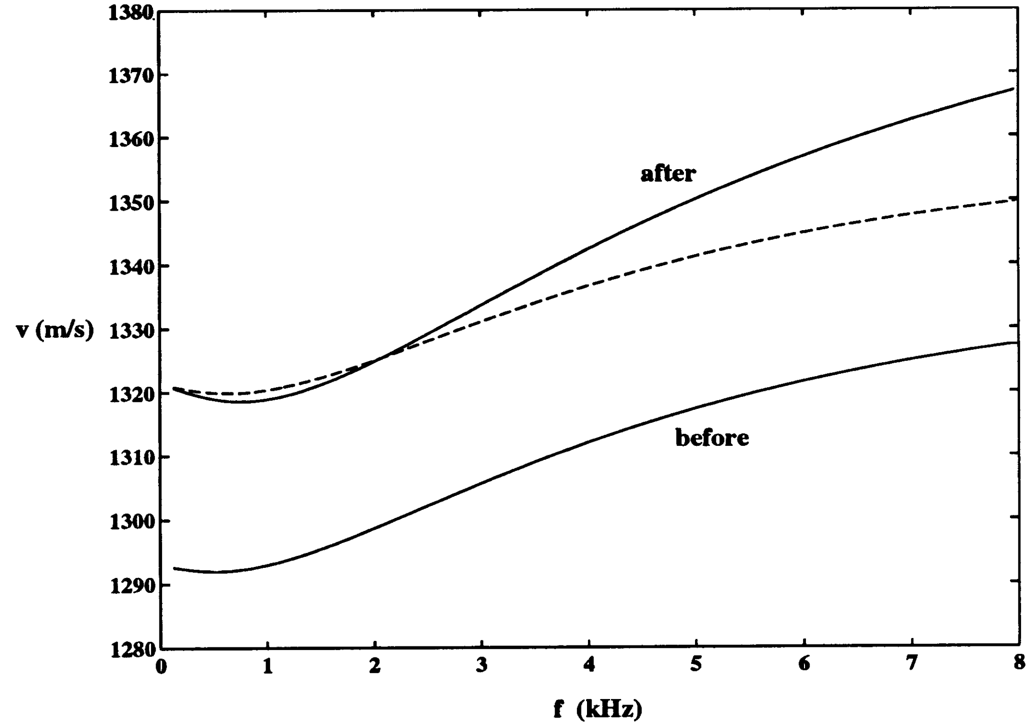

Figure 6.5: Velocity dispersion of Stoneley waves before and after pressurization [$P_0 =$ 13.79 MPa (2000 psi)]. The dashed curve shows the fluid contribution to the total velocity change.

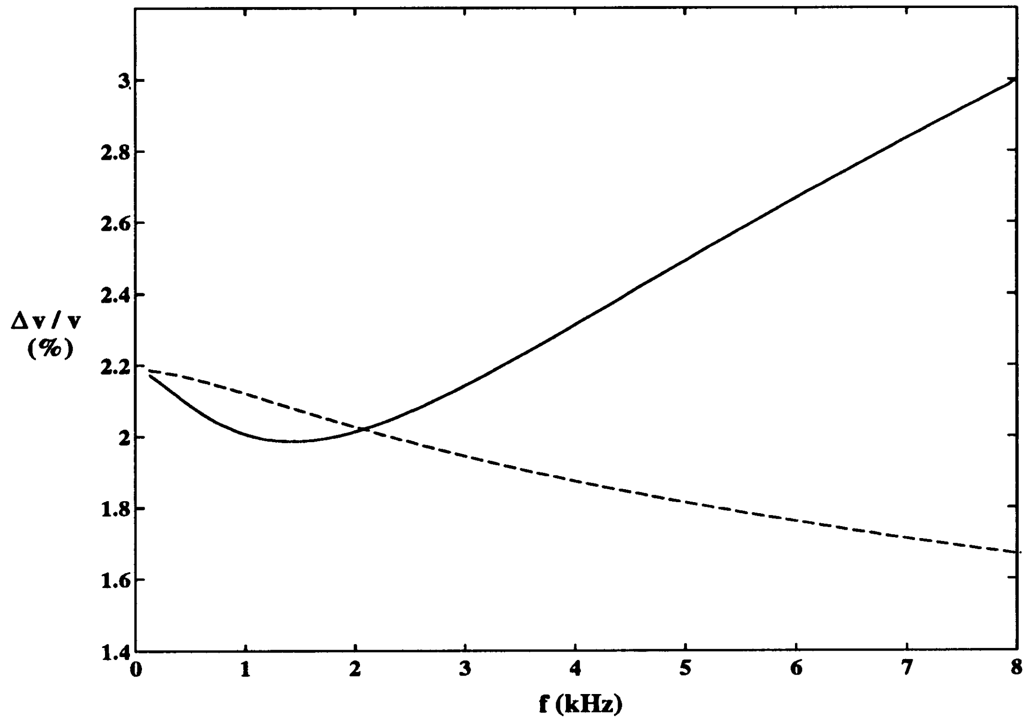

Figure 6.6: Fractional velocity changes of Stoneley wave. The solid curve represents the total change after pressurization, whereas the dashed curve shows only the fluid contribution.

Chapter 7

Conclusions

In this thesis we have set up a formalism for calculating the seismic radiation from a borehole in the limit as the ratio of the borehole diameter to wavelength goes to zero. In this limit an acoustic source in the borehole acts indirectly as a seismic source. The source first generates a tube wave, which is an acoustic wave in the fluid filling the borehole, and the pressure field of the tube wave, by distorting the borehole wall, in turn generates the seismic wave. The action of the tube wave is equivalent in the narrow borehole approximation, to a line distribution of body force along the borehole centerline and acting in the intact elastic solid, *i.e.,* the solid with no borehole in it. We have found expressions for this source distribution, which turn out to be a distribution of dipoles.

In previous work the asymptotic limit of a narrow borehole was calculated by taking the low frequency approximation to an exact solution for a circular cylindrical borehole in an isotropic medium. By directly calculating the asymptotic limit, one is able to find these body-force equivalents and other aspects of the solution in quite general circumstances, without the need for exact solutions. In fact, we have found the asymptotic solution for a curved borehole with elliptic cross-section in an arbitrary anisotropic medium. When these results are specialized to right circularly cylindrical boreholes in an isotropic medium, they agree with previous work in the literature.

These equivalent force systems when combined with general wave propagation codes become a very powerful technique which avoids modeling the source and receiver boreholes, and yet includes all tube wave related effects. Thus, it renders long-range propagation feasible.

We have also considered the radiation problem from the equivalent source distribution in both fast and slow formations and have provided far-field expressions for the displacements. In slow (anisotropic) formations there can be either one or two "conical" waves arriving earlier than the direct wave from source to receiver. We have illustrated our results by plotting radiation patterns for quasi-P, quasi-SV, and SH-waves in isotropic and transversely isotropic media and the corresponding wavefront surfaces. We illustrate the cases where the borehole axis and the TI axis are parallel, and also when they are perpendicular. These two cases can be completely solved analytically. More general situations may require the numerical solution of sextic equations. It is interesting that the expression for the body-force distribution in the equivalent source is obtained as a product of two matrices, one is a function of the material properties of the (anisotropic) medium, including its orientation relative to the borehole, and the other is a function of the parameters of the elliptical cross-section of the borehole.

Finally, we considered the problem of computing the pressure field in one borehole induced by a volume injection source in another borehole. The far-field solution is obtained in closed form, and in particular it clearly shows the reciprocal nature of the problem.

We next studied the interaction of Stoneley waves with fluid-filled fractures intersecting a borehole. We first developed a dynamic fracture model which was implemented numerically with finite differences. This model handles correctly all possible interactions between borehole waves and the fracture. We demonstrated the validity of the model by comparisons with other independent solutions. In our study of Stoneley wave interactions with fractures, we have found that the magnitude of the Stoneley wave reflection coefficient is larger for an elastic formation when compared to that for a rigid one. This result is important since it indicates that an interpretation of the Stoneley wave reflectivity according to a rigid formation model will lead to an overestimation of the fracture aperture h, and thus of the fracture conductivity. Simulations of double fractures show that the interaction between the two fractures has an appreciable effect on the Stoneley reflectivity even when the distance between the fractures is small compared to the wavelength. Here the effect is contrary to that of the elasticity of the formation. Finally, we simulated the effects of a washout-fracture system and showed that at low enough frequencies the effects of the washout can be neglected, since the reflectivity is totally dominated by the fracture characteristics. At higher frequencies, however, the effects of the washout are significant and would lead to a grossly overestimated fracture aperture, if not properly taken into account.

Next, we developed various approximate analytic fracture models which addressed some of the effects described above. Their advantage is that they are simple and can be used effectively in interpreting data. In this vein, we obtained a model for interpreting the tube wave reflection coefficient when the borehole region near the fracture has been washed out or caved in. An estimate of the volume of this region is needed, and can be obtained independently from caliper logs. A frequent problem which leads to false fracture identification is caused by regions where only washouts or caves exist, since by themselves they cause tube wave reflections. We have shown that the behaviour of the reflection coefficient versus frequency can be used to identify these cases. The elasticity of the formation also affects the reflection of tube waves. The analytical model we have developed uses information from the head wave arrivals,*i.e.*, the compressional and shear wave speeds, to predict the reflectivity of tube waves. It can be used to invert for the fracture aperture, which otherwise would be overestimated by a model based on a rigid formation assumption. Finally, we showed the equivalence between a fractured zone and a layer composed of a permeable material characterized by a permeability κ_0. The question of when to use a single equivalent fracture versus a distributed multiple fracture model (or its equivalent) can be addressed by the character of the reflection coefficient versus frequency. Notches in the response curve indicate that a finite thickness zone is present. Alternatively, this question can be answered readily if borehole scans (ultrasonic or electrical) are available.

Finally, we have developed a perturbation model to study the velocity changes in borehole modes which incorporates nonlinear contributions due to prestresses, in particular, the effects of a static increase in the borehole pressure. We have shown that at low frequencies, stress induced velocity changes of the Stoneley wave are basically controlled by the borehole fluid but at higher frequencies there is a significant contribution from the formation. By estimating the nonlinearity of the fluid at low frequencies, we can thus separate the contributions at higher frequencies, and have a direct measure of the nonlinearity of the formation. Therefore, by running acoustic logs before and after pressurization we can get a direct measure of the nonlinearity of the rock.

Appendix A

A Reciprocity Relation

Consider a borehole of elliptic cross-section with axis in the direction $\mathbf{t}$, $|\mathbf{t}| = 1$. Suppose that the surface of the borehole is acted on by a traction $\boldsymbol{\tau}\cdot\mathbf{n}$ derivable from a constant stress $\boldsymbol{\tau}$. Suppose, moreover, that there is no extension in the direction $\mathbf{t}$. (This is the anisotropic equivalent of plane strain.) Then it is known that the displacement $\mathbf{u}$ on the borehole wall is, up to a rigid body motion, a linear function of position:

$$u_i = \sigma_{ik} x_k. \tag{A.1}$$

Here the matrix σ may be taken to be such that

$$\sigma_{ik} t_k = 0. \tag{A.2}$$

We shall consider reciprocity between two such stress states $\{\mathbf{u}^{(1)}, \boldsymbol{\sigma}^{(1)}, \boldsymbol{\tau}^{(1)}\}$ and $\{\mathbf{u}^{(2)}, \boldsymbol{\sigma}^{(2)}, \boldsymbol{\tau}^{(2)}\}$ for the same borehole in the same anisotropic elastic medium. Betti's reciprocity theorem (Love, 1927; p. 173) implies that, in the notation of Section 2.4,

$$\int_{\partial\Sigma} u_i^{(1)} \tau_{ij}^{(2)} n_j \, \mathrm{d}s' = \int_{\partial\Sigma} u_i^{(2)} \tau_{ij}^{(1)} n_j \, \mathrm{d}s', \tag{A.3}$$

where $\partial\Sigma$ is the perimeter of a right cross-section Σ of the borehole, $\mathbf{n}$ is the unit normal to the borehole wall, and $\mathrm{d}s'$ is the element of arclength along $\partial\Sigma$. Let the constant stress fields $\boldsymbol{\tau}^{(1)}$ and $\boldsymbol{\tau}^{(2)}$ be extended as constant functions of position into the interior of the borehole, and the displacement fields $\mathbf{u}^{(1)}$ and $\mathbf{u}^{(2)}$ as the linear functions of (A.1). Using Equation (2.100):

$$n_j = \epsilon_{jpq} t'_p t_q \tag{A.4}$$

in the left member of (A.3), and then applying Stokes's theorem we get

$$\begin{aligned}
\int_{\partial\Sigma} u_i^{(1)}\tau_{ij}^{(2)} n_j \,\mathrm{d}s' &= \int_{\partial\Sigma} u_i^{(1)}\tau_{ij}^{(2)}\epsilon_{jpq}t'_p t_q \,\mathrm{d}s' \\
&= \int_{\partial\Sigma} \epsilon_{rnp}u_{i,n}^{(1)}\tau_{ij}^{(2)}\epsilon_{jpq}t_q t_r \,\mathrm{d}A \\
&= \int_{\partial\Sigma} (\delta_{qr}\delta_{nj} - \delta_{qj}\delta_{nr})\sigma_{in}^{(1)}\tau_{ij}^{(2)} t_q t_r \,\mathrm{d}A \\
&= A\sigma_{in}^{(1)}(\delta_{nj} - t_n t_j)\tau_{ij}^{(2)} \\
&= A\sigma_{ij}^{(1)}\tau_{ij}^{(2)}, \qquad \text{(A.5)}
\end{aligned}$$

by (A.2). Applying a similar calculation to the right member of (A.3) and equating the two we obtain

$$\sigma_{ij}^{(1)}\tau_{ij}^{(2)} = \sigma_{ij}^{(2)}\tau_{ij}^{(1)}. \qquad \text{(A.6)}$$

But $\boldsymbol{\sigma}$ is a linear function of $\boldsymbol{\tau}$, say

$$\sigma_{ij} = N_{ijpq}\tau_{pq}. \qquad \text{(A.7)}$$

Then using (A.7) in (A.6) we obtain

$$N_{ijpq}\tau_{pq}^{(1)}\tau_{ij}^{(2)} = N_{ijpq}\tau_{pq}^{(2)}\tau_{ij}^{(1)}. \qquad \text{(A.8)}$$

The tensors $\boldsymbol{\tau}^{(1)}$ and $\boldsymbol{\tau}^{(2)}$ are symmetric but otherwise arbitrary, and so

$$N_{ijpq} = N_{pqij}, \qquad \text{(A.9)}$$

and we may assume $\mathbf{N}$ has the symmetries

$$N_{ijpq} = N_{jipq} = N_{ijqp}. \qquad \text{(A.10)}$$

Appendix B

Finite-Difference Equations for the Fluid-Filled Borehole Model

In this Appendix we present a stable and accurate finite-difference discretization of Equations (4.1) and (4.2), which govern the behaviour of isotropic elastic media. In particular these equations are used to model wave propagation in a fluid-filled borehole surrounded by an isotropic elastic medium in the absence of any fractures. Figure B.1 shows the layout of the grid used in the computational domain, and the location of the various quantities on the grid. The spatial and temporal staggering of the velocity and stresses is necessary in order that all finite-difference approximations be properly centered.

Let us introduce the forward difference and forward average operators

$$\delta_r f(r_j) = \delta_r f_j = f_{j+1} - f_j, \tag{B.1}$$

$$\sigma_r f(r_j) = \sigma_r f_j = (f_{j+1} + f_j)/2, \tag{B.2}$$

with similar definitions for δ_z, δ_t, σ_z, and σ_t. Approximations to Equations (4.1) and (4.2) may be written as

$$\begin{aligned}\left(\sigma_r \rho_{j-1/2,k+1/2}\right) \frac{\delta_t v^n_{r\ j,k+1/2}}{\Delta t} = {} & \frac{1}{r_j} \frac{\delta_r \left(r \tau^{n+1/2}_{rr}\right)_{j-1/2,k+1/2}}{\Delta r} \\ & - \frac{1}{r_j} \sigma_r \tau^{n+1/2}_{\theta\theta\ j-1/2,k+1/2} + \frac{\delta_z \tau^{n+1/2}_{rz\ j,k}}{\Delta z},\end{aligned} \tag{B.3}$$

$$\left(\sigma_z \rho_{j+1/2,k-1/2}\right) \frac{\delta_t v^n_{z\ j+1/2,k}}{\Delta t} = \frac{1}{r_{j+1/2}} \frac{\delta_r \left(r \tau^{n+1/2}_{rz}\right)_{j,k}}{\Delta r} + \frac{\delta_z \tau^{n+1/2}_{zz\ j+1/2,k-1/2}}{\Delta z}, \tag{B.4}$$

$$\frac{\delta_t \tau_{rr\ j+1/2,k+1/2}^{n+1/2}}{\Delta t} = \lambda_{j+1/2,k+1/2} \left[\frac{1}{r_{j+1/2}} \frac{\delta_r (r v_r)^n_{j,k+1/2}}{\Delta r} + \frac{\delta_z v^n_{z\ j+1/2,k}}{\Delta z} \right] + 2\mu_{j+1/2,k+1/2} \frac{\delta_r v^n_{r\ j,k+1/2}}{\Delta r}, \tag{B.5}$$

$$\frac{\delta_t \tau_{\theta\theta\ j+1/2,k+1/2}^{n+1/2}}{\Delta t} = \lambda_{j+1/2,k+1/2} \left[\frac{1}{r_{j+1/2}} \frac{\delta_r (r v^n_r)_{j,k+1/2}}{\Delta r} + \frac{\delta_z v^n_{z\ j+1/2,k}}{\Delta z} \right] + \frac{2\mu_{j+1/2,k+1/2}}{r_{j+1/2}} \sigma_r v^n_{r\ j,k+1/2}, \tag{B.6}$$

$$\frac{\delta_t \tau_{zz\ j+1/2,k+1/2}^{n+1/2}}{\Delta t} = \lambda_{j+1/2,k+1/2} \left[\frac{1}{r_{j+1/2}} \frac{\delta_r (r v^n_r)_{j,k+1/2}}{\Delta r} + \frac{\delta_z v^n_{z\ j+1/2,k}}{\Delta z} \right] + 2\mu_{j+1/2,k+1/2} \frac{\delta_z v^n_{z\ j+1/2,k}}{\Delta z}, \tag{B.7}$$

$$\frac{\delta_t \tau_{rz\ j,k}^{n+1/2}}{\Delta t} = \left(\sigma_r^{\mathrm{H}} \sigma_z^{\mathrm{H}} \mu_{j-1/2,k-1/2} \right) \left[\frac{\delta_r v^n_{z\ j-1/2,k}}{\Delta r} + \frac{\delta_z v^n_{r\ j,k-1/2}}{\Delta z} \right], \tag{B.8}$$

where the harmonic average operator is defined as $\sigma_r^{\mathrm{H}} f(r_j) = 2(1/f_{j+1} + 1/f_j)^{-1}$, and $r_j = j\Delta r$. Harmonic rather than arithmetic averaging of stiffnesses is proper because the wavelength is much larger than the grid size, $\lambda \gg \ell$, where $\ell = O(\Delta r) = O(\Delta z)$. In this long wavelength (low frequency) regime, the compliances should be arithmetically averaged rather than the stifnesses. This problem is analogous to finding the effective elastic constant of a collection of springs connected in series. Furthermore, if the particular point of interest lies on a fluid-solid interface, then the effective shear rigidity μ will vanish automatically and the shear stress will also vanish according to (B.8). Thus, this scheme automatically accomodates irregular fluid-solid interfaces.

The stability of this system is guaranteed provided the following relation is satisfied

$$v_{\max} \Delta t \left[\frac{1}{(\Delta r)^2} + \frac{1}{(\Delta z)^2} \right]^{1/2} < 1, \tag{B.9}$$

where $v_{\max}$ is the maximum compressional velocity on the grid. The stability condition is independent of both the shear wave velocity, and the Poisson's ratio. The scheme is second-order accurate in space and time, and thus $\ell \leq O(\lambda_{\min}/10)$ in order to minimize numerical grid dispersion. Here $\lambda_{\min}$ is the minimum wavelength travelling on the grid.

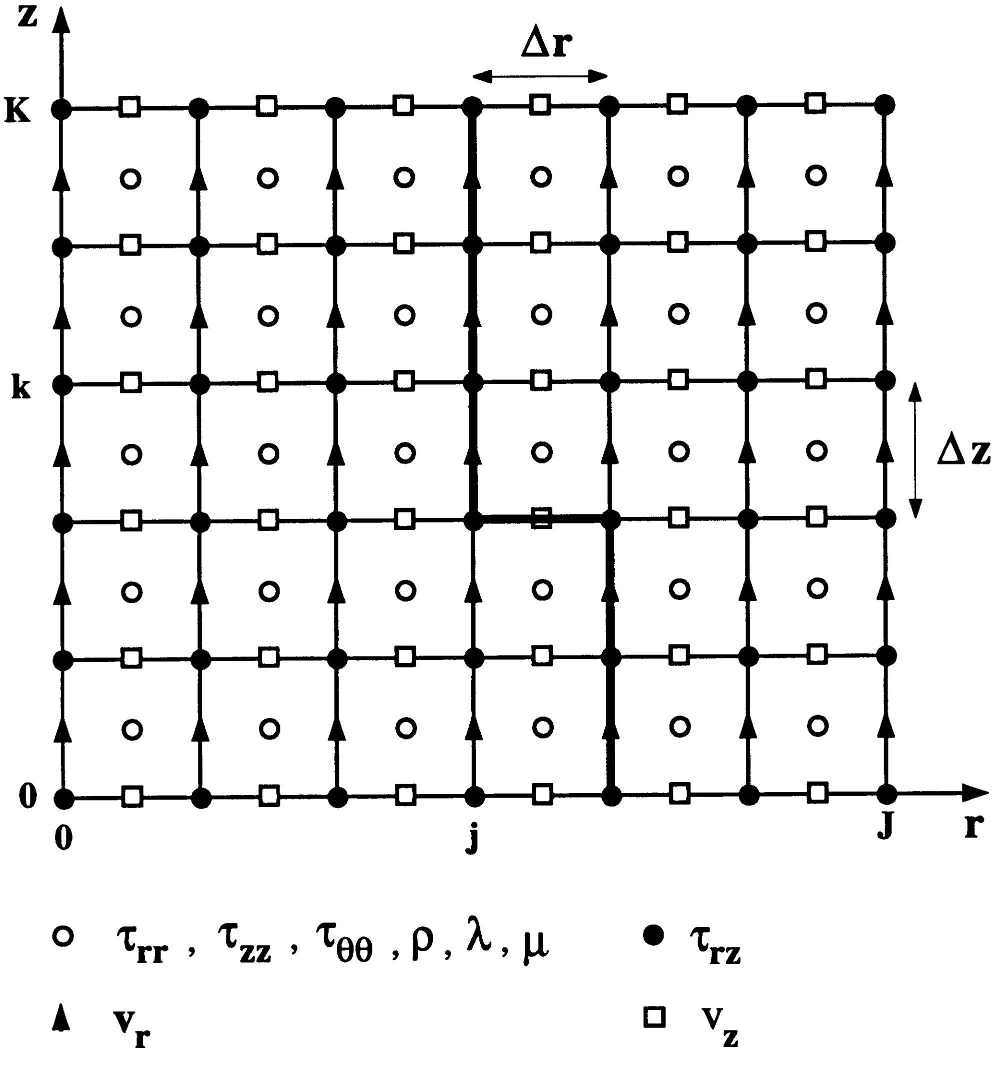

Figure B.1: Staggered finite-difference grid showing the placement of field variables and elastic parameters. The thicker lines represent a fluid-solid interface.

Appendix C

Dispersion Relation for an Infinite Fluid-Filled Fracture

In this Appendix we derive the dispersion relation for axisymmetric modes propagating along an infinite fluid-filled fracture. In Figure C.1 we show the geometry of the problem and the relevant parameters. The fluid-filled fracture is assumed to be confined between two elastic half spaces. Our derivation follows that of Ferrazzini and Aki (1987), but differs in the sense that we consider axisymmetric modes.

The particle displacement in the fluid is given in terms of a displacement potential, ϕ_f, as

$$\mathbf{u} = \nabla \phi^f, \tag{C.1}$$

which satisties the following wave equation

$$\phi^f_{,tt} = v_f^2 \nabla^2 \phi_f, \tag{C.2}$$

where v_f is the acoustic wave speed of the fluid. The pressure in the fluid is given by

$$p = -\rho_f \phi^f_{,tt}. \tag{C.3}$$

Separation of variables leads to the following solution for the potential

$$\phi_f = A(k_r, \omega) H_0^{(1)}(k_r r) \left(e^{k_r \sqrt{\epsilon^2 - 1}\, z} + e^{-k_r \sqrt{\epsilon^2 - 1}\, z} \right) e^{-i\omega t}, \tag{C.4}$$

where

$$\epsilon = \frac{\omega}{v_f k_r}. \tag{C.5}$$

In (C.4) we consider only outgoing cylindrical waves and we assume that $\epsilon < 1$, which corresponds to modes with phase velocities smaller that the fluid velocity. The wall impedance is thus given by

$$\frac{p_f}{u_z}(z = \pm\frac{h}{2}) = \text{sgn}(z)\ \frac{\rho_f \omega^2}{k_r\sqrt{\epsilon^2 - 1}}\ \coth(k_r\sqrt{\epsilon^2 - 1}\ \frac{h}{2}). \tag{C.6}$$

The displacement in the solid half spaces can be expressed in terms of two potentials as

$$\mathbf{u} = \nabla\phi + \nabla \times (\psi \mathbf{e}_\theta), \tag{C.7}$$

where ϕ is associated with compressional motion and ψ with vertically polarized shear motion. The equation of motion in terms of the displacement is

$$\mathbf{u}_{,tt} = v_c^2 \nabla(\nabla \cdot \mathbf{u}) - v_s^2 \nabla \times (\nabla \times \mathbf{u}), \tag{C.8}$$

where v_c and v_s are the compressional and shear wave speeds of the solid, respectively. The two potentials satisfy appropriate scalar wave equations wich yield the following solutions

$$\phi \; = \; B(k_r, \omega)\ H_0^{(1)}(k_r r)\ e^{-k_z^c |z|}\ e^{-i\omega t}, \tag{C.9}$$

$$\psi \; = \; C(k_r, \omega)\ H_1^{(1)}(k_r r)\ e^{-k_z^s |z|}\ e^{-i\omega t}, \tag{C.10}$$

where

$$k_z^c \; = \; \sqrt{k_r^2 - \frac{\omega^2}{v_c^2}}, \tag{C.11}$$

$$k_z^s \; = \; \sqrt{k_r^2 - \frac{\omega^2}{v_s^2}}. \tag{C.12}$$

The vanishing of the shear stress τ_{rz} at $z = \pm h/2$ yields the following relationship between the coefficients B and C

$$\frac{B}{C} = \text{sgn}(z)\ \frac{(2 - \epsilon_s^2)}{2\sqrt{1 - \epsilon_c^2}}\ e^{(k_z^c - k_z^s)h/2}, \tag{C.13}$$

where

$$\epsilon_c = \frac{\omega}{v_c k_r}, \tag{C.14}$$

$$\epsilon_s = \frac{\omega}{v_s k_r}. \tag{C.15}$$

As in the fluid, we can express the wall impedance as

$$\frac{\tau_{zz}}{u_z}(z = \pm\frac{h}{2}) = \mathrm{sgn}(z)\ \frac{\rho k_r v_s^2}{\epsilon_s^4}\left[\frac{(2-\epsilon_s^2)^2}{\sqrt{1-\epsilon_c^2}} - 4\sqrt{1-\epsilon_s^2}\right]. \tag{C.16}$$

Finally, we can make use of the continuity conditions at $z = \pm h/2$ for the normal particle displacements and normal stresses, which take the following concise form

$$(\tau_{zz}/u_z)_{\mathrm{sol}} = (-p_f/u_z)_{\mathrm{flu}}. \tag{C.17}$$

Substituting (C.6) and (C.16) into (C.17) gives the dispersion relation for slow axisymmetric modes in the infinite fluid-filled fracture

$$\coth(\frac{1}{2}\sqrt{\bar{k}_r^2 - \bar{\omega}^2}) + \frac{\rho}{\rho_f}\frac{\sqrt{\bar{k}_r^2 - \bar{\omega}^2}}{(\bar{\omega}\epsilon_s/\epsilon)^4}\left\{\frac{[2\bar{k}_r^2 - (\bar{\omega}\epsilon_s/\epsilon)^2]^2}{\sqrt{\bar{k}_r^2 - (\bar{\omega}\epsilon_c/\epsilon)^2}} - 4\bar{k}_r^2\sqrt{\bar{k}_r^2 - (\bar{\omega}\epsilon_s/\epsilon)^2}\right\} = 0, \tag{C.18}$$

where $\bar{k}_r = k_r h$ and $\bar{\omega} = \omega h/v_f$ are dimensionless radial wavenumber and frequency, respectively.

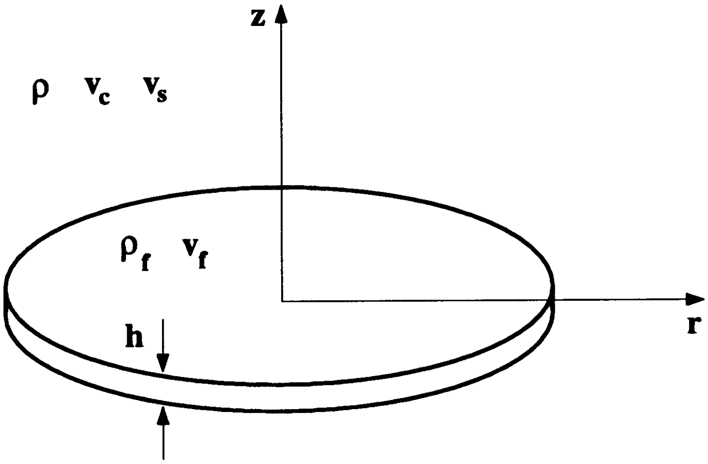

Figure C.1: Fluid-filled fracture bounded by two elastic half spaces.

Appendix D

Third-Order Elastic Constants for an Inviscid Fluid

Nonlinear problems in the acoustics of fluids are usually formulated in terms of an Eulerian description of the wave motion (Beyer, 1984). The elastodynamic of solids on the other hand, is mostly formulated in terms of a Lagrangian description (Eringen and Suhubi, 1974). Also, the choice of fundamental (or primitive) variables is different depending on the type of media. Pressure and density are usually used in adiabatic processes in fluids, whereas stress (Cauchy or Piola-Kirchhoff) and strain (Green or Almansi) are normally used for solids. Therefore the material constants which describe the constitutive behavior of such media will depend on the particular choices of the description and fundamental variables. In dealing with problems involving both fluids and solids it is desirable to use the same description throughout. We next present a derivation for the relation between third-order elastic constants of an inviscid fluid, and the more common parameters, A and B, appearing in the Taylor expansion of the equation of state.

The adiabatic equation of state for a fluid, $p = p(\rho)$, can be expanded in a Taylor series about a given state, and is usually presented in the following form (Beyer, 1960),

$$p = p_0 + A\left(\frac{\rho - \rho_0}{\rho_0}\right) + \frac{B}{2}\left(\frac{\rho - \rho_0}{\rho_0}\right)^2 + O\left(\left(\frac{\rho - \rho_0}{\rho_0}\right)^3\right), \tag{D.1}$$

where p and ρ are pressure and density, respectively, with p_0 and ρ_0 being their reference values, $A = \rho_0 \mathrm{d}p/\mathrm{d}\rho(\rho_0)$ and $B = \rho_0^2 \mathrm{d}^2 p/\mathrm{d}\rho^2(\rho_0)$. In terms of this pressure, the Cauchy stress tensor is given by

$$\boldsymbol{\tau} = -p\mathbf{I}, \tag{D.2}$$

where $\mathbf{I}$ is the second-rank identity tensor. Equations (D.1) and (D.2) define the *constitutive relation* for an inviscid fluid.

In a stressed configuration, particles originally at $\mathbf{X}$ (X_K, $K = 1,2,3$) are displaced to $\mathbf{x}$ (x_k, $k = 1,2,3$), such that we can define the displacement vector as

$$\mathbf{u} = \mathbf{x} - \mathbf{X}. \tag{D.3}$$

The deformation gradient is defined as

$$\mathbf{F} = \frac{\partial \mathbf{x}}{\partial \mathbf{X}} = \mathbf{I} + \frac{\partial \mathbf{u}}{\partial \mathbf{X}}, \tag{D.4}$$

and the Lagrangian (Green) strain tensor is given by

$$\mathbf{E} = \frac{1}{2}\left(\mathbf{F}^{\mathrm{T}}\mathbf{F} - \mathbf{I}\right). \tag{D.5}$$

The density in the stressed configuration can be expressed in terms of its value in the unstressed (reference) configuration through

$$\frac{\rho}{\rho_0} = \frac{1}{\det \mathbf{F}} = \left(1 + 2I_E + 4II_E + 8III_E\right)^{-1/2}, \tag{D.6}$$

where I_E, II_E, and III_E are the principal invariants of the Lagrangian strain tensor (Eringen and Suhubi, 1974), and are given by

$$I_E = \operatorname{tr}\mathbf{E}, \quad II_E = \frac{1}{2}\left[(\operatorname{tr}\mathbf{E})^2 - \operatorname{tr}\mathbf{E}^2\right], \quad III_E = \det \mathbf{E}. \tag{D.7}$$

Expanding (D.6) to second order in strain, and substituting the result into (D.1) yields

$$p = -A\,I_E + \frac{1}{2}(3A + B)\,I_E^2 - 2A\,II_E + O(\mathbf{E}^3), \tag{D.8}$$

which upon substitution into (D.2) gives

$$\tau_{ij} = A\,I_E\delta_{ij} - \frac{1}{2}(3A + B)\,I_E^2\delta_{ij} + 2A\,II_E\delta_{ij}. \tag{D.9}$$

Assuming the fluid is "hyperelastic", we can postulate the existence of a strain energy density function U, defined per unit mass in the reference or Lagrangian description. The strain energy is assumed to be a function of the deformation gradient tensor. Consequently (Eringen and Suhuby, 1974) it depends solely on the strain, and as such admits the following expansion

$$\rho_0 U(\mathbf{E}) = \frac{1}{2}C_{KLMN}E_{KL}E_{MN} + \frac{1}{6}C_{KLMNPQ}E_{KL}E_{MN}E_{PQ} + O(\mathbf{E}^4), \tag{D.10}$$

where C_{KLMN} and C_{KLMNPQ} are, respectively, the second- and third-order adiabatic elastic coefficients evaluated at zero strain (Eringen and Suhubi, 1974; Thurston and Brugger, 1964). These possess the symmetries $C_{KLMN} = C_{LKMN} = C_{MNKL}$ and $C_{KLMNPQ} = C_{LKMNPQ} = C_{MNKLPQ} = C_{KLPQMN}$. The adiabatic Piola-Kirchhoff stress tensor of the second kind, T_{KL}, is defined by

$$T_{KL} = \rho_0 \frac{\partial U}{\partial E_{KL}}. \tag{D.11}$$

The Cauchy and Piola-Kirchhoff stress tensors are related through

$$\tau_{ij} = \frac{\rho}{\rho_0} F_{iK} F_{jL} T_{KL}. \tag{D.12}$$

Making use of Equations (D.10) through (D.12), we can rewrite the latter as

$$\begin{aligned}
\tau_{ij} &= (1 - I_E + \ldots)(\delta_{iK} + u_{i,K})(\delta_{jL} + u_{j,L})(C_{KLMN}E_{MN} + \frac{1}{2}C_{KLMNPQ}E_{MN}E_{PQ}) \\
&= C_{ijKL}E_{KL} + \frac{1}{2}C_{ijKLMN}E_{KL}E_{MN} - C_{ijKL}E_{KL}I_E \\
&\quad +(u_{i,K}C_{KjMN} + u_{j,L}C_{iLMN} + u_{i,K}u_{j,L}C_{KLMN})E_{MN}.
\end{aligned} \tag{D.13}$$

Comparing the terms linear in $\mathbf{E}$ in (D.9) and (D.13) we get

$$A\, I_E\, \delta_{ij} = C_{ijKL}E_{KL}. \tag{D.14}$$

Assuming C_{KLMN} to be isotropic, i.e.,

$$C_{KLMN} = \lambda \delta_{KL}\delta_{MN} + \mu(\delta_{KM}\delta_{LN} + \delta_{KN}\delta_{LM}), \tag{D.15}$$

leads to

$$\lambda = A, \quad \text{and} \quad \mu = 0. \tag{D.16}$$

Equating the nonlinear terms in (D.9) and (D.13), and using (D.16) gives the following identity

$$\begin{aligned}\frac{1}{2}C_{ijKLMN}E_{KL}E_{MN} - A\,I_E^2\,\delta_{ij} + (u_{i,j} + u_{j,i} + u_{i,K}u_{j,K})\,A\,I_E & \\ = -\left[\frac{1}{2}(3A+B)I_E^2 - 2A\,II_E\right]\delta_{ij}. &\end{aligned} \tag{D.17}$$

The quantity $(u_{i,j} + u_{j,i} + u_{i,K}u_{j,K})/2 \equiv \hat{E}_{ij}$ can be rewritten as

$$\begin{aligned}\hat{\mathbf{E}} &= \mathbf{E} + \frac{1}{2}\left(\mathbf{F}^{\mathrm{T}}\mathbf{F} - \mathbf{F}\mathbf{F}^{\mathrm{T}}\right) \\ &= \mathbf{E} + (\boldsymbol{\Omega}\mathbf{E} - \mathbf{E}\boldsymbol{\Omega}) + \mathrm{O}(\mathbf{E}^2),\end{aligned} \tag{D.18}$$

where $\boldsymbol{\Omega} = (\mathbf{F} - \mathbf{F}^{\mathrm{T}})/2$ is the infinitesimal rotation tensor. However, in deriving both sides of (D.17) we have implicitly neglected terms of order $\mathbf{E}^2\boldsymbol{\Omega}$ and smaller. We will say more about this below, but note for the present that to the same degree of approximation (D.17) becomes

$$\frac{1}{2}C_{ijKLMN}E_{KL}E_{MN} = -2AI_E E_{ij} + \left[2A\,II_E - \frac{1}{2}(A+B)I_E^2\right]\delta_{ij}. \tag{D.19}$$

Again, if we assume that C_{KLMNPQ} is isotropic, we can express it as

$$\begin{aligned}C_{KLMNPQ} = \;& \alpha\delta_{KL}\delta_{MN}\delta_{PQ} \\ & +\beta\left[\delta_{KL}(\delta_{MP}\delta_{NQ} + \delta_{MQ}\delta_{NP})\right. \\ & \left. +\delta_{MN}(\delta_{KP}\delta_{LQ} + \delta_{KQ}\delta_{LP}) + \delta_{PQ}(\delta_{KM}\delta_{LN} + \delta_{LM}\delta_{KN})\right] \\ & +\gamma\left[\delta_{LM}(\delta_{KP}\delta_{NQ} + \delta_{KQ}\delta_{NP}) + \delta_{KM}(\delta_{LP}\delta_{NQ} + \delta_{LQ}\delta_{NP}\right. \\ & \left. +\delta_{KN}(\delta_{LP}\delta_{MQ} + \delta_{LQ}\delta_{MP}) + \delta_{LN}(\delta_{KP}\delta_{MQ} + \delta_{KQ}\delta_{MP})\right],\end{aligned} \tag{D.20}$$

where

$$\begin{aligned}\alpha &= C_{112233} = c_{123}, \\ \beta &= \frac{1}{2}(C_{111122} - C_{112233}) = \frac{1}{2}(c_{112} - c_{123}), \\ \gamma &= \frac{1}{8}(C_{111111} - 3C_{111122} + 2C_{112233}) = \frac{1}{8}(c_{111} - 3c_{112} + 2c_{123}),\end{aligned} \tag{D.21}$$

and c_{KLM} is the tensor of elastic constants in the abbreviated Voigt notation. Substituting (D.20) into (D.19) gives the following

$$\begin{aligned}\frac{1}{2}c_{123}I_E^2\,\delta_{KL} + \frac{1}{2}(c_{112}-c_{123})(\text{tr }\mathbf{E}^2\delta_{KL} + 2I_E E_{KL}) \\ + \frac{1}{2}(c_{111} - 3c_{112} + 2c_{123})E_{KP}E_{PL} \\ = -\frac{1}{2}(A+B)I_E^2\,\delta_{KL} + 2A\,II_E\delta_{KL} - 2A\,I_E\,E_{KL}.\end{aligned} \tag{D.22}$$

Using the second equation in $(D.7)$ to eliminate $\operatorname{tr}\mathbf{E}^2$, and equating the coefficients of similar terms on the left and right hand sides of (D.22) we get

$$\begin{aligned} c_{112} &= -(A+B), \\ -(c_{112}-c_{123}) &= 2A, \\ c_{111} - 3c_{112} + 2c_{123} &= 0. \end{aligned} \tag{D.23}$$

Notice that the second equation in (D.23) is obtained twice in this process, thus ascertaining the consistency of the derivation. We thus obtain

$$c_{111} = -(5A+B), \quad c_{112} = -(A+B), \quad c_{123} = A - B. \tag{D.24}$$

We note that had we retained terms of order $\mathbf{E}^2\boldsymbol{\Omega}$ in the expansion of (D.13), it can be shown, using eqs. (D.15) through (D.18), and the isotropic form of C_{KLMNPQ} in (D.20), that they contribute $(2A + c_{111} - c_{123})\,I_E\,(\boldsymbol{\Omega}\mathbf{E} - \mathbf{E}\boldsymbol{\Omega})$ to the Cauchy stress. However, it is clear from $(D.23)_2$ that this contribution vanishes. Hence, we have shown that the hyperelastic and equation of state derivations are consistent, neglecting terms of order $\mathbf{E}^3$.

The first of relations (D.24) was derived in Thurston and Shapiro (1967) [see Equation (43)] by comparing the one-dimensional nonlinear equations of motion derived from the Eulerian and Lagrangian descriptions. Table 1 relates these constants to other sets of constants which appear in the literature (Murnaghan, 1951; Toupin and Bernstein, 1961; Landau and Lifshitz, 1986).

For water (Beyer, 1960; Coppens *et al.*, 1965), $B/A = 5$ and $A = 2.25$ GPa, giving the following third-order elastic constants

$$c_{111} = -22.5 \text{ GPa}, \quad c_{112} = -13.5 \text{ GPa}, \quad c_{123} = -9.0 \text{ GPa}. \tag{D.25}$$

	Murnaghan (1951)	Eringen & Suhubi (1974)	Toupin & Bernstein (1961)	Landau & Lifshitz (1986)	Equation (D.21)
c_{111}	$2l+4m$	$6l_E$	$\nu_1+6\nu_2+8\nu_3$	$2A+6B+2C$	$\alpha+6\beta+8\gamma$
c_{112}	$2l$	$6l_E+2m_E$	$\nu_1+2\nu_2$	$2B+2C$	$\alpha+2\beta$
c_{123}	$2l-2m+n$	$6l_E+3m_E+n_E$	ν_1	$2C$	α

Table D.1: Relation between third-order elastic constants for isotropic solids.

The adiabatic wave speed c is given by (Beyer, 1960)

$$c^2(\rho) = \frac{\mathrm{d}p}{\mathrm{d}\rho}, \tag{D.26}$$

which for a fluid with equation of state given by (D.1) is

$$c^2(\rho) = \frac{A}{\rho_0} + \frac{B}{\rho_0^2}(\rho - \rho_0). \tag{D.27}$$

The natural wave speed c_0 is thus given by

$$c_0^2 = c^2(\rho_0) = \frac{A}{\rho_0}. \tag{D.28}$$

A measure of the nonlinearity of the fluid is given by the dimensionless parameter $\rho_0 \mathrm{d}c^2/\mathrm{d}p$, which by using (D.1) and (D.26) gives

$$\rho_0 \frac{\mathrm{d}c^2}{\mathrm{d}p} = \frac{B}{A}. \tag{D.29}$$

For isotropic solids there are two parameters which measure the degree of nonlinearity and are given by (Toupin and Bernstein, 1961; Hughes and Kelly, 1953)

$$\begin{aligned} \rho_0 \frac{\mathrm{d}v_c^2}{\mathrm{d}p} &= -\frac{7\lambda + 10\mu + c_{111} + 2c_{112}}{3\lambda + 2\mu}, \\ \rho_0 \frac{\mathrm{d}v_s^2}{\mathrm{d}p} &= -\frac{3\lambda + 6\mu + c_{111}/2 - c_{123}/2}{3\lambda + 2\mu}, \end{aligned} \tag{D.30}$$

where v_c and v_s are the speeds of compressional and shear waves, respectively. If we substitute in these expressions the elastic constants given as in (D.16) and (D.24) we get

$$\begin{aligned} \rho_0 \frac{\mathrm{d}v_c^2}{\mathrm{d}p} &= \frac{B}{A}, \\ \rho_0 \frac{\mathrm{d}v_s^2}{\mathrm{d}p} &= 0, \end{aligned} \tag{D.31}$$

which are in agreement with (D.29) and the fact that inviscid fluids do not support shear waves.

The approach taken here compares the Cauchy stress tensor according to the equation of state and from the hyperelastic strain energy density. Alternatively, one can start from the equation of state and find the strain energy, from which the third- and higher-order elastic coefficients could be determined. Thus, eqs. (D.2), (D.5), (D.11), and (D.12), imply

$$\rho_0 \frac{\partial U}{\partial E_{KL}} = -\frac{\rho_0}{\rho} p (\mathbf{I} + 2\mathbf{E})^{-1}. \tag{D.32}$$

Integration then yields

$$\begin{aligned} \rho_0 U &= -\int_0^{\mathbf{E}} p \frac{\rho_0}{\rho} \operatorname{tr}(\mathbf{I} + 2\mathbf{E})^{-1} \mathrm{d}\mathbf{E} \\ &= -\frac{1}{2} \int_0^{\mathbf{E}} p \frac{\rho_0}{\rho} \mathrm{d}\left[\log\det(\mathbf{I} + 2\mathbf{E})\right]. \end{aligned} \tag{D.33}$$

Then using eqs. (D.5) and (D.6) this reduces to the familiar form

$$U = -\int_{\rho_0}^{\rho} p \, \mathrm{d}\rho^{-1}. \tag{D.34}$$

The integral could then be evaluated using eq. (D.1), and subsequently expanded in terms of the invariants of **E**, using (D.6). The elastic moduli are then "read off" by comparing the strain energy with eq. (D.10).

References

Albright, J.N., and P.A. Johnson, 1990, Cross borehole observation of mode conversion from borehole Stoneley waves to channel waves at a coal layer, *Geophys. Prospect.*, *38*, 607-620.

Asay, J.R. , D.L. Lamberson, and A.H. Guenther, 1969, Pressure and temperature dependence of the acoustic velocities in polymethylmethacrylate, *J. Appl. Phys.*, *40*, 1768-1783.

Ben-Menahem, A., and S. Kostek, 1991, The equivalent force system of a monopole source in a fluid-filled open borehole, *Geophysics*, *56*, 1477-1481.

Beyer, R.T., 1960, Parameter of nonlinearity in fluids, *J. Acoust. Soc. Am.*, *32*, 719-721.

Beyer, R. T., Ed., 1984, *Nonlinear Acoustics in Fluids*, Van Nostrand Reinhold Co. Inc., New York.

Biot, M.A., 1956a, Theory of propagation of elastic waves in a fluid-saturated porous solid. I. Low frequency range, *J. Acoust. Soc. Am.*, *28*, 168-178.

Biot, M.A., 1956b, Theory of propagation of elastic waves in a fluid-saturated porous solid. II. High frequency range, *J. Acoust. Soc. Am.*, *28*, 179-191.

Biot, M.A., 1962a, Mechanics of deformation and acoustic propagation in porous media, *J. Appl. Phys.*, *33*, 1482-1498.

Biot, M.A., 1962b, Generalized theory of acoustic propagation in porous dissipative media, *J. Acoust. Soc. Am.*, *34*, 1254-1264.

Bogardus, E.H., 1965, Third-order elastic constants of Ge, MgO, and fused SiO_2, *J. Appl. Phys.*, *36*, A2504-2513.

Brugger, K., 1964, Thermodynamic definition of higher order elastic constants, *Phys. Rev.*, *133*, A1611-1612.

Burridge, R., 1967, The singularity on the plane lids of the wave surface of elastic media with cubic symmetry, *Quart. J. Mech. App. Math.*, *14*, 41-56.

Burridge, R., 1976, *Some Mathematical Topics in Seismology*, Lecture Notes, Courant Institute of Mathematical Sciences, New York University.

Cheng, C.H., and M.N. Toksöz, 1981, Elastic wave propagation in a fluid-filled borehole and synthetic acoustic logs, *Geophysics*, *46*, 1042-1053.

Coppens, A.B., R.T. Beyer, M.B. Seiden, J. Donohue, F. Guepin, R.H. Hodson, and C. Townsend, 1965, Parameter of nonlinearity in fluids. II, *J. Acoust. Soc. Am.*, *38*, 797-804.

Crecroft, D.I., 1962, Ultrasonic wave velocities in stressed nickel steel, *Nature*, *195*, 1193-1194.

de Bruin, J.A., and W. Huizer, 1989, Radiation from waves in boreholes, *Scient. Drill.*, *1*, 3-10.

Eringen, A.C., and E.S. Suhubi, 1974, *Elastodynamics, Vol. 1*, Academic Press, New York.

Ferrazzini, V., and K. Aki, 1987, Slow waves trapped in a fluid-filled infinite crack: Implications for volcanic tremor, *J. Geophys. Res.*, *92*, 9215-9223.

Graham, L.J., H. Nadler, and R. Chang, 1968, Third-order elastic constants of single-crystal and polycrystalline columbium, *J. Appl. Phys.*, *39*, 3025-3033.

Harris, F.J., 1978, On the use of windows for harmonic analysis with the discrete Fourier transform, *Proc. IEEE*, *66*, 51-83.

Heelan, P. A., 1953, Radiation from a cylindrical source of finite length, *Geophysics*, *18*, 685-696.

Holt, R.M., P. Ingsøy, and M. Mikkelsen, 1989, Rock mechanical analysis of North Sea reservoir formations, *SPE Form. Eval.*, *4*, 33-37.

Hornby, B.E., D.L. Johnson, K.W. Winkler, and R.A. Plumb, 1989, Fracture evaluation using reflected Stoneley-wave arrivals, *Geophysics*, *54*, 1274-1288.

Hornby, B.E, S.M. Luthi, and R.A. Plumb, 1992, Comparison of fracture apertures computed from electrical borehole scans and reflected Stoneley waves: An integration interpretation, *The Log Analyst*, *33*, 50-66.

Hughes, D.S., and J.L. Kelly, 1953, Second-order elastic deformation of solids, *Phys. Rev.*, *92*, 1145-1149.

Johnson, D.L., 1986, Recent developments in the acoustic properties of porous media, in *Frontiers of Physical Acoustics, Proc. Enrico Fermi Summer School*, Elsevier, Varenna.

Johnson, D.L., J. Koplik, and R. Dashen, 1987, Theory of dynamic permeability and tortuosity in fluid-saturated porous media, *J. Fluid Mech.*, *176*, 379-402.

Johnson, D.L., J. Koplik, and L.M. Schwartz, 1986, New pore-size parameter characterizing transport in porous media, *Phys. Rev. Lett.*, *57*, 2564-2567.

Johnson, P.A., K.R. McCall, and G.D. Meegan, 1992, Observation and implications of nonlinear elastic wave response in rock, *Nature* (submitted).

Johnson, P.A., A. Migliori, and T.J. Shankland, 1991, Continuous wave phase detection for probing nonlinear elastic wave interactions in rocks, *J. Acoust. Soc. Am.*, *89*, 598-603.

Johnson, P.A., and T.J. Shankland, 1989, Nonlinear generation of elastic waves in granite and sandstone: Continuous wave and travel time observations, *J. Geophys. Res.*, *94*, 17729-17733.

Johnson, P.A., T.J. Shankland, R.J. O'Connell, and J.N. Albright, 1987, Nonlinear generation of elastic waves in crystalline rocks, *J. Geophys. Res.*, *92*, 3597-3602.

King, M.S., 1966, Wave velocities in rocks as a function of changes in overburden pressure and pore fluid saturants, *Geophysics*, *31*, 50-73.

Kostek, S, 1991, *Modeling of Elastic Wave Propagation in a Fluid-Filled Borehole Excited by a Piezoelectric Transducer*, MS thesis, Massachusetts Institute of Technology.

Kostek, S., and C.J. Randall, 1991, Borehole acoustic wave propagation in the presence of fractures: A finite difference approach, *61st Ann. Internat. Mtg., Soc. Expl. Geophys.*, Expanded Abstracts, 863-866.

Kostek, S., B.K. Sinha, and A.N. Norris, 1993, Third-order elastic constants for an inviscid fluid, *J. Acoust. Soc. Am.* (submitted).

Krohn, C.E., 1990, Cross-well continuity logging using seismic guided waves, *60th Ann. Internat. Mtg., Soc. Expl. Geophys.*, Expanded Abstracts, 43-46.

Kurkjian, A.L., and S.K. Chang, 1986, Acoustic multipole sources in fluid-filled boreholes, *Geophysics*, *51*, 148-163.

Kurkjian, A.L., B. de Hon, J.E. White, A.T. de Hoop, and T.L. Marzetta, 1992, A moving point mechanism representation for low-frequency monopole borehole sensors, *54th EAEG Conference Extended Abstract*, Paris, June 1-5.

Landau, L.D., and E.M. Lifshitz, 1986, *Theory of Elasticity*, Pergamon Press, Oxford, 3rd ed., p. 106-107.

Lee, M.W., and A.H. Balch, 1982, Theoretical seismic wave radiation from a fluid-filled borehole, *Geophysics*, *47*, 1308-1314.

Lekhnitskii, S.G., 1963, *Theory of Elasticity of an Anisotropic Body*, Holden-Day, Inc., San Francisco.

Lines, L.R., K.R. Kelly, and J. Queen, 1992, Channel waves in cross-borehole data, *Geophysics*, *57*, 334-342.

Love, A.E.H., 1944, *A Treatise of the Mathematical Theory of Elasticity*, Dover, New York.

Meegan, G.D., P.A. Johnson, R.A. Guyer, and K.R. McCall, 1992, Observations of nonlinear wave behaviour in sandstone, *J. Acoust. Soc. Am.* (submitted).

Meredith, J.A., M.N. Toksöz, and C.H. Cheng, 1991, Secondary shear waves generated from source boreholes, *53rd EAEG Conference Extended Abstract*, paper B003, Florence.

Miller, D.E., 1992, private communication.

Montgomery, P.W., C. Montgomery, D.A. Wald, and J.L.S. Bellin, 1967, Sound velocity measurements at high pressures, *Rev. Sci. Instr.*, *38*, 1073-1076.

Murnaghan, F.D., 1951, *Finite Deformations of an Elastic Solid*, Chapman & Hall, New York, p. 89-95.

Muskhelishvili, N.I., 1953, *Some Basic Problems of the Mathematical Theory of Elasticity*, P.G. Noordhoff, Ltd., Groningen.

Savin, G. N., 1961, *Stress Concentration Around Holes*, Pergamon Press, London.

Schoenberg, M., 1986, Fluid and solid motion in the neighborhood of a fluid-filled borehole due to the passage of a low-frequency elastic plane wave, *Geophysics*, *51*, 1191-1205.

Schreiber, E., and O.L. Anderson, 1966, Pressure derivatives of the sound velocities of polycrystalline alumina, *J. Am. Ceram. Soc.*, *49*, 184-190.

Shkolnik, I.E., L.K. Zarembo, and V.A. Krasilnikov, 1990, On structural non-linear diagnostics of solids and estimation of their strength, in *Frontiers of Nonlinear Acoustics: Proc. of 12th ISNA*, Hamilton, M.F., J. Wu, and T.C.T. Ting, Eds., Elsevier Science Publishers Ltd., London, 589-594.

Sinha, B.K., 1982, Elastic waves in crystals under a bias, *Ferroelectrics*, *41*, 61-73.

Sinha, B.K., A.N. Norris, and S.K. Chang, 1992, Borehole flexural modes in anisotropic formations, *Geophysics* (submitted).

Sinha, B.K. and H.F. Tiersten, 1979, On the influence of a flexural biasing state on the velocity of piezoelectric surface waves, *Wave Motion*, *1*, 37-51.

Smith, R.T., R. Stern, and R.W.B. Stephens, 1966, Third-order elastic moduli of polycrystalline metals from ultrasonic velocity measurements, *J. Acoust. Soc. Am.*, *40*, 1002-1008.

Spring, C.T., and D.G. Dudley, 1992, Acoustic wave propagation in a cylindrical borehole with fractures, *J. Acoust. Soc. Am.*, *91*, 658-669.

Stephen, R.A., F. Pardo-Casas, and C.H. Cheng, 1985, Finite-difference synthetic acoustic logs, *Geophysics*, *50*, 1588-1609.

Stroh, A.N., 1958, Dislocations and cracks in anisotropic elasticity, *Phil. Mag.*, *3*, 625-646.

Stroh, A.N., 1962, Steady-state problems in anisotropic elasticity, *J. Math. Phys.*, *41*, 77-103.

Tang, X.M., 1990, *Acoustic Logging in Fractured and Porous Formations*, PhD thesis, Massachusetts Institute of Technology.

Tang, X.M., and C.H. Cheng, 1993, Borehole Stoneley wave propagation across permeable fractures, *Geophys. Prosp.*, *41*, 165-187.

Thomsen, L., 1986, Weak elastic anisotropy, *Geophysics*, *51*, 1954-1966.

Thurston, R.N., and K. Brugger, 1964, Third-order elastic constants and the velocity of small amplitude elastic waves in homogeneously stressed media, *Phys. Rev.*, *133*, A1604-1610.

Thurston, R.N., and M.J. Shapiro, 1967, Interpretation of ultrasonic experiments on finite-amplitude waves, *J. Acoust. Soc. Am.*, *41*, 1112-1125.

Tiersten, H.F., 1978, Perturbation theory for linear electroelastic equations for small fields superposed on a bias, *J. Acoust. Soc. Am.*, *64*, 832-837.

Ting, T.C.T., 1990, The Stroh formalism and certain invariances in two-dimensional anisotropic elasticity, in *Modern Theory of Anisotropic Elasticity and Applications*, Wu, J., T.C.T. Ting, and D. Barnett, Eds., S.I.A.M. , Philadelphia, 3-32.

Toksöz, M.N., C.H. Cheng, and A. Timur, 1976, Velocities of seismic waves in porous rocks, *Geophysics*, *41*, 621-645.

Toupin, R.A., and B. Bernstein, 1961, Sound waves in deformed perfectly elastic materials. Acoustoelastic effect, *J. Acoust. Soc. Am.*, *33*, 216-225.

Tsang, L., and D. Rader, 1979, Numerical evaluation of the transient acoustic waveform due to a point source in a fluid-filled borehole, *Geophysics*, *44*, 1706-1720.

Virieux, J., 1986, *P-SV* wave propagation in heterogeneous media: Velocity-stress finite difference method, *Geophysics*, *51*, 889-901.

White, J.E., 1953, Signals in a borehole due to plane waves in the solid, *J. Acoust. Soc. Am.*, *25*, 906-915.

White, J.E., and R.L. Sengbush, 1963, Shear waves from explosive sources, *Geophysics*, *28*, 1001-1019.

White, J.E., 1983, *Underground Sound*, Elsevier, Amsterdam.